UNIVERSITY of WISCONSIN
DEPARTMENT of METEOROLOGY

W. Schwerdtfeger

Annual Report

STUDIES OF THE THREE-DIMENSIONAL STRUCTURE OF THE PLANETARY BOUNDARY LAYER

Heinz H. Lettau
PROJECT SUPERVISOR

Contributions by
ROBERT H. BURGG
ERNEST C. KUNG
JOHN E. KUTZBACH
JAMES H. LIENSCH
STEPHEN M. ROBINSON

DA-36-039-SC-80282
Contract with
Meteorology Department, USEPG
Fort Huachuca, Arizona

August 1961

Annual Report

Studies of the Three-Dimensional Structure of the Planetary Boundary Layer

Prepared by

Heinz H. Lettau
Project Supervisor

with Contributions by

Robert H. Burgy
Ernest C. Kung
John E. Kutzbach
James H. Lienesch
Stephen M. Robinson

University of Wisconsin
Department of Meteorology

Under Contract No. DA-36-039-SC-80282
for
Meteorology Department
U. S. Army Electronic Proving Ground
Fort Huachuca, Arizona

August 1961

TABLE OF CONTENTS

SUMMARY

DA Task: 3A99-27-005-08 Micrometeorology, (USAEPG)
Title: Studies of the Three-Dimensional Structure of the Planetary Boundary Layer
Contractor: University of Wisconsin, Madison, Wisconsin

The broad objective of this research is to characterize the three-dimensional structure of the planetary boundary layer. A series of eight investigations is reported, which fall into three types: (1) a comparison of experimental measurements against a theoretical model for the effects of solar heating at the earth's surface, (2) experimental measurements of the effect of variations in surface roughness on the dynamics of the air flow near the ground, and (3) a theoretical analysis of the steady-state, neutral wind profile for the entire planetary boundary layer.

The results may be summarized as follows:

(1) Data are presented for the thermal response of an air-soil system to artificial cycles of solar radiation. It was found that a theoretical two-layer (air-soil) model did not adequately describe the experimental results and that the grass cover at the site must be treated as a third layer. The major discrepancy in magnitude of predicted versus observed amplitude ratios of soil heat flux to net radiation was attributed to the evaporation factor. From this it is evident that thermal response experiments represent a promising method for determining evaporation. For the investigation of two-layer conduction processes, it is recommended that thermal gradient experiments be conducted over surfaces which are free of both moisture and vegetation.

(2) Results are reported from other studies and experiments in a broad attack on the evaluation and significance of the aerodynamic roughness of the earth's surface. Wind profile data from the literature were re-analyzed with special emphasis on measurements above tall vegetation, and a regression was established between vegetation height and aerodynamic roughness. A review of recent literature on drag coefficients for vegetation is included. Data on the areal distribution of plant-cover types were evaluated for the state of Wisconsin and for latitudinal zones. From these data, estimates were obtained for regional and seasonal distributions of vegetation-produced surface roughness by using an empirical relationship between plant height and the aerodynamic roughness parameter. A least square method is described and a program is outlined by which wind profile parameters

can be evaluated from detailed anemometry, with the aid of electronic digital computers. Finally, a series of controlled experiments was conducted to study the effect of varying the area density of defined obstacles on the aerodynamic roughness and other wind profile parameters.

(3) Existing models of mean-velocity distribution in fully turbulent duct flow are critically reviewed in terms of analytical expressions for the length-scale of turbulence. A new theoretical model for the length-scale of turbulence which satisfies the principle of similarity between duct and atmospheric boundary layer flow is given. A comparison of the velocity distribution in duct flow predicted by the model for smooth or rough walls shows satisfactory agreement with observations.

The major result of the study is a generalized mathematical model for steady-state flow in a neutral atmospheric boundary layer. Evidence is also presented which indicates the von Kármán relation is a constant (0.428) only for fully developed flow in ducts with rough walls. A suggestion is made that the turbulent viscosity is adjusted so that the "effective" Reynolds number is less than a critical value (approximately 1,000), and is independent of the Reynolds number.

The investigator concludes that certain aspects of his new mathematical expression for the mean length-scale of turbulence merit closer investigation. The interpretation of a characteristic parameter (m) for duct and atmospheric boundary layer flow as indicating "degree of freedom" (or number of dimensions) makes it similar to the structure of probability functions. This feature may help to consolidate a dual picture of turbulence, in building a bridge between engineering and theoretical concepts.

(4) The new theoretical form for the length-scale of turbulence as a function of distance from the lower boundary is applied to a barotropic atmosphere. As a consequence, all characteristics of the boundary layer are determinate upon specification of three parameters: geostrophic wind, Coriolis force, and aerodynamic roughness. The theory is compatible with the conventional logarithmic wind profile in the surface boundary layer and computed wind spirals compare satisfactorily with observed wind spirals for the boundary layer of the atmosphere. Applications of the theory for estimating the dissipation of energy in the lower troposphere are discussed.

No major conclusions or recommendations other than those stated above are given by the contractor.

METEOROLOGY DEPARTMENT
USAEPG

LIST OF ILLUSTRATIONS

List of Illustrations

List of Illustrations

List of Illustrations

General Introduction

Heinz H. Lettau

Department of Meteorology
University of Wisconsin

The understanding of the kinematics, dynamics, and energetics of the natural small-scale processes near the earth's surface, and the structure of the lower atmosphere, is the prerequisite for any successful application of micrometeorological research. The following brief statement of the general technical requirements of the contract work summarizes the principal objectives of the research program:

"Experiments shall be performed by the contractor to study the horizontal variations of micrometeorological factors as they relate to surface characteristics. The bulk of the experimental effort shall be an intensified investigation of a limited geographical area, under a variety of weather conditions. To the extent possible, the experimental plot shall encompass a natural variety of soil types, topographic features, and surface characteristics to include wooded areas, lakes, cultivated land (in part irrigated) and urban areas. Experimental measurements shall be made within different types of air masses (including Continental Arctic, Continental Polar, and Maritime Tropical) to include data with snow cover and various degrees of solar heating and vegetative growth. Instrumentation shall be both ground based and airborne. Analyses of the data shall be performed in order to evaluate the interrelationship of the horizontal variation of micrometeorological parameters with the state and features of the surface, and to establish mathematical models that describe and permit the prediction of the variability of atmospheric boundary layer structure in a quantitative manner."

The work accomplished during the first two years under the contract has been devoted to the following subtasks:

1. Ground-based instrumentation

2. Airborne instrumentation

3. Micrometeorological measurements, and

4. Evaluation and data analysis

Progress has been made in all subtasks. A list of titles of published scientific papers follows in which results obtained from research sponsored by the contract are reported:

J. A. Dutton, "Space and Time Response of Airborne Sensors for the Measurement of Ground Parameters;" this research was co-sponsored by ONR under Contract Nonr (1202)07 and published as an ONR Technical Report No. 1, 1959.

H. H. Lettau, "Wind Profile, Surface Stress, and Geostrophic Drag Co-efficients in the Atmospheric Surface Layer," was published by Academic Press, Inc., New York, in "Advances in Geophysics," Vol. 6, 1959.

W. L. Pelton, K. M. King, and C. B. Tanner, "An Evaluation of the Thornthwaite and Mean Temperature Methods for Determining Potential Evapotranspiration," Agronomy Journal, Vol. 52, p. 387-395, 1960.

W. L. Pelton and C. B. Tanner, "Energy Balance Data Hancock, Wisconsin," Soils Bulletin 2, University of Wisconsin, June, 1960.

W. L. Pelton and C. B. Tanner, "Potential Evapotranspiration Estimates by the Approximate Energy Balance Method of Penman," Journal of Geophysical Research, 65, No. 10, p. 3391, 1960.

C. B. Tanner and S. M. Robinson, "Black-Body Function Sigma-T^4," January, 1959, University of Wisconsin, Soils Department Report.

H. H. Lettau, "A Theoretical Model of Temperature Variations at the Surface of an Orbiting Satellite," Journal of Geophysical Research, 66, No. 11, p. 3693-3698.

C. B. Tanner, "Energy Balance Approach to Evapotranspiration from Crops," Proceedings, Soil Science Society of America, Vol. 24, p. 1-9, January, 1960.

C. B. Tanner, "Radiant Energy Exchange in a Cornfield," Agronomy Journal, Vol. 52, p. 373-379, 1960.

The work under the contract has been advanced on a broad front. For the present annual report it was decided to concentrate on evaluation and data analysis, and to discuss subtasks which could be attacked with a minimum of required new instrument development. A report on instrumentation, new flight investigations, and other subtasks will be submitted in due time.

The main characteristic of what may be referred to as the "Wisconsin-approach" to micrometeorological research is the emphasis on (a) controlled, or genuine micrometeorological experiments, and (b) the relationship between small-scale and large, or synoptic-scale meteorological processes. The concept of controlled micrometeorological experimentation was discussed in Section 2.2 of the Final Report, Contract DA-36-039-SC-80063, entitled "Research Problems in Micrometeorology," by Heinz H. Lettau, dated September 1959. In the present report, a first series of thermal response experiments, involving artificial cycling of natural radiation fluxes, is described in the paper by J. Lienesch, and a first series of wind-stress experiments, involving a controlled modification of surface roughness, in another paper by J. Kutzbach. The results of these experiments are highly interesting. It can be expected that they will open new aspects of micrometeorological research. The thermal response experiment deals with a problem-complex, which includes the special problem of heat diffusion in a non-homogeneous conductor and also that of the balance between heat conduction and black-body radiation, under extreme conditions.

Concerning the relationship between small-scale and large to synoptic-scale atmospheric processes, it is, perhaps, surprising that the controlled wind stress experiment (reported in the paper by Kutzbach) has not only contributed to the clarification of the action of an ensemble of roughness elements, but also has opened aspects of large-scale application of a typically small-scale experiment. The key for this is the use of the concept of the geostrophic drag coefficient, which is also discussed, and directly applied to synoptic-scale problems, even numerical weather prediction problems (as far as dissipation of mechanical energy by friction is concerned), in Paper No. 9. The other papers of this report fit into the frame in that they deal essentially with a first attempt to establish the regional and continent-wide basis for estimating the aerodynamic roughness parameter of the earth's surface. This is an important step in the evaluation of the interrelationship of the horizontal variation of micrometeorological parameters with the state and features of the surface, and towards establishment of mathematical models that describe, and permit the prediction of the variability of atmospheric boundary layer structure in a quantitative manner.

Scanner's note:

This page is blank.

2

Experimental Investigation of the Thermal Response of the Air-Soil System to Controlled Radiation Pulses[1]

James H. Lienesch

Department of Meteorology
University of Wisconsin

Abstract. The results of an experimental investigation of the transformation of solar energy at a grass surface to sensible heat fluxes into air and soil are presented. The dependence of the response of the air-soil system to arbitrary cycling of incoming solar energy by means of a movable shading device is examined as a function of period. Comparison with Lettau's theoretical model is presented and probable causes for departure from this model are discussed.

2.1 Introduction

The incident solar radiation upon the surface of the earth is transformed into heat pulses into the air and soil, which follow the yearly and daily variations of the sun's intensity. These pulses are harmonic in character and produce sinusoidal oscillations in the temperatures of the two mediums (air and soil). Lettau (1951, 1952) has presented a theory which describes the temperature distribution in terms of the available radiation energy and the thermal parameters of the surface, soil, and air. He has described the response of a two-layer system to periodic heat pulses. Lettau (1959) has outlined an experimental method for the determination of the thermal

---

[1] Part of this work was submitted to the University of Wisconsin in partial fulfillment of the requirements for the degree of Master of Science. In addition to sponsorship by the U. S. Army Electronic Proving Ground, Fort Huachuca, Meteorology Department, the research in this paper has been supported by the National Science Foundation, Washington, D. C., under Grant No. G-5786.

response, i. e., the ratio of surface temperature amplitude (deg) and the amplitude of the forcing function (ly/sec), for a variety of frequencies of the forcing function.

In the spring of 1959, Dr. Baumgartner, University of Munich, was visiting the University of Wisconsin. He prepared a study of the feasibility of this experiment and computed the response of the two mediums to short period energy pulses, on the basis of Lettau's model. An unpublished manuscript of Baumgartner (1959) summarizes the result.

It is the purpose of this paper to report the results of the experimental investigation, as outlined by Lettau, designed to explore the process involved in the transformation of a periodic energy wave at the surface, and its propagation into the air and soil. The energy wave was obtained by periodically shading an experimental site from direct solar radiation. The dependence of the temperature response in the two mediums on the period of energy wave can be observed by varying the duration of the controlled radiation pulses. It was felt that the range of the shading periods should cover an order of magnitude to obtain significant changes in the response to the forcing function.

It is desirable that the intensity of available energy be nearly constant throughout the entire duration of the experiment. This restricts the experiment to approximately two hours, one hour before to one hour after noon of a clear day. Since the longer periods of the energy wave should be of the order of ten times that of the shorter periods, a minimum program (within two hours) consisting of a succession of two, four, ten, twenty and forty minute periods was selected. Time allowed the immediate repetition of the shorter periods so that a typical test would proceed with three two-minute periods, followed by two four-minute periods, single ten, twenty, and forty minute periods, and then another twenty, ten, etc. . . . to the two-minute periods through the reverse order. For an illustration of this see Fig. 1. The response of the two layer system could then be observed in the form of a spectrum for the frequencies of the energy pulse.

2.2 Description of Site

The site of the experiment was an open field near the flat top of a low hill, part of the Picnic Point Reservation on the campus of the University of Wisconsin. The area, sloping slightly (6%) to the east, was surrounded by farm fields with the nearest stand of trees approximately 100 yards distant eastwards and down-hill from the

site. The test field, approximately 150 feet square, was seeded with grass in the spring of the year in order to provide a uniform surface cover. By the fall of the year, the grass was quite dense and provided a relatively smooth surface.

Near the center of the field a radiation shield was constructed to provide for the periodic shading of the experimental area. It was made of aluminum sheeting, eight feet square. It could be pivoted about a horizontal axis at its lower side so that it either shaded the experimental area or exposed the area to the direct solar beam. The size of the shaded area could be varied by changing the angle of the shield, thus minimizing the effect of the sun angle. Heating of the shield and the possible resulting increase in long-wave radiation from the shield was reduced by positioning it parallel to the solar beam during periods of exposure of the experimental area to direct sunlight.

The area affected by the shading was mown prior to each experiment so that the grass height was about two inches. The grass in the surrounding area was kept at a height of about three to four inches.

2.3 Instrumentation

2.3.1 Instruments above the surface

Incoming short-wave radiation was measured by an Epply Pyrheliometer at a height of approximately one meter. This instrument was within the shaded area, and exposed so that during periods of shading it measured the diffuse radiation from approximately 95% of the sky. This pyrheliometer had a time lag of about one minute, therefore instantaneous values of short-wave radiation immediately following shading or exposure could only be estimated from the values indicated after the instrument came to equilibrium.

A ventilated net radiometer of the type described by Suomi, Fransilla, and Islitzer (1954) was used to measure net radiation. This instrument was at a height of about one meter and positioned to "see" a surface area immediately adjacent to the area containing the soil instruments. The surface beneath the net radiometer was equivalent to that beneath which the soil sensors were located. The time lag of this instrument was only a few seconds. It also was within the area of shading.

The most difficult problem proved to be an accurate method of

determining air temperature close to the grass surface. It would be desirable to employ an instrument which is completely free of any radiation error. Since such an ideal sensor was not available, an attempt was made to determine and eliminate the radiation error of the sensor. One possible method is to paint one group of thermocouples white and a separate group, black. By varying the number of white thermocouples relative to the black thermocouples and opposing or "bucking" the voltages produced, it was hoped that radiation error would be eliminated. It was found that such an instrument, upon exposure to radiation, had a lag time which was longer than could be tolerated in this investigation. Specifically, this sensor system tended to produce an initial overshoot in voltage when solar radiation was first incident and an initial overshoot when it was removed.

It seemed therefore more advisable to record the air temperatures with the aid of two separate thermocouples, one painted black and the other white. Knowing the absorptivity of the two paints (0.31 for white and 0.88 for black), the extrapolation to zero absorptivity (i.e., elimination of radiation error) was done numerically. Two white thermocouples and two black thermocouples were alternately arranged on a support which held the sensors about two inches above the soil surface.

Average wind speed for the duration of a test was measured by a cup anemometer at a height of approximately two feet. A hot-wire anemometer was used on occasion (days with large wind velocities) to measure maximum wind velocities prior to the test. These measurements were the basis for the estimate of the diffusivity of the air.

2.3.2 Instruments below the surface

To measure the soil temperature a thermopile consisting of eight thermocouples was placed in the soil at a depth of 0.5 cm. The eight thermocouples were located within a circle about 3 inches in diameter to provide an integrated value over a small area. It was not an easy task to position each individual junction so that a 0.5 cm layer of soil covered each one. However, it is felt that the average soil cover was satisfactorily close to 0.50 cm.

The difference in soil temperature between the 0.5 cm level and the 2.5 cm level was measured directly by a thermopile with one set of ten junctions at each level. The two sets of junctions were placed in a horizontal line approximately 2 inches in length. Again it was difficult to insure that the proper depths were maintained individually

but the average levels for each of the two sets of junctions should be satisfactorily close to the assumed depths (0.50 cm and 2.5 cm).

All the thermocouples were made from No. 30 Leeds and Northrup thermocouple wire. Those placed in the soil were covered by a plastic jacket to prevent electrical conduction between sensors through the moist soil. The remainder of the thermocouple wire in contact with the soil was coated with Dow Corning 808 Resin and a varnish to minimize electrical leakage to the soil.

At a depth of 1.5 cm a heat flux transducer was placed. The transducer itself is composed of a silver-constantan thermopile arranged in a thin phenolic resin plate. This instrument, manufactured by Beckman and Whitley Company, indicates the heat flow through the plate by an electromotive force produced by the difference in temperature between the two sets of thermojunctions, which are parallel and adjacent to the two sides of the plate. The sensitivity of the transducer is temperature dependent. Therefore, a thermocouple junction in the plate provides for measurement of the transducer temperature, which corresponds to an additional soil temperature measurement at a depth of 1.5 cm.

The various soil sensors were installed in the soil by digging three shallow holes, each with one vertical wall. The sensors were then placed in the vertical walls at their respective depths, forming a semicircular arrangement.

As a reference junction for all thermocouples a thermos bottle was placed below the soil surface at a horizontal distance of approximately 1.5 feet from the sensors. Oil was used as a reference bath because of its low electrical conductivity. The temperature of the oil was read by a mercury thermometer accurate to the nearest tenth of a degree. Each reference junction in the bath was covered with a plastic jacket to prevent contact between junctions.

2.3.3 Recording and calibration

Tentative experiments using a different shading device were made by Dr. Baumgartner at the same field site in May, 1959. At that time a one-channel recorder was used, with switching devices. It became immediately obvious that continuous and simultaneous recording of all elements on one chart is a necessity.

For the series of experiments described here, a Honeywell 906B Visicorder Oscillograph was used. Through mirror galvonometers

Table 1. Results of thermal response experiment at the University of Wisconsin Micrometeorological Site during three clear days in Fall of 1960. Listed are double amplitudes of: (1) air temperature at 5 cm, (2) soil temperature at 0.5 cm, (3) soil temperature difference 0.5 to 2.5 cm (all in °C), (4) soil heat flux at 1.5 cm, and (5) net radiation, in ly/min, for indicated shading periods.

	Shading Period (in Minutes)															
	2	2	2	2	4	4	10	20	40	20	10	4	4	2	2	2
	October 17															
(1)	----	-----	2.05	3.05	2.90	3.50	3.90	4.35	4.24	3.85	4.20	2.65	3.05	2.10	1.90	-----
(2)	----	-----	-----	-----	.11	.08	.44	.95	1.53	.89	.45	.15	.16	.09	.08	-----
(3)	----	-----	.02	.03	.11	.09	.40	.85	1.13	.89	.42	.08	.10	.03	.02	-----
(4)	----	-----	-----	-----	-----	-----	-----	-----	.058	.049	.031	.011	.012	.003	.002	-----
(5)	----	-----	.785	.785	.775	.790	.790	.805	.815	.810	.795	.790	.770	.755	.670	-----
	October 24															
(1)	----	2.00	2.15	3.70	2.60	3.90	6.70	7.50	-----	5.50	5.00	2.70	5.00	3.00	4.70	3.70
(2)	----	.04	.05	.05	.13	.14	.53	.98	-----	1.02	.49	.14	.15	.09	.09	.07
(3)	----	-----	-----	.02	.12	.12	.45	.85	-----	.95	.46	.09	.11	.04	.04	-----
(4)	----	-----	-----	-----	-----	-----	-----	.041	-----	.036	.018	.008	-----	-----	-----	-----
(5)	----	.755	.740	.740	.740	.740	.750	.735	-----	.725	.710	.685	.685	.675	.675	.675
	November 3															
(1)	.85	1.55	1.60	1.90	2.40	.195	2.05	2.15	3.00	2.05	2.20	1.40	1.80	.90	-----	-----
(2)	.05	.06	.06	.07	.18	.15	.33	.64	1.01	.60	.31	.11	.10	.06	-----	-----
(3)	.03	.04	.03	.04	.13	.10	.33	.61	.80	.53	.28	.06	.06	.02	.03	-----
(4)	.003	.004	.004	.003	.007	.011	.026	.049	.055	.039	.020	.007	.008	.003	.002	-----
(5)	.790	.805	.805	.795	.795	.805	.755	.755	.745	.700	.680	.660	.630	.635	.620	-----

this instrument can record up to 12 signals simultaneously and continuously, without interference, on photographic paper which develops upon exposure to ultraviolet light. A total of eight galvonometers was used, one for each instrument: (1) the Epply pyrheliometer, (2) the net radiometer, (3) the white air temperature thermocouples, (4) the black air temperature thermocouples, (5) the soil temperature thermopile at 0.5 cm, (6) the thermopile for measuring the difference in soil temperature between the 0.5 cm level and the 2.5 cm level, (7) the soil heat flux transducer at 1.5 cm, and (8) the temperature of the soil heat flux transducer. Trace identification was accomplished through occasional systematic shorting of the circuits in a prescribed sequence. The paper transport of the available instrument was inconveniently fast. A timer was constructed which allowed the paper drive mechanism to operate for only one second in every ten seconds. Thus the record obtained indicated the voltage corresponding to a simultaneous sampling rate of once every ten seconds.

The recorder was located in a house trailer approximately 80 feet from the experimental area and connected to three 8-conductor magnetically insulated cables in a plastic tube 6 inches below the soil surface. A junction-box 10 feet from the sensors was used to connect the cables to the 2-conductor cables from each sensor. Grounding was provided at the trailer housing the recorder.

The Epply pyrheliometer and the net radiometer were calibrated in early fall of 1960 with the use of a secondary standard, an Abbot Silver-Disk pyrheliometer. The calibrations of these instruments on two separate days were within 4% for the net radiometer, and 2% for the pyrheliometer.

The calibration for the heat flux transducer was provided by the manufacturer. The calibration for the thermocouples was obtained from the Standard Conversion Tables for Leeds and Northrup Thermocouples.

2.4 Experimental Results

2.4.1 Raw data

Due to the nature of the experiment it was necessary to confine the investigation to cloudless days with the wind direction between southwest and northwest. After completion of the instrumentation, and before the winter season, only three such days occurred, on October 17, October 24, and November 3, 1960. On October 24 the wind was very light; on October 17, gusty to 20 mph; and on November 3, gusty to

Figure 1

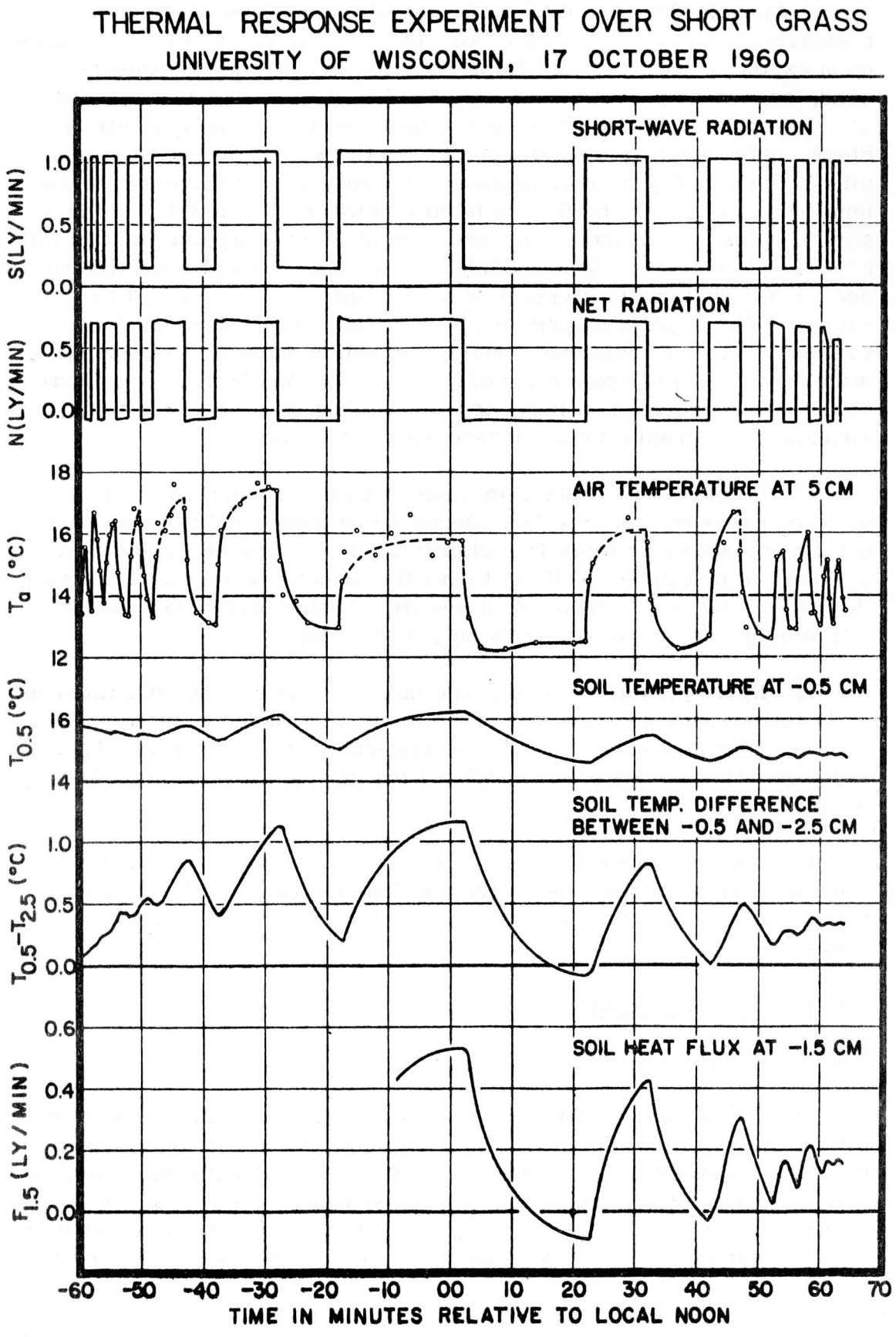
THERMAL RESPONSE EXPERIMENT OVER SHORT GRASS
UNIVERSITY OF WISCONSIN, 17 OCTOBER 1960
SHORT-WAVE RADIATION
S(LY/MIN)
1.0
0.5
0.0
NET RADIATION
N(LY/MIN)
0.5
0.0
AIR TEMPERATURE AT 5 CM
T_a (°C)
18
16
14
12
SOIL TEMPERATURE AT -0.5 CM
$T_{0.5}$ (°C)
16
14
SOIL TEMP. DIFFERENCE
BETWEEN -0.5 AND -2.5 CM
$T_{0.5}-T_{2.5}$ (°C)
1.0
0.5
0.0
SOIL HEAT FLUX AT -1.5 CM
$F_{1.5}$ (LY/MIN)
0.6
0.4
0.2
0.0
-60 -50 -40 -30 -20 -10 00 10 20 30 40 50 60 70
TIME IN MINUTES RELATIVE TO LOCAL NOON

25 mph. Owing to rainy days in between, the soil moisture conditions also were different, as is discussed in Section 2.6.2, in connection with soil heat conductivity data.

The recorded values were read from the photographic paper and were replotted for each of the three days. Trends were then eliminated from the results. This was done in the following manner. Envelopes encompassing the maximum and minimum values of amplitudes for the sequence of radiation pulses were constructed. The actual data was then expressed as the numerical difference between the two envelope curves.

Records for the three days did not show any great dissimilarities. The amplitude values were not constant because of changes in solar radiation, air and soil parameters from one day to the other. But, in general, the character of the amplitude response to the periodic heat pulses as a function of period was found to be satisfactorily reproducible.

Table 1 gives the response of the measured elements to the various frequencies of the forcing functions for the three days. The values presented in this table are equivalent to twice the amplitude of the response, i.e., they are the difference between maximum and minimum points occurring during the sequence of radiation pulses.

2.4.2 Analysis of October 17 data

The data obtained on October 17 is fairly representative of the data obtained on the remaining two days. Figure 1 is a composite showing the response of the system to the controlled pulses forced upon the experimental area on October 17. The following discussion applies, in general, also for the data obtained on October 24 and November 3.

The values for solar short-wave radiation and for the total net radiation give an indication of the amount of energy potentially available at the surface for transformation into sensible heat. These curves also illustrate the controlled cycling of the radiation pulses. The relatively small over-all variation in the solar radiation was insignificant for the results of the experiment. The decrease in the amount of net radiation at the end of the test period is explained by the gradual march of the shaded area across the experimental site as a result of the changing sun angle. The net radiometer "saw" this gradual advance of unshaded surface because of its relatively large field of view.

In contrast to the soil variables the amplitudes of the air temperature show a relatively weak dependency on the frequency of the forcing function. The method by which the air temperature was obtained was discussed in Section 2.3. 1. It amounts to the elimination of the radiation error with the aid of two sensors having known but relatively large radiation errors. It was thought that possibly the absorptivities assumed for the two paints were not accurately enough known. Therefore, extrapolation to zero absorptivity was tested assuming ± 10% variation in the absorptivities of the two paints. No significant change in the result was obtained. Convective cooling was apparent as is illustrated by the dispersion of the air temperature data points in Fig. 1. However, it is not felt that the cooling of the sensors by the wind was mainly responsible for the result obtained. The reliability of the air temperature measurement in this experiment is still an open question.

The curves representing the soil temperature and the difference in temperature between the 0.5 cm level and the 2.5 cm level follow the forcing function with relatively short phase lag, but with a characteristic transformation from the originating rectangular step-function to sinusoidal shape. In view of this transition, phase lags will not be discussed. The emphasis will be on amplitude relations. At the beginning of the test, the general cooling trend shown by the soil temperature is hardly affected by the solar radiation pulses. When the duration of shading reached two minutes or more, the effect was great enough to overcome the initial cooling trend. At the end of the test, the variations in soil temperature to the shorter pulses are quite recognizable.

The curve representing the temperature difference between the 0.5 cm and 2.5 cm soil level shows the response to all pulses of solar radiation. For the 20-minute heating, the ΔT-amplitude is not as large as might be expected because the heat flux reaches the lower set of junctions, thus diminishing the temperature difference between the two levels. At the end of the 20-minute shading (at absolute time equal to 82 minutes), the figure shows that the temperature at 2.5 cm is slightly larger than that at 0.5 cm, indicating a significant heat loss in the layer of soil close to the surface.

The curve representing the heat flux in the soil resembles the ΔT-curve quite well. The flux plate was inoperative until minute 52 of the test. This instrument recorded an outward flux at the end of both the 20-minute and 10-minute shadings. The difference in temperature between the 0.5 cm and 2.5 cm levels does not show this reversal for the 10-minute shading, but this is tolerable considering the difference between measurement at the depth of the flux plate (1.5 cm) and

a mean-layer depth between levels of 0.5 and 2.5 cm. The shadings of duration below 10 minutes did not permit heat flux toward the surface at the 1.5 cm level.

2.5 Discussion of Errors

The method of recording the simultaneous response of the various elements required that the data be read from the multichannel visicorder chart. A certain amount of error is present in reading the paper trace. Also there is the tendency to manufacture deviations in the trace when such are desired. However, it is felt that such errors are small and in no way invalidate the result of the experiment, with the possible exception of the one- and two-minute shading durations.

The largest error persistent throughout the experiment is undoubtedly in the measurement of air temperatures. The presence of natural fluctuations of wind produced unsteady signals from the two types of sensors measuring air temperature.

In general, the results of this experiment are not so dependent on the absolute values obtained but rather on the relative responses of all the instruments to the same forcing functions.

2.6 Data Evaluation and Comparison with Theory

2.6.1 Albedo estimates

The simultaneous measurements of solar radiation and net radiation provide a basis for estimates of the surface albedo. The equation for net radiation permits us to express the albedo (α) of the surface as follows:

$$\Delta N = \Delta S(1 - \alpha); \quad \text{or,} \quad \alpha = 1 - \Delta N/\Delta S , \tag{1}$$

where ΔN is the amplitude of the net radiation (i.e., the difference in net radiation between shaded and exposed conditions) and ΔS is the amplitude of the solar radiation. The values of albedo for the three days are not the same, although the values computed at different times for the individual days are very consistent. A relationship seems to exist between the albedo and the moisture content of the soil. On October 24, the soil contained the smallest amount of moisture and the corresponding mean albedo and its standard deviation was $23 \pm 1.6\%$. On October 17, with larger moisture content, the albedo was $15 \pm 3.8\%$ and on November 3, with the largest moisture content, $9 \pm 2.3\%$. It is reported in the literature that the albedo of various soils decreases with the moisture content.

Figure 2

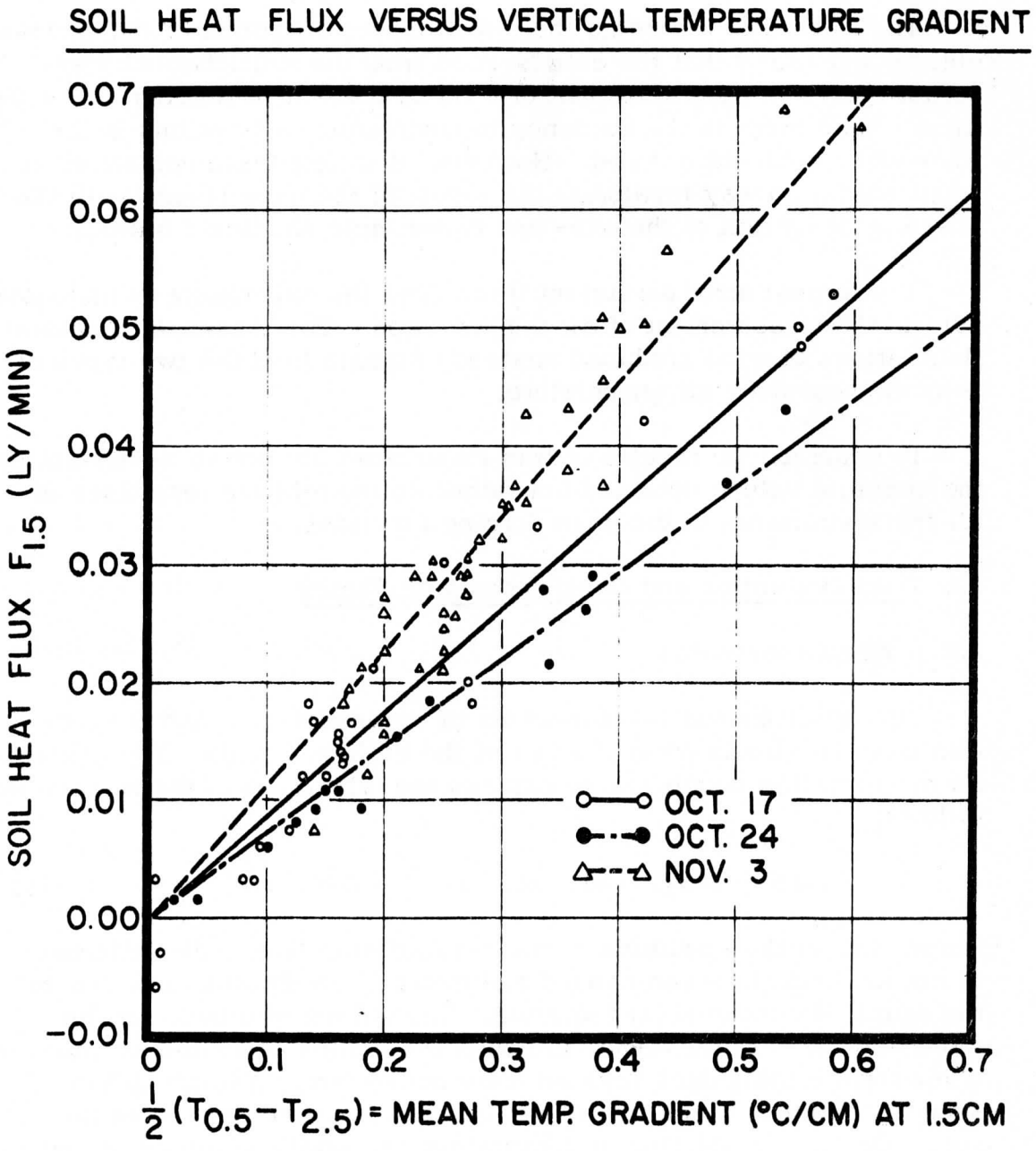
SOIL HEAT FLUX VERSUS VERTICAL TEMPERATURE GRADIENT
SOIL HEAT FLUX $F_{1.5}$ (LY/MIN)
0.07
0.06
0.05
0.04
0.03
0.02
0.01
0.00
-0.01
0
0.1
0.2
0.3
0.4
0.5
0.6
0.7
OCT. 17
OCT. 24
NOV. 3
$\frac{1}{2}(T_{0.5}-T_{2.5})$ = MEAN TEMP. GRADIENT (°C/CM) AT 1.5CM

2.6.2 Determination of soil heat conductivity

The heat conductivity (ly/min per deg/cm) of the soil was obtained graphically by plotting the instantaneous values of soil heat flux (ly/min) at the 1.5 cm level versus half the difference in temperature between the 0.5 cm and 2.5 cm levels. The heat conductivity (λ) is defined in the equation

$$\lambda = -F/T' , \quad \text{or} \quad F = -\lambda T' \qquad (2)$$

where F is the heat flux, and T' the vertical temperature gradient (°C/cm). Fig. 2 shows the data points obtained from shading experiments on the three different days. The slope of the lines of best fit result in the following λ values: 0.00122 for October 24, 0.00146 for October 17, and 0.00191 for November 3, where, for convenience, the λ units are ly/sec per deg/cm.

The soil at the site was identified as a silt loam. Carter (1951) has found that λ for various silt loams ranges from 0.0006 for dry conditions to 0.0040 for wet conditions (30% moisture). This indicates that the soil heat conductivity increases with increasing moisture content. The work of Patten (1909) substantiates this conclusion.

Table 2 shows the relationship between the observed λ and the total amount of rainfall for the period of seven days preceding each test day. The actual soil moisture content was not determined at the time of the test; however, this table provides an indication of the amount of moisture present in the soil. An increase of the λ value with increasing soil moisture is concluded.

Table 2. Soil heat conductivity and total rainfall for the seven days preceding the dates of the experiment.

Date	Rainfall	Conductivity
October 24	0.05 inches	0.00122 ly/sec per deg/cm
October 17	0.25 inches	0.00146 ly/sec per deg/cm
November 3	2.50 inches	0.00191 ly/sec per deg/cm

2.6.3 Extrapolation of soil response to the surface

Since there was no independent measurement of the temperature of the soil surface, it became necessary to estimate this value from

Figure 3

AMPLITUDE RATIO (Soil Heat Flux at 1.5 CM / Net Radiation) Vs. SHADING PERIOD

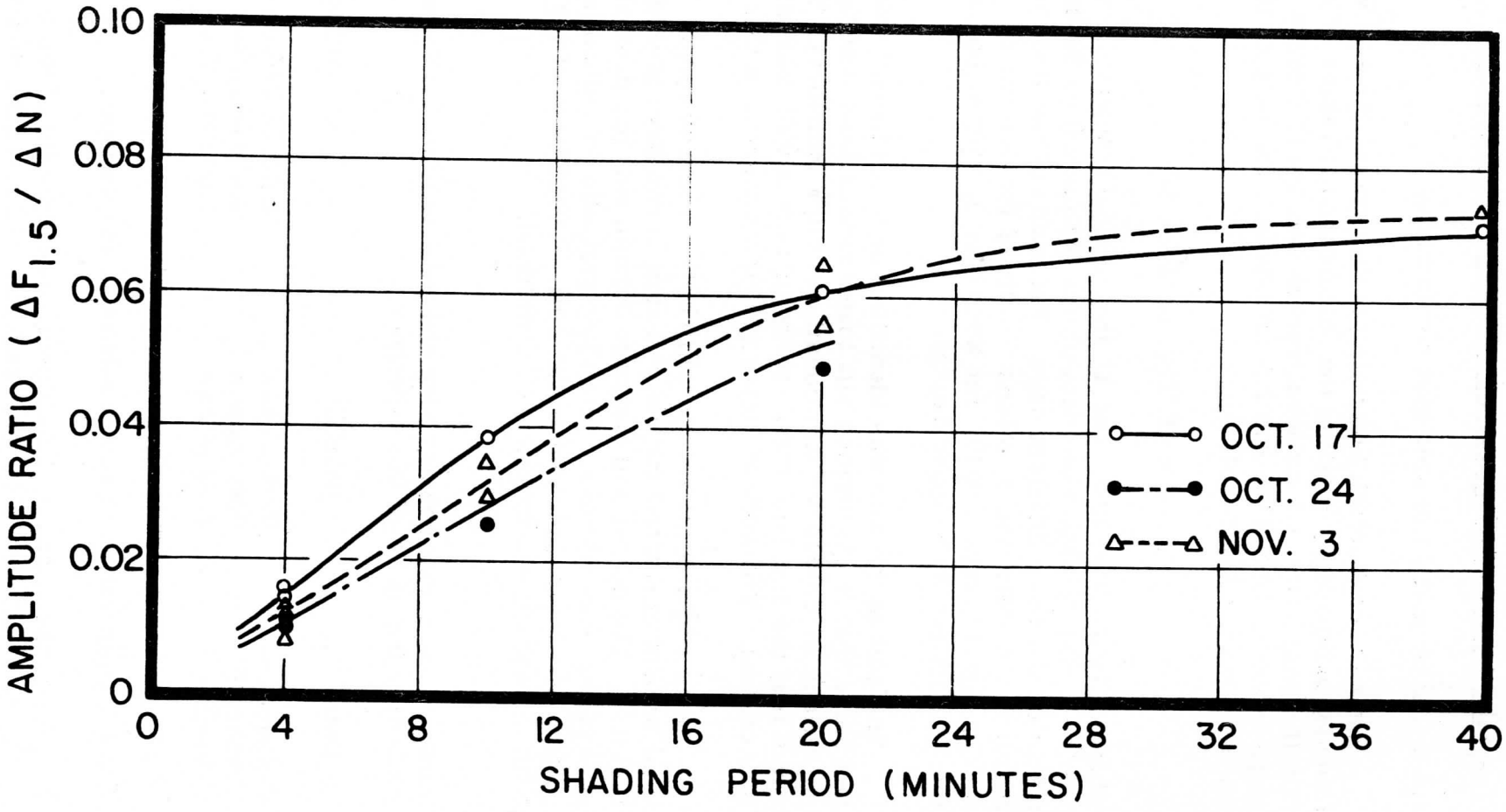

the observed temperature at the 0.5 cm depth. In addition, the value of the soil heat flux at the surface is also required and may be calculated knowing the heat flux at 1.5 cm. For simplicity, the well-known classical solution of the thermal diffusion equation for homogeneous soil will be used. The equation for the two above computations is

$$\log_e (\Delta X_0 / \Delta X_z) = z \sqrt{n/2K} \qquad (3a)$$

where ΔX_0 is the amplitude (of temperature or flux) at the surface, ΔX_z is the amplitude (of temperature or flux) at the level z, n is frequency $= 2\pi/T$ where T is the period, K is thermal diffusivity $= \lambda/c\,(cm^2/sec)$, c is volumetric heat capacity (cal/deg per cm^3).

An average value of $c = 0.4$ has been assumed, and λ-values for the individual days as derived from Fig. 2.

To determine the soil temperature at the surface, equation (3a) becomes

$$\log_e (\Delta T_0 / \Delta T_{0.5}) = 0.5 \sqrt{n/2K} \qquad (3b)$$

For the heat flux at the surface, equation (3a) gives

$$\log_e (\Delta F_0 / \Delta F_{1.5}) = 1.5 \sqrt{n/2K} \qquad (4)$$

where $\Delta T_{0.5}$ and $\Delta F_{1.5}$ are the observed amplitudes.

Figure 3 illustrates how the amplitude of the heat flux in the soil at 1.5 cm varies with the frequencies of the radiation pulse. The amplitude of the soil heat flux (ΔF_0) has been divided by the value of the net radiation amplitude (ΔN) in order to facilitate a comparison of data for the three days. The data presented in Table 1 was used for the evaluation of ΔF_0 described above.

The ratio of the air temperature amplitudes to the estimated soil surface temperature amplitudes is shown in Figure 4, which indicates that this ratio is very large, especially for the energy pulses of higher frequency. This result is due to the fact that the air temperature amplitude was found nearly independent of the frequency of the forcing function as shown in Fig. 1. Possible explanations for this result are presented in the following section.

2.6.4 Comparison with theory

A theoretical model for the response of the two-layer system (soil-air) to harmonic energy waves was discussed by Lettau (1951).

Figure 4

AMPLITUDE RATIO OF AIR TEMPERATURE AT 5 CM (ΔT_A, °C) AND SOIL SURFACE TEMPERATURE (ΔT_O, °C) VERSUS SHADING PERIOD

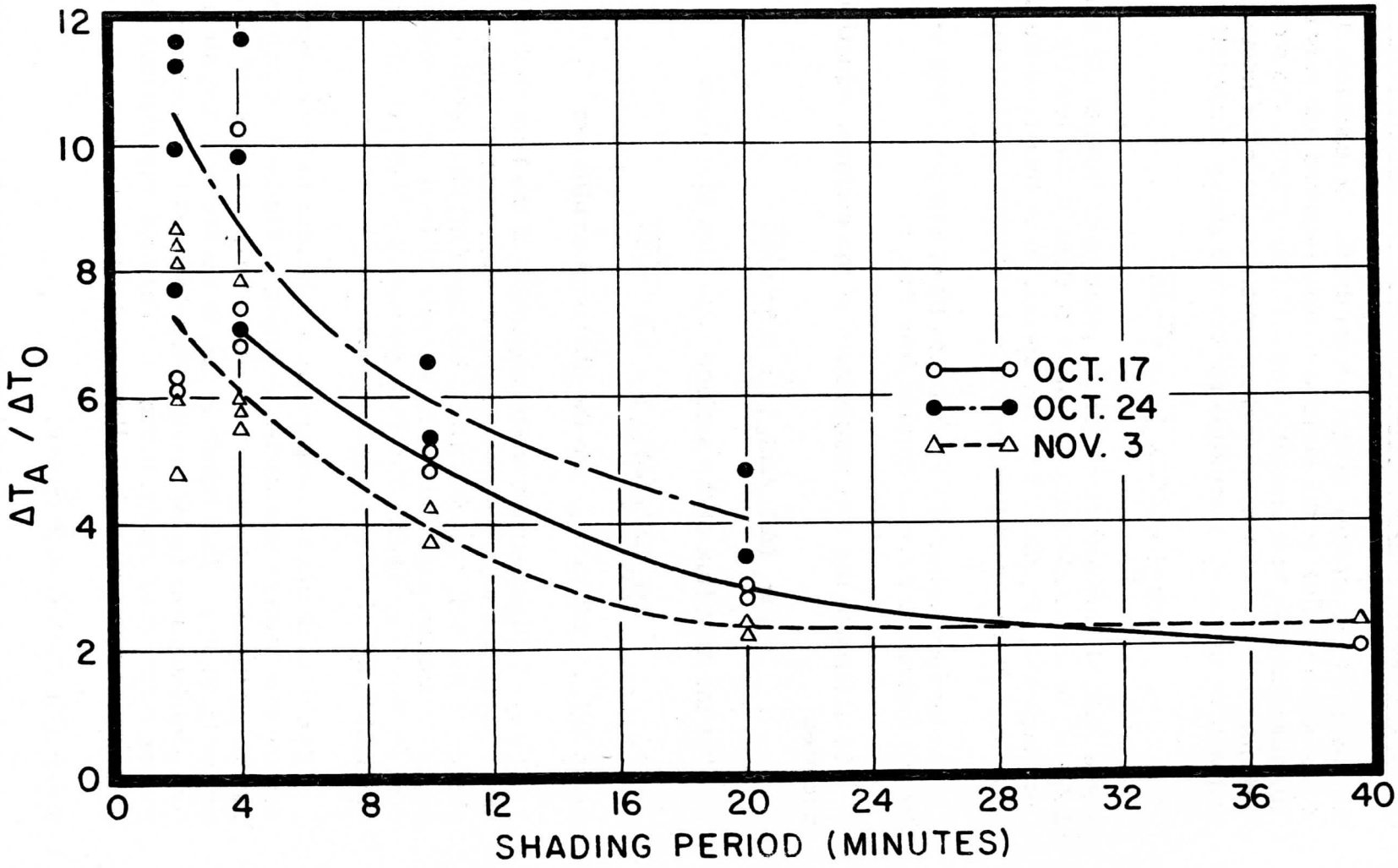

He has expressed the soil surface temperature amplitude as a function of frequency, and the amplitude (u_0) of the energy available for transformation to sensible heat only. If this model is applied to natural soil, the net radiation amplitude must be reduced by the portion of energy used for evaporation. In Figure 5, the three theoretical curves illustrate the soil surface temperature amplitude as a function of the period of the forcing function. These curves are labeled with the values assumed for the soil heat conductivity (λ) and adiabatic mixing velocity (w^*) which measures, in Lettau's model, the diffusivity of the air.

Another parameter in Lettau's model is the aerodynamic surface roughness (z_0). A constant value of $z_0 = 0.5$ cm was used. The values for λ correspond to existing soil conditions for the three days; the values of w^* are estimated from measurements of the wind speed at two feet above the ground and the maximum wind speeds determined prior to the tests by the hot-wire anemometer. Within tolerable error limits, the curve labeled $w^* = 10$ cm/sec applies to October 24, $w^* = 20$ cm/sec to October 17, and $w^* = 40$ cm/sec to November 3.

Fig. 5 also shows the experimental results obtained on the three days, in a plot of the amplitude ratio of soil surface temperature to net radiation. Note should be made of the different scales used for the ordinates of experimental and theoretical curves. Within tolerable error limits the general trend of the experimental results is similar to that predicted by the theory. Consequently the discrepancy in the magnitudes between the predicted and experimental values can be attributed to the evaporation process which is not considered in the theoretical model. A quantitative discussion of evaporation effects is presented in the following section.

The theoretical amplitude of soil heat flux at the surface relative to that of available energy for conduction of sensible heat ($\Delta F_0 / u_0$) is shown in Figure 6. The upper curve is computed for soil heat conductivity equal to 0.00122 (ly/sec per deg/cm) and an adiabatic mixing velocity of 10 cm/sec, i. e., the values corresponding to conditions of October 24; the other, for $\lambda = 0.00191$ and $w^* = 40$ corresponding to November 3. The curve for October 17, for $\lambda = 0.00146$ and $w^* = 20$, would lie between these two.

Fig. 6 illustrates the difference between the theoretical values and those obtained experimentally on the three days. The amplitude ratio of soil heat flux at the surface to net radiation, as determined experimentally, is in general approximately 20%. However, for the

Figure 5

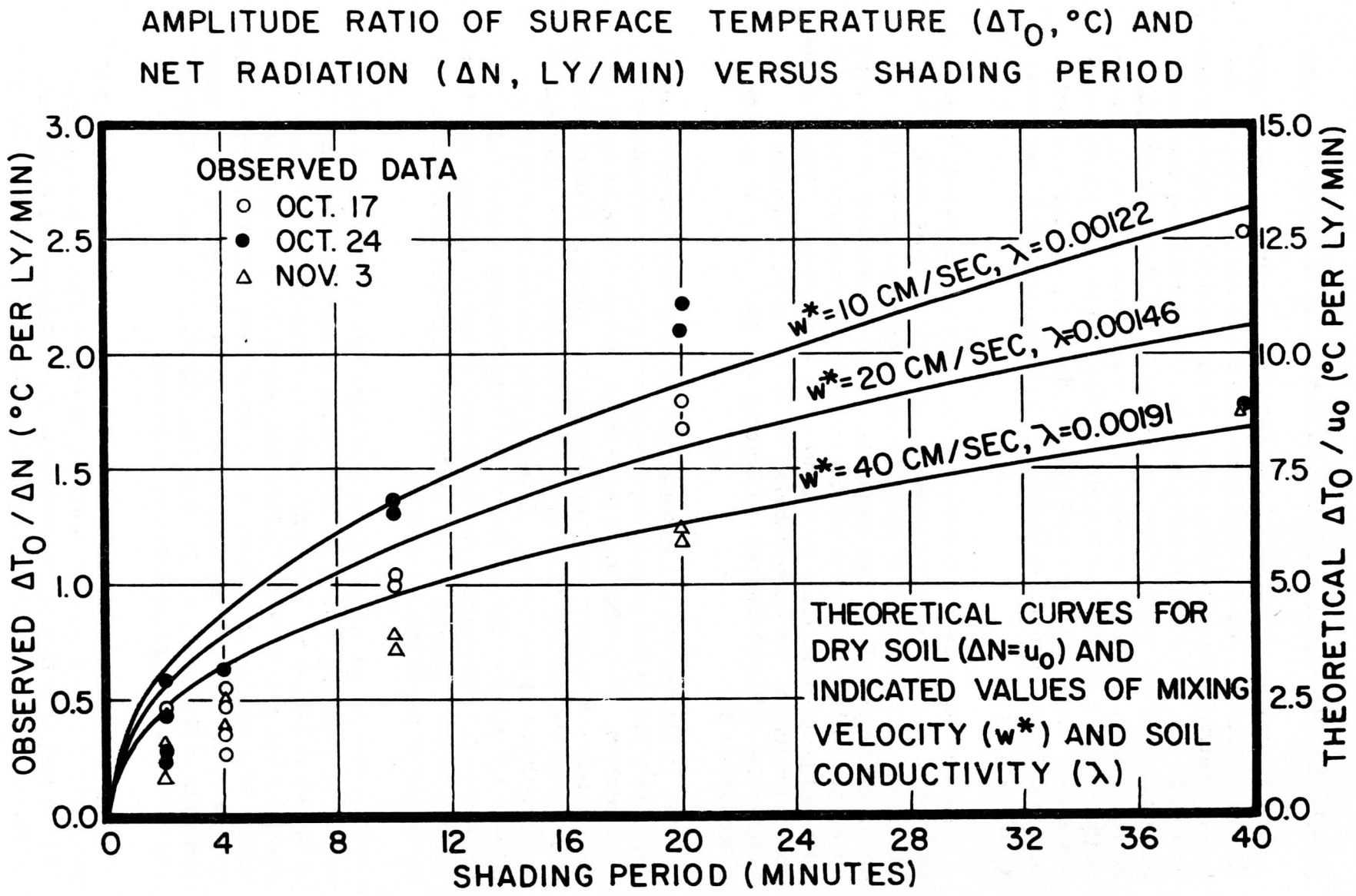
AMPLITUDE RATIO OF SURFACE TEMPERATURE (ΔT_0, °C) AND NET RADIATION (ΔN, LY/MIN) VERSUS SHADING PERIOD
OBSERVED DATA
OCT. 17
OCT. 24
NOV. 3
w^*=10 CM/SEC, λ=0.00122
w^*=20 CM/SEC, λ=0.00146
w^*=40 CM/SEC, λ=0.00191
THEORETICAL CURVES FOR DRY SOIL ($\Delta N = u_0$) AND INDICATED VALUES OF MIXING VELOCITY (w^*) AND SOIL CONDUCTIVITY (λ)
OBSERVED $\Delta T_0 / \Delta N$ (°C PER LY/MIN)
THEORETICAL $\Delta T_0 / u_0$ (°C PER LY/MIN)
SHADING PERIOD (MINUTES)
0.0
0.5
1.0
1.5
2.0
2.5
3.0
0
4
8
12
16
20
24
28
32
36
40
0.0
2.5
5.0
7.5
10.0
12.5
15.0

assumed soil and air parameters for the three days and the frequencies of the forcing function used in the experiment, the theory predicts that more than 70% of the energy available for sensible heat transfer will be directed into the soil. The discrepancy between the values determined experimentally and those predicted by theory are attributed here also to the evaporation process occurring at the soil surface.

2.7 Conclusions

2.7.1 Apparent deviation from two-layer theory

Lettau's theoretical model assumes that the lower medium (soil) is homogeneous, separated from the upper medium (air) by a horizontal surface of discontinuity. Possibly the site upon which the experiment was performed did not represent satisfactorily a simple two-layer system. With a grass height of approximately two inches, an additional layer might be postulated between the soil and air. The presence of a third layer, consisting of a mat of grass, quite possibly could have contributed to the unexpectedly large air temperature amplitudes, and their small variation with the period of the incident radiation.

Owing to the late season (low radiation intensities), preliminary experiments performed on a grass-free surface were inconclusive in establishing a better understanding of the processes involved. On the other hand, it can be doubted that the method of elimination of radiation errors from the air temperature sensors was satisfactory. A more refined technique for the measurement of air temperature will supply more dependable data to resolve the existing uncertainties.

2.7.2 Evidence of evaporation processes

In Section 2.6.4 the discrepancy between the theoretical and experimental values shown in Fig. 5 was attributed to the evaporation process. The ratio existing between the two curves for individual days indicates that only approximately 20% of the net radiation has been converted to sensible heat. This suggests that 80% of the net radiation energy is being used for evaporation. In view of ample soil moisture at the test site, this ratio agrees fairly well with that obtained on occasion (days with relatively high, but absolutely rather moderate, soil moisture) by Suomi and Halstead at O'Neill, Nebraska. Reference is made to H. Lettau and B. Davidson (1957), Vol. II, Tables 7.3.a., see Table 3. Tanner and Pelton (1960) found that evaporation from a good alfalfa-brome cover may be greater than or equal to 90% of the net radiation. With advective heating they found that evaporation may actually exceed net radiation.

Figure 6

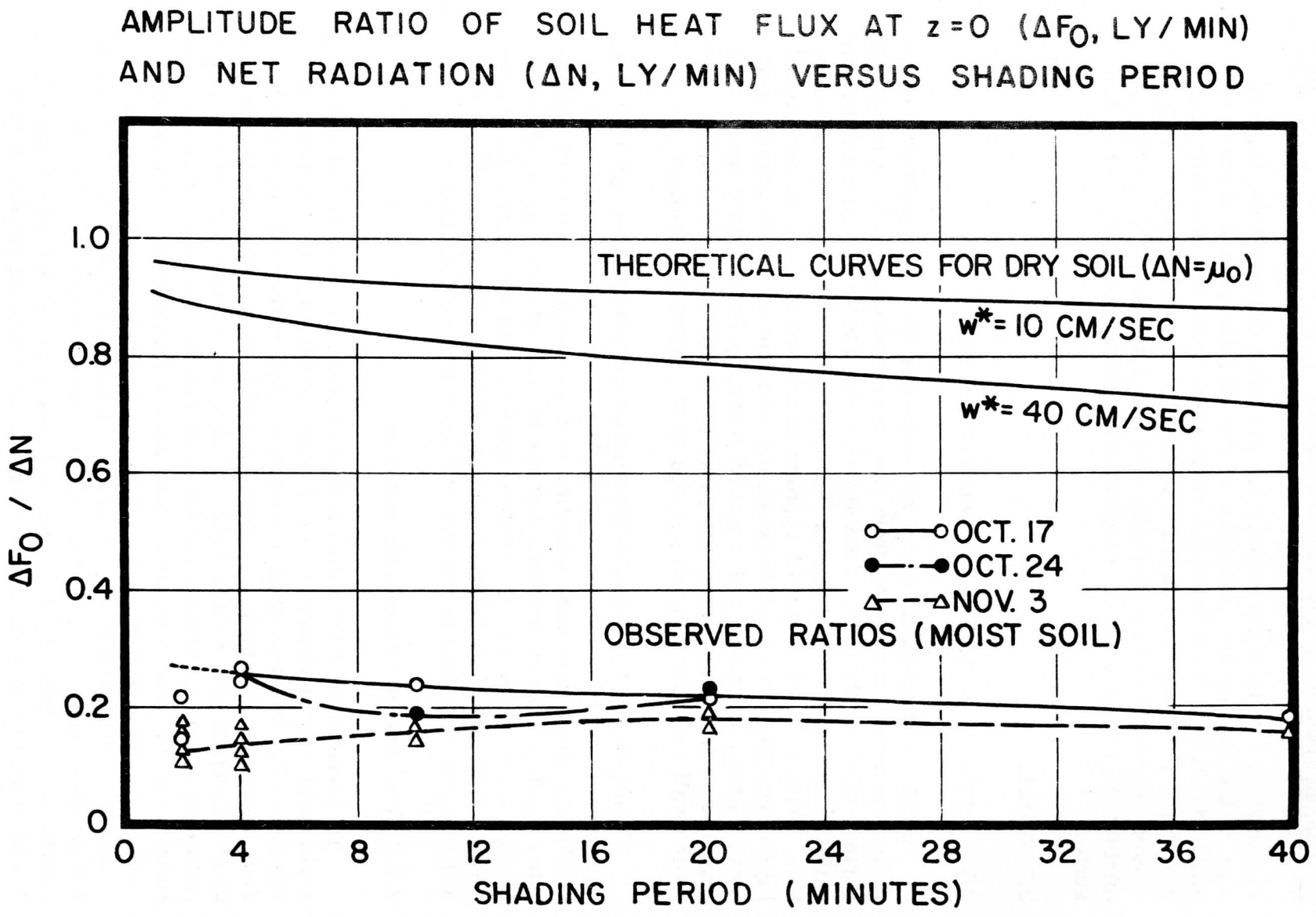
AMPLITUDE RATIO OF SOIL HEAT FLUX AT z=0 (ΔF_0, LY/MIN) AND NET RADIATION (ΔN, LY/MIN) VERSUS SHADING PERIOD
THEORETICAL CURVES FOR DRY SOIL ($\Delta N=\mu_0$)
w*= 10 CM/SEC
w*= 40 CM/SEC
OCT. 17
OCT. 24
NOV. 3
OBSERVED RATIOS (MOIST SOIL)
ΔF_0 / ΔN
1.0
0.8
0.6
0.4
0.2
0
0
4
8
12
16
20
24
28
32
36
40
SHADING PERIOD (MINUTES)

Table 3. Net radiation (N_0) and evaporation (E_0) in millily/min, averaged for hours 10 A. M. to 2 P. M. at O'Neill, Nebraska, according to Suomi and Halstead.

	Suomi			Halstead		
Date	N_0	E_0	100 E_0/N_0	N_0	E_0	100 E_0/N_0
August 9, 1953	746	397	53	826	464	56
August 14, 1953	780	449	58	857	543	64

The estimate of evaporation following the original approach outlined by Lettau (1952) is a promising aspect of the thermal response experiment. The data in Fig. 6 confirm the result that approximately 80% of the net radiation energy was used for evaporation.

The understanding of the evaporation process, too, requires an investigation concerning the validity of the two-layer system discussed above. Postulating a third layer of grass greatly increases both the surface area for exchange of sensible heat and evaporation. Further experiments are necessary to define the processes occurring over a grass surface.

2.8 Recommendations

To perform an experiment aimed at investigating the two-layer conduction processes, it will be necessary to insure that truly two mediums only are present. Therefore, such an investigation will be best performed on a soil surface which is free of vegetation, thus eliminating a possible third or buffer layer. To provide data for comparison with the theory of two-layer heat conduction, a further restriction is advisable. As reported in the body of this report the process of evaporation apparently involves a large fraction of net radiation, not considered in the theoretical study. Evaporation is eliminated by performing a similar experiment on a moisture-free medium. Dry concrete or asphalt would conveniently provide such a surface.

A more detailed investigation of the evaporation processes as related to the period of the energy wave would be interesting. Comparisons with direct methods of determining the evaporation, perhaps, performing shading experiments on lysimeters (a sensitive weighing system) or one permitting active control of the moisture flux are promising possibilities.

Further investigations similar to that reported here should incorporate an independent measurement of soil surface temperature, either by contact thermometers, or bolometers. In addition, the measurement of air temperature without radiation error is a necessity. An aspirated thermocouple surrounded by a high reflecting cylinder might be useful but has the undesirable features of casting a shadow upon the underlying surface and disturbing the air by ventilation.

Experiments along the lines discussed here could add greatly to an understanding of the transformation of energy occurring at the surface of the earth which is one of the most important micrometeorological processes.

References

Baumgartner, A.: Numerical calculation of Lettau's synthetic climatology for short periods of the energy wave. An unpublished manuscript. 1959.

Carter, C. L.: "Soil Temperature, Moisture Content, and Thermal Properties." University of Tennessee, Eng. Expt. Stn. Bull. No. 15. June 1951.

Lettau, H.: "Theory of Surface Temperature and Heat-Transfer Oscillations near a Level Ground Surface." Transactions American Geophysical Union 32, 189. 1951.

Lettau, H.: "Synthetic Climatology." Berichte des Deutschen Wetterdienstes No. 38; Bad Kissingen, Germany. 1952.

Lettau, H., and Davidson, B. (editors): "Exploring the Atmosphere's First Mile" (two volumes). Pergamon Press Inc., New York and London. 1957.

Lettau, H.: "Research Problems in Micrometeorology." Final Report Contract DA-36-039-SC-80063. Meteorology Department, University of Wisconsin, September 1959. U. S. Army Electronic Proving Ground, Fort Huachuca, January 1960.

Patten, H. E.: "Heat Transference in Soils." U. S. Dept. of Agriculture, Bureau of Soils, Bulletin No. 59. 1909.

Suomi, V. E., Fransilla, M., and Islitzer, N.: "An Improved Net Radiometer." Journal of Meteorology 11, 276. 1954.

Tanner, C. B., and Pelton, W. L.: "Potential Evapotranspiration Estimates by the Approximate Energy Balance Method of Penman." Journal of Geophysical Research 65, 10. October 1960.

3

Derivation of Roughness Parameters from Wind Profile Data Above Tall Vegetation

Ernest Kung

Department of Meteorology
University of Wisconsin

Abstract. Wind profile measurement above tall vegetation (including corn, brush fields, orchards, and fir forest) reported in the literature are reanalyzed. The logarithm of the roughness parameter z_0 is found to increase in proportion to the logarithm of vegetation height; however, the probable error of this regression line is relatively large. The uncertainties of the analysis are discussed, and explained by certain unreliabilities of anemometry.

3.1 Introduction

The roughness length (z_0, cm), the zeropoint-displacement (d, cm), and the surface stress (τ_0, dynes/cm^2) are the three wind profile parameters in the study of the atmosphere near the ground. In specifying the degree of roughness of a given surface, we must consider at least two factors: the height of protuberance, and spacing between individual elements. Thus, the wind profile parameter will be determined by the structure and nature of vegetation cover at the surface.

Deacon (1953) has quoted roughness parameter values for various natural surfaces which are summarized in Table 1. His study referred to surfaces without natural vegetation and surfaces of low vegetation. In this study it was attempted, through the analysis of wind profile data reported in the literature, to extend Deacon's tabulation to surfaces of various kinds of relatively tall vegetation.

Table 1. Roughness parameters of various surfaces — adopted from Deacon (1953).

Type of Surface		z_0 (cm)
Smooth mud flats		0.001
Smooth snow on short grass		0.005
Sea		0.02
Desert near Karachi		0.03
Snow surface, Canada		0.10
Mown grass surfaces		
Grass length 1.5 cm		0.2
Grass length 3.0 cm		0.7
Grass length 45 cm:	V_2 = 2 m/sec	2.4
	V_2 = 6 to 8 m/sec	1.7
Long grass, 60 to 70 cm high:		
	V_2 = 1.5 m/sec	9.0
	V_2 = 3.5 m/sec	6.1
	V_2 = 6.2 m/sec	3.7
Downland at Porton:	Winter	1 to 2
	Summer	2 to 4

3.2 Methods

In the fully-rough regime, the wind velocity profile under neutral conditions of stability is related to the three wind profile parameters by the equation (Lettau, 1957)

$$V = V^* \ln[(z + d + z_0)/z_0] \quad \text{(cm/sec)},$$

where V = wind velocity (cm/sec) at height z, and $V^* = k^{-1}\sqrt{\tau_0/\rho}$ $= 2.5\sqrt{\tau_0/\rho}$ = friction velocity (cm/sec), with ρ = air density (g/cm^3) and $k = 0.4$ = universal Karman number. For convenience, let $D = d + z_0$ (cm).

A curve-fitting is most satisfactorily achieved by a least square method (Lettau, 1957) in which the parameters are determined such that the sum of the error squares is minimized,

$$\varepsilon_i = V_i - V^* \ln[(z_i + D)/z_0] \; ;$$

$$\sum \varepsilon_i = 0 \; ; \quad \text{and} \quad \sum \varepsilon_i^2 = \text{minimum} \; .$$

For practical computations, a numerical trial-and-error method may be used. One assumes an arbitrary D-value which is equal to or smaller than zero, and repeats the computation for other D-values, until that D is determined for which the sum of the error squares has the least value. When the bar indicates the mean for the i observation levels (z_i), the following abbreviations are introduced:

$$X_i = V_i - \overline{V} \; ; \quad Y_i = \ln(z_i + D) - \overline{\ln(z + D)} \; ;$$

$$S_{xx} = \sum X_i^2 \; ; \quad S_{xy} = \sum X_i Y_i \; .$$

Then, the equations,

$$\varepsilon_i = X_i - V^* Y_i \; ; \quad \text{and} \quad V^* = S_{xy}/S_{xx}$$

give the deviations and their sum of squares varies directly as a function of D.

After determining the least square D-value, the roughness parameter, z_0, is computed by the equation

$$\ln z_0 = \overline{\ln(z + D)} - \overline{V}/V^* \; .$$

Table 2. Evaluation of wind profile data for relatively extreme surface roughness types.

Surface cover	Plant height (m)	Anemometer levels (m)	Computed values of $\overline{V}$ (m/sec)	z_0 (cm)	d (cm)	τ_0 (dynes/cm^2)
Corn field	0.7 to 0.9	1.6, 2.4, 3.2, 4.0, 4.8, 5.6, 6.4	3.95	6.4	- 88.4	2.2
Brush field	1.3	1.5, 1.8, 2.4, 3.7, 4.3, 4.6, 6.4	3.44	15.7	- 125	3.8
Orange orchard	3.3	4.3, 5.8, 7.3, 8.8, 10.4 12.6, 15.2	1.36	24.1	- 332	0.4
Orange orchard	3.3	4.3, 5.8, 7.3, 8.8, 10.4, 12.6, 15.2	2.29	122	- 244	3.2
Fir forest	5.5	8.0, 9.8, 12.2, 16.0	2.82	190	- 190	4.9
Fir forest	5.5	3.0, 9.8, 12.2, 16.0	1.15	399	- 399	2.4
Idaho forest*	24.4	25.3, 34.1, 47.5	4.11	1847	-1847	83.1
Idaho forest	24.4	25.3, 34.1, 47.5	1.60	1347	-1637	6.8

*Composed of spruce, hemlock and Douglas fir.

Then the relation $D = d + z_0$ gives the zeropoint-displacement, d, and the equation

$$V^* = 2.5 \sqrt{\tau_0/\rho}$$

gives the surface stress parameter, τ_0. Air density ρ is assumed to be 0.0012 g/cm^3.

3.3 Data

A search of the literature revealed that wind profile measurements over tall vegetation are very rare. In this computation, data from five different sources — The Johns Hopkins University Laboratory of Climatology (1952), Fons (1940), Kepner, Boelter and Brooks (see Poppendiek, 1949), Baumgartner (1956, 1957), and Gisborne (see Poppendiek, 1949) — are used to obtain roughness parameter values for corn field, brush field, orange orchard, fir forest, and Idaho forest. The zeropoint-displacement and surface stress are also computed in reference to roughness parameter.

As the wind profile will be logarithmic only under neutral stability conditions, attention was paid to selecting wind profile data for adiabatic hours, if it was possible.

3.4 Roughness Parameter Approximation

The Johns Hopkins University (1952) wind velocity data for seven levels from 1.6 to 6.4 m height at Shirley Field Station, New Jersey, was used to compute roughness parameter for a thickly planted corn field before tasseling when the plant height was about 0.7 to 0.9 m. The data in Table 2 refer to the wind velocity profile at 1800 to 1900 local time, July 2, when the lower atmosphere was adiabatic. The computed roughness parameter, z_0, was 6.4 cm with $d = -88.4$ cm and $\tau_0 = 2.2$ dynes/cm^2. This z_0 value agrees closely with Deacon's (1953) value for long grass.

The wind velocity measurement by Fons (1940) above a brush field for seven levels from 1.5 to 6.4 m in California yielded a roughness parameter value of 15.7 cm with $d = -125$ cm and $\tau_0 = 3.8$ dynes/cm^2. The brush was manzanita and snowbrush of 1.3 m average height.

Wind velocities for seven levels from 4.3 to 15.2 m were measured above an orange orchard by Kepner, Boelter and Brooks (Poppendiek, 1949). Data were reported in five groups. Group IV ($\overline{V} = 1.36$ m/sec) and group V ($\overline{V} = 2.29$ m/sec) of relatively high mean velocity were

selected for the analysis. On the average the orange trees were 3.3 m tall and had a diameter of 3.3 m. The wind observations were made at night under temperature inversion conditions. The roughness parameter value obtained from group IV was 24.1 cm with $d = -332$ cm and $\tau_0 = 0.4$ dynes/cm^2 which seemed comparable with the values obtained by Deacon (Table 1) for other natural coverages. However, the computed roughness parameter value from group V was 122 cm with $d = -243$ cm and $\tau_0 = 3.2$ dynes/cm^2, which seemed unreasonably large. This might be a spurious effect due to the temperature inversion condition under which these measurements were made.

Two sets of wind velocity data above fir forest were selected from Baumgartner's work (1956, 1957). One set represents the average wind velocity profile for 1700 to 1800 local time from June 28 to July 8 of 1952, and another set represents the average for 1800 to 2100 local time from July 9 to July 14 of 1952. In both cases, the data refer to isothermal condition. The tree height was about 5.5 m. The four anemometer levels were from 8 to 16 m. The computed z_0 value for the first set was 190 cm with $d = -190$ cm and $\tau_0 = 4.9$ dynes/cm^2; for the latter $z_0 = 399$ cm with $d = -399$ cm and $\tau_0 = 2.4$ dynes/cm^2 (Table 2). Both z_0 values are unexpectedly large even though the computation was carried only to $D = 0$ in order to avoid positive D-values.

Two groups of Idaho forest wind velocity data were presented by Gisborne (see Poppendiek, 1949) for three anemometer levels from 25.3 m to 47.5 m. The average tree height was about 24.4 m for spruce, hemlock, and Douglas fir. The computed roughness parameter for group I was 1847 cm, with $d = -1847$ cm and $\tau_0 = 83.1$ dynes/cm^2; for group II the computed roughness parameter value was 1347 cm with $d = -1637$ cm and $\tau_0 = 6.8$ dynes/cm^2 (Table 2). In both cases, the variation of D was restricted to positive values only. The unreasonably large roughness parameters suggested unreliability of the data. The large τ_0 value for group I does not seem to be realistic.

3.5 Reliability of the Data

The results of roughness parameter computation will strongly depend on the reliability of the anemometer data.

The Johns Hopkins University (1952) data for corn field include seven anemometer levels. Special care was taken to use only the most reliable and matched anemometers. The error distribution in the least-square computation was found to be very even. To check the reliability of the roughness parameter computation, the data were

divided into two parts: the first part contained the four z_i with $i = 1, 3, 5,$ and 7; and the second part, the three z_i with $i = 2, 4, 6$. The roughness parameter was computed for each group separately, and the results are listed below.

Levels (m)	z_0 (cm)	d (cm)	τ_0 (dynes/cm^2)
1.6, 2.3, 4.8, 6.4	3.0	-106	1.6
2.4, 4.0, 5.6	14.7	- 57.7	3.2
All 7 levels	6.4	- 88.4	2.2

The difference in computed roughness parameter values from the complete data was considerable. The probable error of the result from the complete data may be expressed in terms of a factor which can vary from $\frac{1}{2}$ to 2.

The same treatment was applied to Fons' (1940) data for brush field. The original set contained seven levels, and the two divided parts had four and three levels each. The results are listed below.

Levels (m)	z_0 (cm)	d (cm)	τ_0 (dynes/cm^2)
1.5, 2.4, 4.3, 6.4	7.3	-135	2.5
1.8, 3.7, 4.6	87.6	- 87.6 (D=0)	13.7
All 7 levels	15.7	-125	3.8

The differences in computed roughness parameter value are such that the probable error may be expressed by a factor which may vary from $\frac{1}{4}$ to 4.

Both groups of Baumgartner's (1956, 1957) data for fir forest contained only four anemometer levels. On the basis of the error distribution, the third level seemed inaccurate. Therefore this anemometer level was omitted and z_0 was computed for the remaining three levels. The results are listed below.

The group II data showed some improvement by eliminating the third level, though the z_0 value still remained larger than expected.

However, group I data was not affected by elimination of the third level.

Levels (m)	z_0 (cm)	d (cm)	τ_0 (dynes/cm^2)
Group I			
8.0, 9.8, 12.2, 16.0	190	-190 (D=0)	4.9
8.0, 9.8, 16.0	192	-192 (D=0)	5.0
Group II			
8.0, 9.8, 12.2, 16.0	399	-399 (D=0)	2.4
8.0, 9.8, 16.0	203	-493	1.4

Since the Idaho forest data by Gisborne had only three levels it was impossible to omit any information from the data.

This study leads to the conclusion that caution should be used in future experiments of this nature. The considerable unreliability of previous data may include the construction, exposure, condition of the anemometer. It is suggested that at least seven levels are required for a reliable roughness parameter approximation. Wind data at less than four levels must be considered inconclusive.

3.6 Concluding Remarks

Plotting the roughness parameter values versus height of natural vegetation on a logarithmic graph, a straight regression line can be assumed. It may be stated that the logarithm of roughness parameter is proportional to the logarithm of height of natural vegetation. The regression line is expressed by

$$\log z_0 = -1.24 + 1.19 \log h$$

where z_0 and plant height h are in cm; see Fig. 1, Section 5.4.

The surface stress, τ_0, can be computed independently to assign the roughness parameter value or check the reliability of the data for the specific plant height.

References

Baumgartner, A.: Untersuchungen über den Wärme — und Wasserhaushalt eines jungen Waldes. Berichte des Deutchen Wetterdienstes No. 28 (Band 5), 1956.

Baumgartner, A.: Beobachtungswerte und weitere Studien zum Wärme — und Wasserhaushalt eines jungen Waldes. Universität München — Meteorologisches Institut, Wissenschaftliche Mitteilungen No. 4, 1957.

Deacon, E. L.: Vertical profiles of mean wind in the surface layer of the atmosphere. Geophysical Memoirs 2, No. 91, 1953.

Fons, W. L.: Influence of forest cover on wind velocity. Journal of Forestry 38, No. 6, 1940.

The John Hopkins University Laboratory of Climatology: Publications in Climatology V, No. 7, 1952.

Lettau, H. H.: Computation of Richardson Numbers, Classification of Wind Profiles, and Determination of Roughness Parameters. Section 7.4 in Vol. I of Exploring the Atmosphere's First Mile (H. Lettau and B. Davidson, editors), Pergamon Press, London and New York, 1957.

Poppendiek, H. F.: Investigation of velocity and temperature profiles in air layers within and above trees and brush. Contract N6-ONT-275, Task Order VI, NR-082-036. Department of Engineering, University of California, Los Angeles, 1959.

Scanner's note:

This page is blank.

4

Aerodynamic Drag in Tall Vegetation

Robert H. Burgy*

Department of Civil Engineering
and
Department of Meteorology
University of Wisconsin

Abstract. This report summarizes the results of a review of recent literature relating to drag forces and coefficients for tall vegetation. Results of wind tunnel tests on conifer saplings, and field tests on broad leafed trees are quoted which show that the drag coefficient decreases with increasing wind speed.

4.1 Introduction

The study by Kung — see Section 3 — reviewed the available information on wind profiles above stands of shrubs and trees. This review is directed mainly toward locating additional data on which to base calculations of roughness effects for trees.

No new wind profile data were located. However, a group of studies relating to the effects of winds in tree damage in forests from atomic blasts was disclosed. Two studies have been made, one on conifers — Sauer, Fons, and Arnold (1951) — and the other on hardwoods — Lai (1955) — wherein whole individual trees were used to measure drag in the crowns. Part of the work was done in a wind

---

*Professor R. H. Burgy, Department of Irrigation, University of California, Davis, California, on sabbatical leave during 1960-61 at the University of Wisconsin, engaged in graduate study in Civil Engineering and Micrometeorology, completed this work as a special problem assignment in course CE 280, Spring Semester 1960-61, for Professor H. Lettau.

tunnel and the bulk of the tests were made on truck-mounted tree samples moved at constant velocity while drag and other measurements were made. These tests led to studies of crown characteristics of forest types to relate crown areas to crown weights, with two additional reports being published on tree crown relationships — Storey, Fons, and Sauer (1955), and Storey and Pong (1957).

In hydrodynamic work it is convenient to express the frictional resistance of bodies immersed in flowing fluids as a "drag force," D_f, in appropriate units. This drag force is related to the dynamic pressure acting on the body by a suitable factor, the drag "coefficient," which thus gives the drag as a function of dynamic pressure on the cross-sectional area of the body exposed to the flow, as follows:

$$D_f = C_d A\rho V^2/2 \; ; \quad \text{or} \quad C_d = 2D_f / A\rho V^2$$

where C_d = drag coefficient, V = velocity, A = silhouette area and ρ = density of fluid.

The data are for single trees of various species moved through the air on a vehicle. The basic data for the conifer tests were not reported and it is not possible to make further analysis of these data, since the study was concerned with shock waves from blasts and the relationships are in nondimensional form.

Tree crown characteristics were developed to define the several types with respect to crown weights and area. In the limited scope of this review the writer has not been able to make more than very generalized comparisons to determine the resultant drag coefficients for the two tree types. Some estimates based on average values with certain assumptions concerning the trees are made to obtain an average drag coefficient.

Another study reported from Japan by Hirata (1953) includes wind tunnel investigations of tree crown drag for "models" of forest trees. Drag coefficients are reported which are of the order of 1.0. The study was also directed toward wind damage effects and is consequently of limited applicability to the problem of forest drag under normal conditions.

The thought-provoking question may be asked concerning the relationship of values measured in single tests as compared to the composite conditions in a stand of trees. Certainly the drag forces, and coefficients are applicable for the given velocity. However, the development of the boundary layer and the consequent redistribution of

the wind profile over the forest will cause marked differences in comparison with drag for a single tree. Additionally the integrated effects of uniform or variegated vegetation and existence of both primary and secondary canopies will be important in micrometeorological work; reference is made to Kutzbach's discussion, see Section 7.5.4.

The application of mass transfer concepts to the forest for micrometeorological investigations requires a considerably better understanding of the internal relationships for forests and tall vegetation than is now available.

An additional topic reviewed in this study was the effect of wind speed on drag coefficients. C_d for rigid bodies of many shapes have been reported. Flexible bodies like vegetation have rarely been studied. Some work has been done on fabrics, flags, tow targets, and parachutes, which may have some bearing on the question; see Hoerner (1951, 1958).

Sauer (1951) and Lai (1955) recognized the effect of wind on C_d and suggest that plant components may respond to increased dynamic pressure by deflecting, with a resultant variation in drag coefficient. If the plant tends to become more streamlined in shape under higher pressures the drag parameter would become commensurately smaller, making a non-linear relation between squared velocity and stress. If, however, in some plants the higher speeds will cause flutter or flapping and oscillations of the leaves and branches, then the drag may become greater and the coefficient increased.

Hirata's (1953) data show an effect of the wind speed, increasing in some species and decreasing in others. He concludes that there is no effect for the conditions of his tests and attributes the variation to errors. The trends are quite apparent and cause this writer to suspect that a relationship does exist.

Observational evidence seems to support either contention and detailed investigation must be made to resolve the question. The thought also occurs that the oscillations in grain fields, or waves moving across the stalks (seen as bending of the stalks) may be partly due to fluctuations of C_d as the stalks bend, introducing a harmonic cycle to the wind stream, which would rise and fall both in vertical position and in magnitude as the boundary layer responded to a changing surface stress. Conversely, it may well be concluded on the basis of even fragmentary evidence that any variation of drag with wind speed is, for practical purposes, of no significance in micrometeorological work.

4.2 Wind Tunnel Tests on Conifer Saplings

The data presented in the reports relating to crown drag in conifers and broadleafed (hardwood) species have been used to calculate some typical values of C_d for the conditions of the tests. Some assumptions are made of the effective area of crown exposed since the reports use the relationship of foliage and branch weights to correlate drag force with a moment-stress-dynamic pressure factor. There is some evidence to indicate that the use of foliage dry-weight is appropriate and some correlations are available. For these calculations the writer preferred to use standard terms. The basic data are not complete for the conifer tests of whole trees. Even the wind tunnel tests are not fully explained, and possible misinterpretation of the graphs may be inherent in the calculated values presented here.

For this purpose it was believed appropriate to estimate the gross silhouette area of the tree species based on some average dimensions and shapes. This is a reasonable assumption since the coefficients should be calculated on the standard terms used in hydrodynamics and aerodynamics to be meaningful.

As noted above, the tests in the wind tunnel of saplings of several conifer species are graphed using nondimensional parameters and therefore with incomplete explanation this reviewer is unable to insure the meaning of the graphs. If a correct interpretation is made, then the drag coefficients of white fir saplings for several wind speeds are as listed below. The average height was 0.6 m, the average width was 0.3 m. The average dry foliage weight was 180 grams. A gross silhouette area of 0.18 m^2 and an air density of 0.00106 g/cm^3 was assumed.

Velocity	23	15	9 (m/sec)
Drag force	2.53	1.60	0.70 (10^6 dynes)
Drag coefficient	0.41	0.60	0.72 (-)

It should be noted that these are "apparent" drag coefficients since the area is gross silhouette. As the velocity increases the tree tends to deflect downwind and this action seems to result in a more compact silhouette. It is impossible to estimate the amount of this effect on wind speed vs. drag since the reduced area of the tree must yield less drag or a higher coefficient and using the constant area

here shows a reducing coefficient. These two effects must be partially compensating.

The tests reported for the conifer trees on vehicles do not include sufficient detail or data to permit a calculation of C_d. Several attempts were made to select average values from the graphs and to relate these to the wind tunnel tests which were also plotted with the field data. These attempts have proved fruitless to this writing since the values of C_d thus obtained range from over 50 to about 3. These are believed to be meaningless due either to inaccuracy or probable erroneous interpretation of the data as presented. Inquiries have been made to the authors for more explanation of the methods used and meaning of the terms.

4.3 Field Tests on Broadleafed Trees

The tests of the broadleaf species provide more dependable results since the basic data are reported for the runs on the various trees. The values obtained for three speeds of tree moved on the truck are listed below. Assumptions were made of the tree crown area and shape as before. The total tree height was 12 to 20 m, the average crown height 7.5 m. The gross silhouette area was assumed to equal 13.5 m^2.

Velocity	23	10	6	(m/sec)
Drag force	133	51	24	(10^6 dynes)
Drag coefficient	0.31	0.76	0.82	(-)

It should be noted that the use of gross tree area is not representative of the actual situation since the broadleafed species are relatively open in structure. The C_d values thus calculated show the reduction with increase in velocity as did the conifer saplings.

There is no rational way in which this deflection of the tree form and streamlining can be identified from the data presented in these studies. The writer is confident that a means can be found to measure this effect and to isolate the relation of wind speed and drag.

In both conifer and broadleaf tests some specimens were defoliated and tested with the drag being reduced from 1/10 to 1/5 of the whole crown drag values.

4.4 Addenda

Data furnished by Lemon (1960), in response to the author's request, show relationships for three species of crops — corn, alfalfa, and wheat — of the wind speed and the roughness parameter z_0.

For winds ranging from 200 to 1000 cm/sec measured above the crop, the z_0-values vary as follows:

Alfalfa (75 cm) z_0 decreases continuously —

Wheat (130 cm) z_0 rises, then falls off rapidly —

Corn (240 cm) z_0 increases continuously —

— all as the wind speed increases. The displacement height d varies inversely as the z_0 value.

The curves are suggestive that for winds greater than those shown for the corn, this crop would probably show a reversal. This is possible since the dynamic pressure of greater wind will tend to bend the drop over to a more streamlined shape. Some opinions have been expressed that crops such as corn with long flexible leaves that flap probably would have greater drag coefficients under higher wind speeds, up to the point that physical damage to the plant might occur. Lemon's data do not cover this range but do show the increased z_0 which evidences the greater drag at higher velocities.

It is interesting to note that this information supports some of the contentions outlined previously in this report. On the basis of these relationships it would be appropriate to conclude that for long stemmed and flexible bladed crops and vegetation z_0 does increase with wind. That alfalfa is reversed follows logically since it is a small leafed plant. A similar relationship undoubtedly exists in the several arrangements of leaves, needles, branches, etc., in trees. The botanical structure of tree leaves and needles, etc., should be investigated in the light of these concepts regarding velocity-drag relationships. Sauer (1951) and Lai (1955) tend to lead toward this in analyzing the individual species which they studied.

References

Hirata, T.: Fundamental Studies on the Formation of Cutting Series (II), on the Centre Pressure, the Drag Coefficient of a Tree and

One Effect of Shelter Belts. Bull. Tokyo University for. No. 39, 1951 (1-11) No. 45, 1953 (61-87). Japanese.

Hoerner, S.: Fluid Dynamic Drag. Published by author, 148 Bustead Drive, Midland Park, N.J. 1958 (260 pp.)

Hoerner, S.: Aerodynamic Drag. Published by author, 148 Bustead Drive, Midland Park, N.J. 1951.

Lai, W.: Aerodynamic Crown Drag of Several Broadleaf Tree Species, Interim Technical Report. AFSWP, 63, 1955 USDA, FS

Lemon, E.R.: Private communication on micrometeorological research, Sections from Ann. Report, 1960, USDA, ARS, SWCRD, NE Br., Cornell University, Ithaca, New York.

Sauer, F.M., W.L. Fons and K. Arnold: Experimental Investigation of Aerodynamic Drag in Tree Crowns Exposed to Steady Wind — Conifers. Division of For. Fire Res., USDA, For. Ser., Washington, D.C., 1951.

Storey, T.G., W.L. Fons and F.M. Sauer: Crown Characteristics of Several Conifer Tree Species, Interim Technical Report — AFSWP 416, Division of For. Fire Res., USDA, For. Ser., Washington, D.C., 1955.

Storey, T.G., and W.Y. Pong: Crown Characteristics of Several Hardwood Tree Species, Interim Technical Report AFSWP 968, Division of For. Fire Res., USDA, For. Ser., Washington, D.C., 1957.

Scanner's note:

This page is blank.

5

Regional and Meridional Distributions of Continental Vegetation Cover and Aerodynamic Roughness Parameters

Ernest C. Kung and Heinz H. Lettau

Department of Meteorology
University of Wisconsin

Abstract. Data on the areal distribution of defined types of plant cover are evaluated for the region of the State of Wisconsin, and for latitudinal zones of all continents. An empirical numerical relationship between plant height and aerodynamic roughness parameter (z_0) is used to estimate weighted area-averages of log z_0. In an attempt to establish a basis for utilizing micrometeorological information in large-scale meteorological problems, the regional and meridional distributions, and their seasonal variations, of vegetative surface roughness is discussed.

5.1 Introduction

Frictional forces in the lower atmosphere, and the dissipation of mechanical energy of large-to-small-scale air currents depend primarily on the roughness structure of the natural ground. Micrometeorological information indicates that the frictional effects at the lower boundary can be expressed in terms of the aerodynamic roughness parameter (z_0, cm), which depends significantly on the type of vegetation cover. In a preceding report (9) a numerical relationship between the roughness parameter and the plant height was extended to include several types of tall vegetation. In order to obtain the roughness parameter for a region, in contrast to that of a defined micrometeorological site, it is necessary to combine the above relationship with data on the horizontal distribution of plant covers.

In the present paper, an attempt is made to study in detail the probable seasonal variation of aerodynamic roughness for a region of

approximately 10^5 km^2 as represented by the State of Wisconsin. Also, available ecological information for all continents is used to prepare the basis of a world-wide study of the meridional distribution of roughness parameters for all land surfaces.

5.2 Method and Data

The evaluation of the aerodynamic roughness of a selected region involves the following four steps:

(1) Classify the vegetation into major types and determine the area-percentage of each type (i. e., the "land use").

(2) Estimate representative heights for each vegetation type with a breakdown by month, or by season.

(3) On the basis of (2) assign roughness parameters to each vegetation type.

(4) Compute the regional mean of the logarithm of roughness parameters, employing the percentage area of each vegetation type as a weight factor, with a breakdown by month, or by season.

For the regional study of the State of Wisconsin, the data on land use were obtained from the following sources: statistics by the Wisconsin Crop and Livestock Reporting Service (20) and the Conservation Department (10, 19), and estimates by the staff of the Forestry Extension Service of the University of Wisconsin (8). For the continent-wide study the statistics of the United Nations (6) and other sources (2, 5, 7, 11, 13, 14, 15, 16, 17) were used.

Phenological data and estimates of plant heights were obtained from various sources (1, 3, 12, 18), and also as the result of discussions with staff members of the Departments of Agronomy and Botany at the University of Wisconsin. For the estimate of roughness parameters, on the basis of plant height, the numerical relationship derived by E. Kung (9) was used.

5.3 Monthly Data on Surface Roughness for the Region of Wisconsin

The area of the State of Wisconsin was divided into nine districts on a county basis, in the following manner.

District	Counties Included
1. Northwest	Barron, Bayfield, Burnett, Chippewa, Douglas, Polk, Rusk, Sawyer, Washburn
2. North	Ashland, Clark, Iron, Lincoln, Marathon, Oneida, Price, Taylor, Vilas
3. Northeast	Florence, Forest, Langlade, Marinette, Oconto, Shawano
4. West	Buffalo, Dunn, Eau Claire, Jackson, La Crosse, Monroe, Pepin, Pierce, St. Croix, Trempealeau
5. Central	Adams, Green Lake, Juneau, Marquette, Portage, Waupaca, Waushara, Wood
6. East	Brown, Calumet, Door, Fond du Lac, Kewaunee, Manitowoc, Outagamie, Sheboygan, Winnebago
7. Southwest	Crawford, Grant, Iowa, Lafayette, Richland, Sauk, Vernon
8. South	Columbia, Dane, Dodge, Green, Jefferson, Rock
9. Southeast	Kenosha, Milwaukee, Ozaukee, Racine, Walworth, Washington, Waukesha.

According to land use in these districts nine major categories of vegetation cover were distinguished. Each category involves either one, or more than two main kinds of vegetation, as follows: (1) Corn - (2) Oats - (3) Hay - (4) Other field crops - (5) Natural vegetations - (6) Oak - (7) Maple - (8) Aspen - (9) Other trees. The results of the vegetation survey for each district are shown in Table 1, in percentages of total district area.

Combining the vegetation cover survey, phenological data and estimates of vegetation height, the average monthly roughness parameter was evaluated for each district of Wisconsin. Results are shown

Table 1. Percentage area covered with indicated vegetation types for nine districts of the State of Wisconsin.

Vegetation Type	Districts 1-NW	2-N	3-NE	4-W	5-C	6-E	7-SW	8-S	9-SE
Corn	3.23	1.66	2.32	9.14	7.37	10.16	12.40	20.76	16.39
Oats	3.78	3.86	3.81	10.85	7.00	19.05	9.63	15.91	14.84
Hay	7.91	7.59	6.61	13.15	11.09	19.61	15.37	13.85	14.41
Grains	0.11	0.13	0.14	0.60	1.23	1.95	0.25	1.00	2.05
Field crops other than grains	0.22	0.34	0.46	1.21	0.79	1.43	0.61	1.84	1.48
Idle and noncropped land	3.94	3.39	3.90	6.99	10.80	7.94	5.75	7.75	7.42
Pastured woodland	13.47	11.14	10.28	16.78	13.13	7.72	21.90	7.04	8.35
Other pastured land	4.66	6.30	2.60	8.03	6.85	4.79	15.67	9.77	5.64
Oak	8.66	9.07	17.47	19.81	10.43	6.84	12.28	14.73	19.62
Maple	7.34	7.68	9.61	2.12	5.74	3.76	1.29	1.55	2.06
Aspen	33.35	34.90	26.20	2.83	15.65	10.25	0.65	0.78	1.03
Other trees	13.34	13.96	16.60	8.49	9.91	6.49	4.20	5.04	6.71
Total Area (10^3 km^2)	24.47	25.16	15.61	17.89	13.69	11.83	13.95	12.27	6.81

in Table 2. For this evaluation a roughness parameter for snow cover of $z_0 = 0.10$ cm was adopted from Deacon's study (4).

The distribution of average roughness parameters over different districts and their seasonal change can be summarized as follows. The northern parts of the state have high annual z_0-averages — $z_0 = 64.96$ cm in Northeast, 44.62 cm in North, and 38.85 cm in Northwest. The z_0-values decrease towards the Southwest and South. The annual average z_0-values are $z_0 = 8.12$ cm in West, 12.71 cm in Central, 5.24 in East, 3.19 in Southwest, 4.29 in South and 6.82 cm in Southeast. The regional difference of characteristic roughness parameter is mainly due to heavy acreage of forest trees in the northern parts of the state, while in the southern parts of the state farm crops and grass-type natural vegetation dominate. The West and Central districts are a zone of transition. Since the z_0-value is proportional to the 1.19th power of the vegetation height, these characteristic differences in vegetation cover are emphasized. The seasonal change of roughness parameters is also significant for the whole state as well as each district. This is due to the phenological cycle. The lush summer vegetation produces the highest z_0-values. The spring and fall values are intermediate between the summer maximum and winter minimum. We also notice that the seasonal change of roughness parameter is greater in the southern and central part of the state than in the northern parts. This is illustrated by the following ratio of winter to July z_0 values:

Districts	Winter z_0 / July z_0 (%)
Northwest	20.7
North	24.7
Northeast	27.6
West	5.6
Central	8.0
East	3.7
Southwest	3.4
South	2.9
Southeast	4.0
State Average	9.6

This is caused by the withering of field crops and grass-type vegetations, with snow cover over these low vegetation areas in southern

Table 2. Seasonal trend of estimated area-averages of the aerodynamic roughness parameter (z_0, cm) for nine districts of the State of Wisconsin.

Month	Districts 1-NW	2-N	3-NE	4-W	5-C	6-E	7-SW	8-S	9-SE	State Average
December-March	16.63	21.11	32.75	1.70	3.20	0.96	0.48	0.66	1.24	4.44
April	34.62	40.31	59.13	7.57	11.28	4.85	3.06	3.54	5.86	14.07
May	35.66	42.05	61.22	9.76	13.65	7.48	4.58	6.39	10.19	17.54
June	70.71	79.23	106.20	24.33	32.70	21.00	11.52	16.24	22.96	38.58
July	80.11	85.39	118.80	30.44	40.21	25.74	14.09	22.92	31.27	46.06
August	79.62	81.25	112.80	25.68	36.46	19.71	13.37	18.46	26.43	41.64
September	70.94	74.93	104.70	21.83	31.64	13.37	10.21	13.43	18.54	34.77
October	66.18	70.23	99.88	19.78	29.62	11.34	9.29	11.84	16.85	31.90
November	59.03	63.97	90.86	15.45	24.32	8.48	6.99	8.14	12.06	26.17
Annual Mean	38.85	44.62	64.96	8.12	12.71	5.24	3.19	4.29	6.82	15.59

NOTE: State averages and annual means are the antilogarithm of the averaged logarithms of the individual z_0-values.

and central parts of the state. The effect of snow cover is much reduced in the forested northern parts of the state.

5.4 Meridional Distribution of Vegetive Roughness

The land area of the world was studied separately for: (1) the Americas, (2) Europe-Africa, and (3) Asia-Oceania (including the USSR), with a subdivision into 10-degree latitudinal zones, and 5-degree latitudinal zones between 30 and 50°N in North America. The estimates of the aerodynamic roughness parameter of all zones, for the seasons, were based on surveys of the land use and the distribution of vegetation cover.

For the United States and Canada the main sources of information were the USDA Official Statistics (15, 16) and the Canada Yearbook (5). The data for China, India, and Australia were taken from Shen (13), Time of India (14), and the Yearbook of the Commonwealth of Australia (2), respectively, together with a survey of existing maps (7, 17). The 1957 FAO Yearbook (6) was used for all other areas. Atlasses (7, 17) and other miscellaneous information (1, 8, 16, etc.) were also considered for bridging gaps, and to make slight adjustments in a few cases where the available statistics data were insufficient or incomplete.

The following eight classes of continental vegetation cover were distinguished: (1) Crops - (2) Woodland and tree crops - (3) Meadow and pasture - (4) Forest - (5) Natural vegetations - (6) Tundra - (7) Desert -, and (8) Built-on and waste land. The results of the survey are shown in Tables 3a and 3b in percentages of the total zonal area, separately for the three major land masses.

The roughness parameters for each season and all continental zones were computed in the same manner as the regional values for the State of Wisconsin. Values of $z_0 = 0.03$ cm for deserts, and $z_0 = 0.1$ for snow cover were adopted from the study of Deacon (4). The results are listed in Tables 4a and 4b, and illustrated in Figures 1, 2, and 3.

The latitudinal distributions reflect the characteristic vegetation covers over the continents. In general, the z_0-values are relatively large for both the equatorial zone and temperate to high latitudes; they show minimum values about 20 to 30 degrees from the equator. This is caused by the meridional sequence ranging from tropical forests, to low natural vegetations and crops, then to the woodlands and coniferous forests of the temperate zone. Farther north the z_0-values

Table 3a. Vegetation cover in percent of total zonal area — (1) Crops, (2) Woodland and tree crops, (3) Meadow and pasture, (4) Forest, (5a) Natural vegetation, (5b) Natural vegetation of generally low types if distinct from 5a, (6) Tundra, (7) Desert, (8) Built-on and waste land.

The Americas

	(1)	(2)	(3)	(4)	(5a)	(5b)	(6)	(7)	(8)	Total Area $10^4 km^2$
70-60°N	0.0	0.0	15.8	30.5	0.0	0.0	53.7	0.0	0.0	400.2
60-50	7.0	5.8	0.8	63.8	21.1	0.0	1.5	0.0	0.0	498.0
50-45	18.4	1.3	21.9	42.0	14.8	0.0	0.0	0.0	1.6	153.6
45-40	27.7	0.0	34.4	30.2	4.3	0.0	0.0	0.0	3.4	213.6
40-35	20.5	0.0	37.7	33.5	6.9	0.0	0.0	1.3	0.1	236.2
35-30	14.8	0.0	40.7	37.3	3.1	0.0	0.0	4.1	0.0	202.9
30-20	10.0	0.0	31.9	23.2	4.6	0.0	0.0	0.0	30.3	208.0
20-10	11.3	0.0	11.1	47.2	7.6	0.0	0.0	0.0	22.8	56.0
10-Equ.	3.8	0.0	12.3	50.1	1.7	0.0	0.0	0.0	32.1	257.4
Equ.-10°S	1.6	0.0	6.4	79.3	8.7	0.0	0.0	3.7	0.3	540.9
10-20	2.0	0.0	20.2	33.3	28.5	0.0	0.0	4.8	11.2	434.9
20-30	2.8	0.0	11.7	48.0	14.4	6.5	0.0	4.4	12.2	291.7
30-40	22.9	0.0	34.9	16.4	13.1	1.3	0.0	0.0	11.4	164.9
40-50	0.0	0.0	56.3	30.0	10.0	0.0	0.0	0.0	2.8	70.7
50-55	0.0	0.0	24.9	69.8	5.3	0.0	0.0	0.0	0.0	22.8

Table 3b. Vegetation cover in percent of total zonal area — (1) Crops, (2) Woodland and tree crops, (3) Meadow and pasture, (4) Forest, (5a) Natural vegetation, (5b) Natural vegetation of generally low types if distinct from 5a, (6) Tundra, (7) Desert, (8) Built-on and waste land.

Europe-Africa	(1)	(2)	(3)	(4)	(5a)	(5b)	(6)	(7)	(8)	Total Area $10^4 km^2$
70-60°N	5.9	0.0	2.7	42.6	0.0	0.0	48.8	0.0	0.0	121.4
60-50	40.4	0.0	27.0	19.1	0.0	0.0	0.0	0.0	13.5	108.0
50-40	40.1	0.0	20.1	25.7	3.7	0.0	0.0	0.0	10.4	183.2
40-30	22.9	0.0	16.4	12.6	6.7	9.6	0.0	31.8	0.0	211.6
30-20	0.7	0.0	5.0	0.0	0.1	0.0	0.0	94.2	0.0	440.9
20-10	2.2	0.0	10.8	26.5	2.2	6.8	0.0	51.5	0.0	802.3
10-Equ.	14.2	0.0	18.8	37.5	10.8	8.4	0.0	10.3	0.0	619.9
Equ.-10°S	15.4	8.4	1.2	40.8	34.2	0.0	0.0	0.0	0.0	333.9
10-20	10.1	1.6	29.8	40.9	17.6	0.0	0.0	0.0	0.0	387.1
20-35	3.2	0.0	65.4	2.5	13.5	15.4	0.0	0.0	0.0	276.0
Asia-Oceania (including USSR)										
70-60°N	5.3	0.0	0.0	52.8	0.0	0.0	41.9	0.0	0.0	716.4
60-50	26.9	0.0	18.9	34.2	20.0	0.0	0.0	0.0	0.0	848.7
50-40	13.2	0.0	29.4	13.9	7.8	0.0	0.0	35.7	0.0	1008.2
40-30	15.1	0.0	16.7	8.8	6.3	18.0	0.0	35.1	0.0	852.2
30-20	23.5	0.0	12.1	11.7	4.9	33.9	0.0	13.9	0.0	765.2
20-10	23.4	0.0	7.1	35.0	8.6	18.3	0.0	7.6	0.0	285.0
10-Equ.	16.6	0.0	0.4	72.6	2.1	7.5	0.0	0.0	0.8	40.1
Equ.-10°S	8.5	0.0	0.0	49.4	42.0	0.0	0.0	0.0	0.1	209.7
10-20	50.8	2.2	36.6	0.0	0.0	0.0	0.0	10.4	0.0	145.9
20-30	0.0	29.9	26.7	13.3	0.0	0.0	0.0	30.1	0.0	419.1
30-40	8.7	2.7	52.7	32.6	0.0	0.0	0.0	3.3	0.0	200.3
40-50	2.4	35.4	37.5	9.9	1.2	13.6	0.0	0.0	0.0	33.6

Table 4a. Estimated zonal averages of the aerodynamic roughness parameter (z_0, cm) for the seasons.

The Americas	Spring	Summer	Fall	Winter
70-60°N	1.92	8.68	2.07	1.36
60-50	41.70	141.3	86.74	35.28
50-45	17.86	54.06	24.97	4.00
45-40	9.08	31.46	19.90	1.28
40-35	16.30	32.92	19.84	13.13
35-30	28.29	35.56	28.86	20.92
30-20	15.25	16.75	14.64	12.28
20-10	45.67	48.87	41.97	48.19
10-Equ.	77.45	79.20	75.32	78.85
Equ. -10°S	418.9	431.3	416.2	421.6
10-20	44.85	45.08	44.37	45.15
20-30	44.03	44.51	43.57	44.59
30-40	13.80	10.91	15.30	17.71
40-50	24.84	15.53	22.71	28.80
50-55	126.0	105.4	116.9	133.1

Table 4b. Estimated zonal averages of the aerodynamic roughness parameter (z_0, cm) for the seasons.

Europe-Africa	Spring	Summer	Fall	Winter
70-60° N	4. 66	16. 65	11. 97	3. 88
60-50	2. 19	18. 49	4. 48	0. 51
50-40	7. 48	26. 24	10. 85	2. 90
40-30	2. 24	2. 78	2. 31	1. 83
30-20	0. 04	0. 04	0. 04	0. 04
20-10	1. 32	1. 34	1. 30	1. 34
10-Equ.	32. 23	35. 09	28. 98	34. 50
Equ. -10° S	126. 1	134. 9	109. 8	135. 1
10-20	59. 50	62. 22	54. 29	64. 40
20-35	9. 32	5. 37	7. 52	9. 46
Asia-Oceania (including USSR)				
70-60° N	10. 55	29. 66	11. 21	9. 26
60-50	5. 02	29. 42	8. 64	1. 87
50-40	0. 67	1. 99	1. 06	0. 21
40-30	1. 00	1. 51	1. 21	0. 78
30-20	4. 08	5. 08	3. 69	3. 43
20-10	37. 60	38. 94	36. 82	38. 15
10-Equ.	352. 6	361. 5	347. 4	356. 2
Equ. -10° S	187. 2	193. 2	188. 3	194. 0
10-20	143. 5	100. 0	103. 5	145. 9
20-30	23. 66	10. 37	10. 68	10. 94
30-40	22. 27	18. 93	19. 41	24. 62
40-50	47. 59	35. 92	43. 33	52. 61

FIGURE 1 — ROUGHNESS PARAMETER RELATED TO VEGETATION HEIGHT

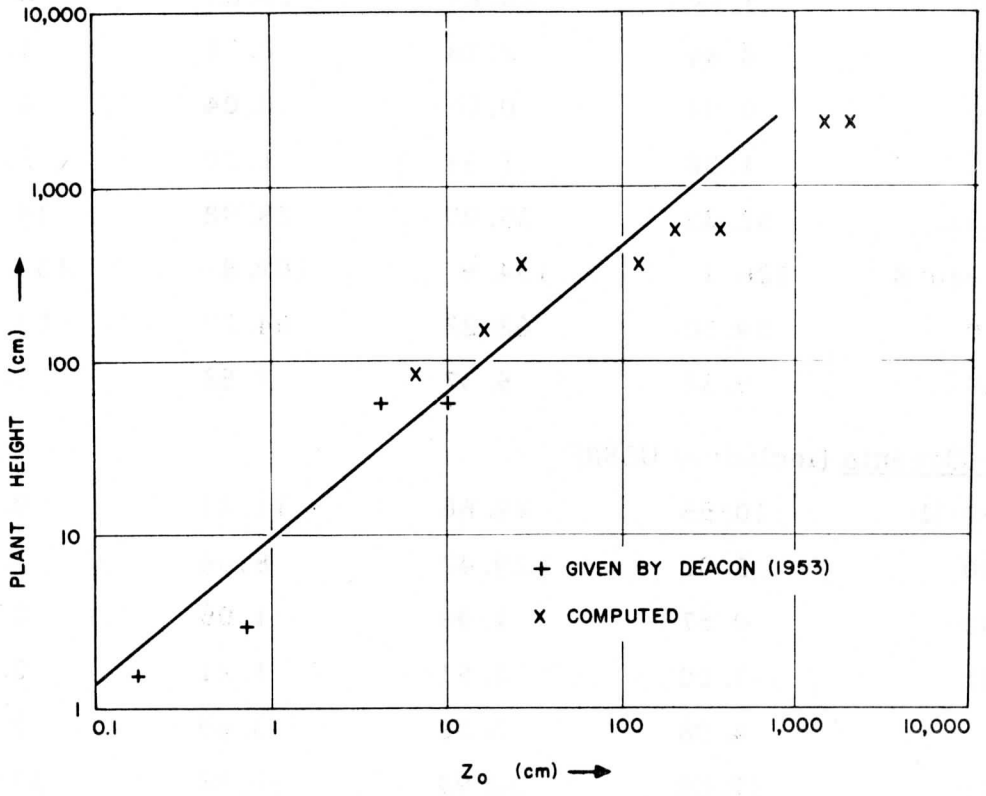

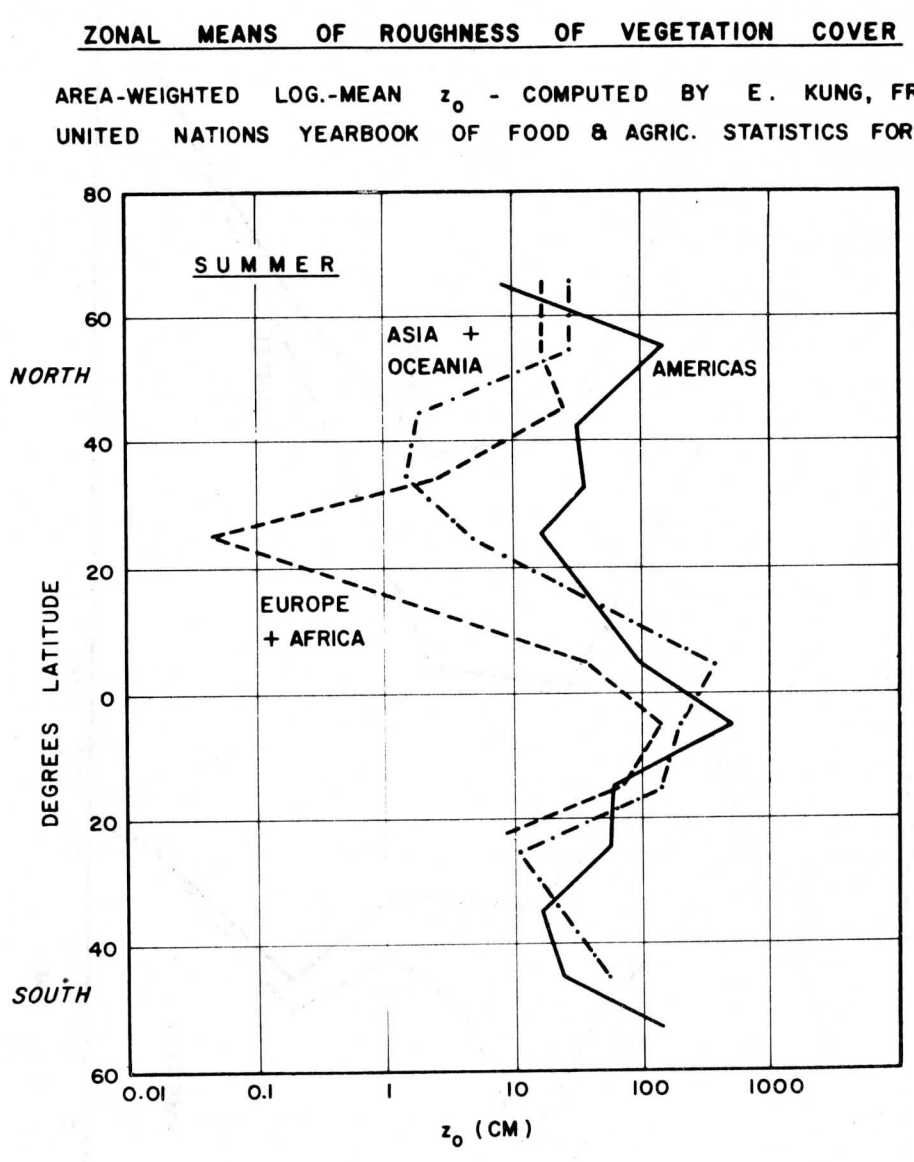

Fig. 2. Meridional profiles of the average aerodynamic roughness parameter derived from vegetation cover on the continents in summer.

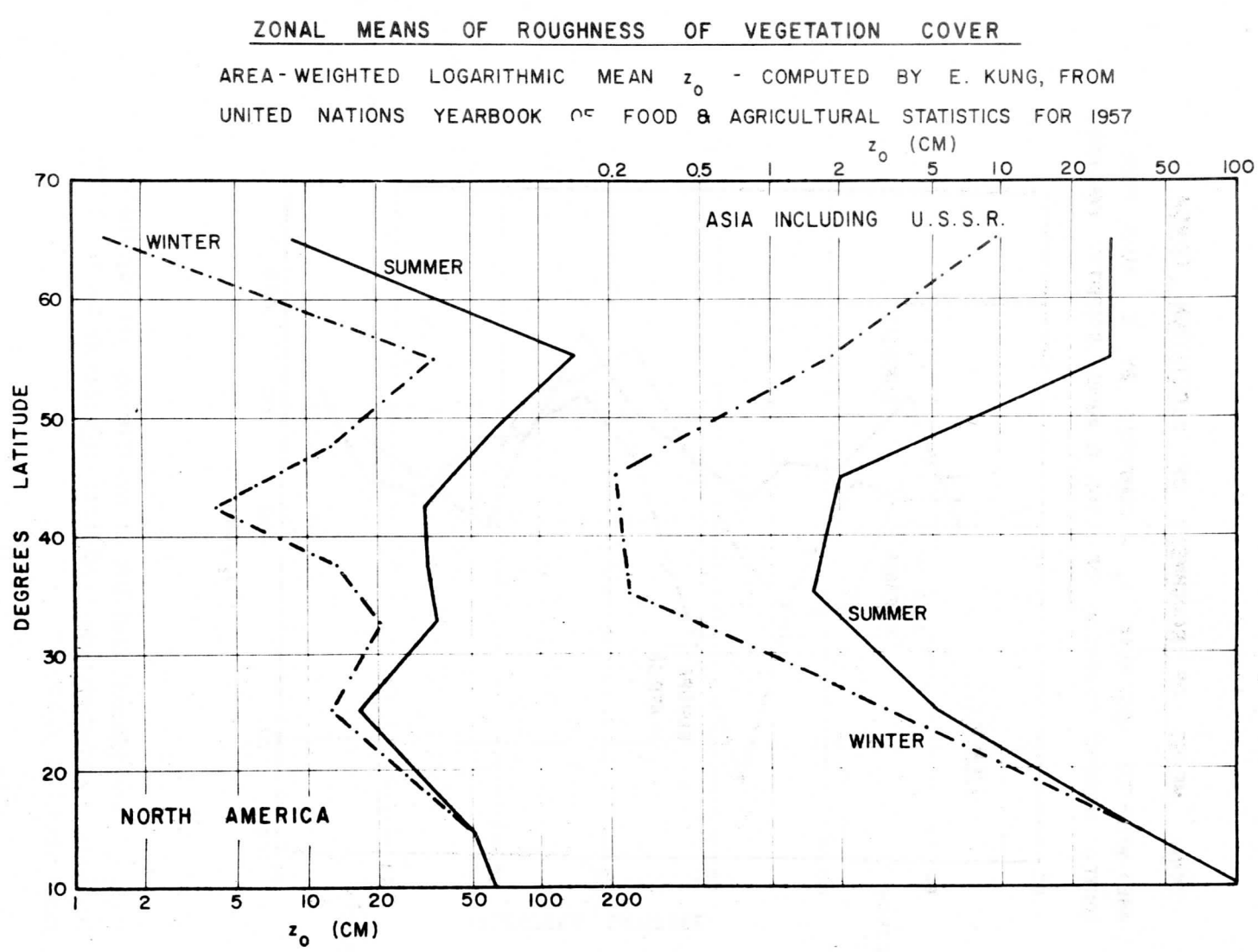

Fig. 3. Meridional profiles of the average aerodynamic roughness parameter as derived from vegetation cover on northern hemispheric continent areas in summer and winter.

decrease again, especially in North America, due to lower vegetation and extended tundra regions.

In the southern hemisphere, the latitudinal distributions of z_0 are nearly the same for all three continental groups. In the northern hemisphere, there are significant differences. In the low and middle latitudes of Europe and North Africa, extremely small z_0-values are due to extended low-vegetation and desert areas, while lush vegetation in the same latitudes of North America and Asia causes relatively high values. At highest latitudes of Europe and Asia the roughness parameter is significantly larger than in North America owing to the differences in northern extent of coniferous and other forests.

The seasonal trends of zonal roughness parameters reflect the phenological cycle. There is little change in tropical regions. Crop growth and phenological sequences of vegetation height in middle and high latitudes cause roughness maxima in summer and minima in winter. It can be noted that the autumn-wilting of low-type vegetations, and winter snow covering them, affects significantly the seasonal changes in roughness parameter.

5.5 Discussion, and Concluding Remarks

The evaluation of regional and zonal roughness parameters is based on several assumptions, and the results must be considered tentative and restricted. In the survey of land use and vegetation cover, a great number of different sources were employed. Since the statistical data were frequently found incomplete, certain adjustments had to be made. Extrapolations, supported by economical maps, were necessary, especially for Australia, South America, and the USSR.

Vegetation height was considered the major factor in causing aerodynamical roughness. The forests, therefore, play an important role. It must be expected that the density of forest trees is an additional factor. Due to the lack of pertinent information this factor could not be considered here. The problem can be solved only by detailed experimental investigations in relatively small areas. Similar restrictions are imposed by the adoption of Deacon's z_0 values over desert and snow. However, it is believed that only relatively minor revisions of the zonal distribution of aerodynamic roughness parameters will be necessary.

The method of computing the representative area-means of roughness parameters as the weighted average of ($\log z_0$)-values is suggested by Lettau's (21) findings that the logarithm of the surface-

Rossby number (which is proportional to $1/z_0$) determines the drag coefficient of large-scale atmospheric currents. The meteorological and climatological significance of the estimates of regional and zonal roughness parameters can only be tested by a comparison of actual, with computed friction effects in the lower atmosphere. A relatively direct and readily available climatological measure of actual friction effects is the mean ratio of observed wind speed (at anemometer level of a synoptic or climatological station) to regional geostrophic speed; reference is made to Lettau (21). A continent-wide study of this ratio, together with an evaluation of vegetive roughness parameters and subsequent drag coefficients, is in progress. The investigation will include a study of the combined effects of plant cover and topography on the aerodynamic roughness of continent surfaces.

References

1. Balchin, W. G. V.: Geography and Man. New Era Publication Company, London, 1955.

2. Commonwealth Bureau of Census and Statistics: Yearbook of the Commonwealth of Australia, No. 46, 1960. Canberra.

3. Curtis, J. T.: The Vegetation of Wisconsin. University of Wisconsin Press, Madison, 1959.

4. Deacon, E. L.: Vertical Profiles of Mean Wind in the Surface Layer of the Atmosphere. Geophysical Memoirs, No. 91, 1953.

5. Dominion Bureau of Statistics: Canada Yearbook 1957-1958. Ottawa, 1958.

6. Food and Agriculture Organization of the United Nations: Yearbook of Food and Agricultural Statistics, 1956. Rome, 1958.

7. Hammond, C. S. and Co.: Hammond's Comparative World Atlas. New York.

8. Kung, E. C.: Ecological data of crops and natural vegetations. (Data collected at the University of Wisconsin by personal communication.)

9. Kung, E. C.: See Section 3 of this Annual Report.

10. Mackie, D. J., and H. W. Thorne: Wisconsin Forest Resources.

Wisconsin Conservation Department and Wisconsin Forestry Advisory Committee, 1957.

11. Oxford Regional Economic Atlas: The USSR and Eastern Europe. Oxford University Press, 1956.

12. Packard, R. L.: Ecological Geography of Certain Wisconsin Feed Crops. Ph. D. thesis, University of Wisconsin, 1957.

13. Shen, T. H.: Agricultural Resources of China. Cornell University Press, Ithaca, 1951.

14. The Time of India: Directory and Yearbook, 1956-1960. Coleman Company Ltd., Bennett.

15. United States Department of Agriculture: Agricultural Statistics, 1957. Washington, D. C., 1958.

16. United States Department of Agriculture: Forest Timber Resources for America's Future. Washington, D. C., 1958.

17. Van Royen, W.: The Agricultural Resources of the World. Prentice-Hall, Inc., New York, 1954.

18. Wilson, F. G.: Forest Trees of Wisconsin. Wisconsin Conservation Department Publication, 507-55, 1955.

19. Wisconsin Conservation Department: Twenty-sixth Biennial Report. Wisconsin Conservation Department Publication, 612-59, 1959.

20. Wisconsin Crop and Livestock Reporting Service: Wisconsin Agriculture in Mid-Century. Bulletin No. 325, 1954.

21. Lettau, H. H.: Wind profile, surface stress and geostrophic drag coefficients in the atmospheric surface layer. In Atmospheric Diffusion and Air Pollution (F. N. Frenkiel and P. S. Sheppard, editors). Vol. 6 of "Advances in Geophysics," Academic Press, New York and London, 1959.

Scanner's note:

This page is blank.

6

A Method for Machine Computation of Wind Profile Parameters

Stephen M. Robinson

Numerical Analysis Laboratory
and
Department of Soils
University of Wisconsin

Abstract. A least-square method is described by which the three parameters of the wind profile in the adiabatic surface layer of the atmosphere can be determined with the aid of electronic digital computers.

6.1 Introduction

Under adiabatic conditions, the wind profile in the atmospheric surface layer is determined by three parameters, which are the roughness length, the zero point displacement, and the surface stress. When reference is made to Lettau [1], the three parameters are related by the following equation:

$$V = k^{-1}(\tau_0 / \rho)^{\frac{1}{2}} \ln [(z + d + z_0)/z_0] \qquad (1)$$

where

k = Kármán number = 0.38

τ_0 = surface stress (dyne/cm^2)

ρ = air density (g/cm^3)

z = nominal height of anemometer (cm)

d = zero point displacement (cm)

z_0 = roughness length (cm)

V = mean wind speed (cm/sec) at height z.

Let $V^* = k^{-1}(\tau_0/\rho)^{\frac{1}{2}}$ = friction velocity, (cm/sec^{-1}),

$D = d + z_0$, (cm) ;

then, equation (1) can be rewritten as:

$$V = V^* \ln [(z + D)/z_0] \quad . \tag{2}$$

Given at least three observations of V and z, we wish to solve (2) for V^*, D, and z_0. We therefore subscript the observed variables V and z, and seek a least-squares solution to

$$V_i = V^* \ln [(z_i + D)/z_0] , \quad 1 \leq i \leq N , \tag{3}$$

where N denotes the number of observation levels. The least-squares method requires that

$$\sum_{i=1}^{N} \varepsilon_i^2 \equiv \sum_{i=1}^{N} \{V_i - V^* \ln [(z_i + D)/z_0]\}^2$$

be minimized.

6.2 Analytical Development

The derivation to follow will be greatly simplified if we use vector notation. A vector will be simply an ordered array of N elements; considerations of magnitude and direction will not enter directly. Vector quantities will be distinguished by a bar (e. g., $\overline{V}$, $\overline{F}$, $\overline{G}$), and their scalar product will be indicated by a dot:

$$\overline{F} \cdot \overline{G} \equiv \sum_{i=1}^{N} (F_i G_i) ,$$

where F_i and G_i are arbitrarily defined arrays of N elements each.

Let

$$\overline{W} = \{\ln z_0 , \ln z_0 , \ldots , \ln z_0\} ,$$
$$\overline{X} = \{\ln (z_1 + D), \ln (z_2 + D), \ldots , \ln (z_N + D)\} ,$$
$$\overline{V} = \{V_1, V_2, \ldots , V_N\} ,$$
$$\overline{B} = \{(z_1 + D)^{-1}, (z_2 + D)^{-1}, \ldots , (z_N + D)^{-1}\} ,$$
$$\overline{I} = \{1, 1, \ldots , 1\} .$$

Then (3) becomes

$$\overline{V} = V^*(\overline{X} - \overline{W}) , \tag{4}$$

and the vector of the ε_i values is

$$\bar{\varepsilon} = \bar{V} - V^*(\bar{X} - \bar{W}) \quad . \tag{5}$$

Thus,

$$\sum_{i=1}^{N} \varepsilon_i^2 \equiv \bar{\varepsilon} \cdot \bar{\varepsilon} = \bar{V} \cdot \bar{V} - 2V^* \bar{V} \cdot (\bar{X} - \bar{W}) + V^{*2} (\bar{X} - \bar{W}) \cdot (\bar{X} - \bar{W}). \tag{6}$$

The condition that the quantity (6) be minimized is that the partial derivatives of (6) with respect to V^*, D, and z_0 be zero. Remembering that

$$\frac{\partial \bar{\varepsilon} \cdot \bar{\varepsilon}}{\partial z_0} = \left(\frac{1}{z_0}\right) \frac{\partial \bar{\varepsilon} \cdot \bar{\varepsilon}}{\partial \ln z_0} \quad ,$$

we have

$$\frac{\partial \bar{\varepsilon} \cdot \bar{\varepsilon}}{\partial z_0} = \left(\frac{1}{z_0}\right) [2V^* \bar{V} \cdot \bar{I} - 2V^{*2} (\bar{X} - \bar{W}) \cdot \bar{I}] = 0 \, , \tag{7}$$

or

$$\bar{V} \cdot \bar{I} = V^* (\bar{X} - \bar{W}) \cdot \bar{I} \quad . \tag{8}$$

If we let $\bar{X}_a = N^{-1}\{\bar{X} \cdot \bar{I}, \bar{X} \cdot \bar{I}, \ldots, \bar{X} \cdot \bar{I}\}$, which is the vector of means of the elements of $\bar{X}$, and use a similar convention for $\bar{V}_a$ and $\bar{B}_a$, we may write the vectors of adjusted values of $\bar{V}$, $\bar{X}$, and $\bar{B}$, as

$$\begin{aligned} \bar{v} &= \bar{V} - \bar{V}_a \\ \bar{x} &= \bar{X} - \bar{X}_a \\ \bar{b} &= \bar{B} - \bar{B}_a \quad . \end{aligned} \tag{9}$$

Now, by (8) we have

$$\bar{W} \equiv \bar{W}_a = \bar{X}_a - V^{*^{-1}} \bar{V}_a \quad . \tag{10}$$

Hence, from (5),

$$\bar{\varepsilon} = (\bar{V} - \bar{V}_a) - V^*(\bar{X} - \bar{X}_a) = \bar{v} - V^* \bar{x} \, , \tag{11a}$$

and

$$\bar{\varepsilon} \cdot \bar{\varepsilon} = \bar{v} \cdot \bar{v} - 2V^* \bar{v} \cdot \bar{x} + V^{*2} \bar{x} \cdot \bar{x} \quad . \tag{11b}$$

Since

$$\partial(\bar{\varepsilon} \cdot \bar{\varepsilon})/\partial V^* = 0 \, , \quad V^* = (\bar{v} \cdot \bar{x})/(\bar{x} \cdot \bar{x}) \, , \tag{12}$$

and $$\bar{\varepsilon}\cdot\bar{\varepsilon} = \bar{v}\cdot\bar{v} - (\bar{v}\cdot\bar{x})^2/(\bar{x}\cdot\bar{x}) \ . \qquad (13)$$

Applying the final condition, $\partial(\bar{\varepsilon}\cdot\bar{\varepsilon})/\partial D = 0$, we see that since $\bar{v}\cdot\bar{x}$ should never be zero,

$$g(D) = (\bar{v}\cdot\bar{x})(\bar{x}\cdot\bar{b}) - (\bar{x}\cdot\bar{x})(\bar{v}\cdot\bar{b}) = 0 \ . \qquad (14)$$

The term $g(D)$ in equation (14) is a function of one unknown only which is D. Equation (14) can be attacked by conventional iteration techniques. Perhaps the easiest of these to use — because it requires no derivatives — is the secant method of Jeeves [2]. Given two successive approximations to D, say D_{n-1} and D_n, this method defines

$$D_{n+1} = [D_{n-1}\,g(D_n) - D_n\,g(D_{n-1})]/[g(D_n) - g(D_{n-1})] \ . \qquad (15)$$

The secant method is of convergence order 1.62 . This means that the increase in the number of significant figures at each step is approximately 1.62 times the previous increase. The secant method has been found most effective in practice. The unknown D may be determined to as close a tolerance as one wishes; after doing so, one finds V^* and z_0 by substitution, using equations (10) and (12).

6.3 Sample Computation

Some wind data for an adiabatic surface layer given by Lettau [1, p. 333] have been used to compute a sample set of wind profile parameters. The data are:

i	V_i (cm·sec^{-1})	z_i (cm)
1	837.5	640
2	759.2	320
3	673.7	160
4	585.3	80
5	490.2	40

The computation proceeds as follows: Let us choose two initial guesses for D — say, -20 and -15 cm — and call them D_{-1} and D_0. Then, machine computation resulted in the following sequence:

$$D_1 = -12.684$$

$$D_2 = -10.636$$

$$D_3 = -\ 9.779$$

$$D_4 = -\ 9.554$$

$$D_5 = -\ 9.534$$

$$D_6 = -\ 9.534\ .$$

Thus, within six steps the iteration has converged to a final D-value within a tolerance of 0.001 cm. Upon determining the values of V^* and z_0 from (10) and (12), respectively,

$$D \doteq -9.534 \text{ cm}$$

$$V^* \doteq 115.1 \text{ cm/sec}$$

$$z_0 \doteq 0.433 \text{ cm}.$$

Using hand computation Lettau [1, p. 335] had obtained for the same sample profile $D = -9.5$ cm, and $z_0 = 0.442$ cm.

It should be noted here that the value of z_0, being an exponential function, is very much subject to error. A relatively small variation in D and/or V^* can produce a large variation in z_0. One must therefore be careful when doing the back substitution.

6.4 Windprofile Program

The program (see Appendix) will read in two estimates to D, along with a decimal tolerance $T > 0$, and N pairs of data, each pair consisting of a level z_i and a wind speed V_i. After reading these, the program computes and prints the values of V^*, D, and z_0 necessary to produce a least-squares fit, along with the final error sum of squares (R^2). The program is written in the IBM FORTRAN programming language, and can be compiled and run on any computer able to use that language.

Special features are as follows: (a) If the program encounters a non-positive argument of a logarithm function, or if it attempts to divide by zero, the computer will print:

ERROR AT *TH ITERATION. TRY OTHER INITIAL GUESSES.

The asterisk will be replaced by a number indicating the number of successful iterations made before the error occurred. The next set of data will be read immediately. (b) If sense switch 1 (or its equivalent) is up, the value of D at each iteration will be printed, along with the number of that iteration. This feature is useful for keeping track of the progress of the solution.

The card format (for each set of data) is as follows:

Card 1:	Cols.	1-6	±xx.xx	(the 1st estimate to D, or D_{-1})
		7-12	±xx.xx	(the 2nd estimate to D, or D_0)
		13-20	± .xxxxxx	(the value of the tolerance T)

Cards 2 through (N+1):

Cols.	1-8	+xxx.xxx	(wind speed V_i)
	9-16	+xxx.xxx	(anemometer height z_i)

Card (N+2):

Cols.	1-8	-999.999	(dummy variables for
	9-16	-999.999	control purposes)

To run the program, simply load the compiled deck followed by the data cards. The printing will take place automatically.

Answer format (all answers are in floating-point form):

V^* D z_0 R^2.

References

1. Heinz H. Lettau and Ben Davidson, eds., Exploring the Atmosphere's First Mile, Vol. 1. Pergamon Press, 1957, pp. 332-336.

2. T. A. Jeeves, "Secant Modification of Newton's Method," Comm. of the Assoc. for Computing Machinery, Vol. 1, No. 8 (August 1958), p. 9.

Appendix

```
      PROGRAM WPRF
C       PROGRAM TO FIND WINDPROFILES BY ITERATION
C       1 MARCH 1961          STEPHEN M. ROBINSON
C
      DIMENSION V(50), Z(50)
    3 FORMAT (2F6.2,F8.6)
    4 FORMAT (2F8.3)
    5 FORMAT (I 3, 4E15.6)
    6 FORMAT (10H ERROR AT I4, 39HTH ITERATION. TRY
   6C OTHER INITIAL GUESSES)
    7 FORMAT (E15.6, I3)
      ER=(10.)**(-5)
   20 N=0
      SV=0
      S2V=0
      READ 3, DO, DN, T
      J=0
  150 READ 4, U1, U2
      IF (U1) 10, 11, 11
   11 N=N+1
      Z(N)=U2
      V(N)=U1
      SV=SV+U1
      S2V=S2V+U1**2
      GO TO 150
   10 AN=N
      S=0
      D=DO
   13 SX=0
      S2X=0
      SVX=0
      SB=0
      SVB=0
      SXB=0
      DO 14 I=1,N
      Y=(Z(I)+D)
      IF (Y) 23, 23, 102
   23 PRINT 6, J
      GO TO 20
  102 X=LOGF(Y)
      SX=SX+X
      S2X=S2X+X**2
      SVX=SVX+X*V(I)
```

```
      B=1./Y
      SB=SB+B
      SVB=SVB+B*V(I)
14    SXB=SXB+X*B
      G=(SVX-(SV*SX)/AN)*(SXB-(SX*SB)/AN)-(S2X-
     C(SX**2)/AN)*(SVB-(SV*SB)/AN)
      IF (S) 15, 16, 15
16    S=1.
      G0=G
19    D=DN
      GO TO 13
15    GN=G
      J=J+1
      E1 = (D0*GN-G0*DN)
      E2 = (GN-G0)
22    DP = E1/E2
      IF (ABSF(DP-DN)-T) 17, 17, 18
18    D0 = DN
      G0 = GN
      DN = DP
      IF (SENSE SWITCH 1) 100, 101
100   PRINT 7 DP, J
101   GO TO 19
17    VST = (SVX-(SV*SX)/AN)/(S2X-(SX**2)/AN)
      ZNT=EXPF((SX-(1./VST)*SV)/AN)
      R2=(S2V-(SV**2)/AN)-VST*((2.*SVX-VST*S2X)-
      SX*(2.*SV-VST*SX)/AN)
      PRINT 5, J, VST, DP, ZNT, R2
      GO TO 20
      END
      END
```

7

Investigations of the Modification of Wind Profiles by Artificially Controlled Surface Roughness[1]

John E. Kutzbach

Department of Meteorology
University of Wisconsin

Abstract. A series of controlled wind profile experiments were conducted on the ice of Lake Mendota under conditions of near neutral thermal stratification. The logarithmic model for the variation in wind speed and height is assumed. Changes in the wind profile parameters for controlled variations in the area density (number per unit area) of ordinary bushel baskets are examined. The density of the obstacles ranged from one basket per 48.5 m^2 to one basket per 0.4 m^2. Within this range, the aerodynamic roughness parameter was proportional to basket density raised to the 1.1th power, the zero point displacement was proportional to basket density to the 0.29th power, and the surface stress was proportional to basket density to the 0.49th power. These results are compared with similar experiments conducted in ducts and wind tunnels. The dependence of the geostrophic drag coefficient on the Surface-Rossby Number is discussed.

7.1 Symbols and Definitions

7.1.1 Geometric characteristics of the obstacles and their distribution

h = height of bushel basket, or in general, obstacle height (cm)

$\overline{S}$ = average spacing distance between bushel basket centers (m)

---

[1] Part of this work was submitted to the University of Wisconsin in partial fulfillment of the requirements for the degree of Master of Science.

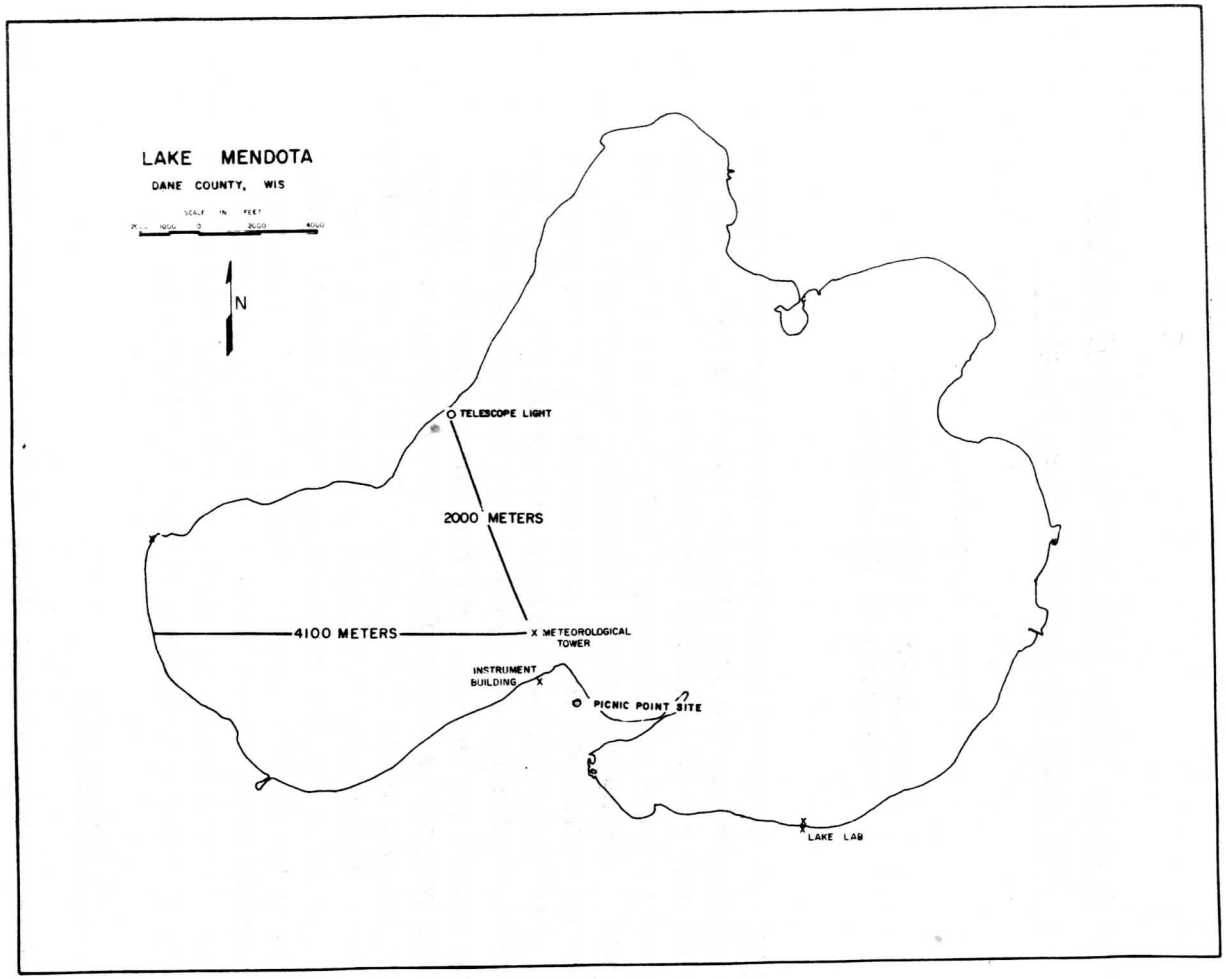

Fig. 1. Lake Mendota, Madison, Wisconsin — showing the location of the Department of Meteorology, University of Wisconsin, micrometeorological tower.

S. A. = specific area of obstacle (m^2) = $(\bar{S})^2$ = reciprocal of area density of obstacles

A = non-dimensional ratio of specific area over the lateral silhouette area of the roughness element

R = upwind roughness fetch (m) = length of upwind trajectory over roughness field

r = downwind roughness fetch (m) = length of downwind (or crosswind) trajectory over roughness field

ϕ = angular width of roughness field (degrees)

x = distance downwind from leading edge of roughness field (m).

7.1.2 Dimensional variables and wind profile parameters

V(z) = mean velocity profile (cm/sec)

V_{con} = mean velocity at control anemometer (cm/sec)

τ_0 = surface stress (dynes/cm^2)

ρ = air density (gm/cm^3)

κ = Kármán constant

$V^* = \kappa^{-1}(\tau_0/\rho)^{\frac{1}{2}}$ = friction velocity (cm/sec)

z = nominal height (cm)

z_0 = aerodynamic roughness parameter (cm)

d = zero point displacement (cm)

7.1.3 Flow parameters and stability parameters

$C = (\tau_0/\rho)^{\frac{1}{2}}/V_{g,o}$ = geostrophic drag coefficient

$\underline{Ro}_0 = V_{g,o}/z_0 f$ = Surface Rossby Number

$\underline{Ri} = (g/T_m)(\partial\theta/\partial z)/(\partial V/\partial z)^2 = g\,\Delta z\,\Delta\theta/T_m(\Delta V)^2$

= Richardson number referred to the geometric mean height $\sqrt{z(z+\Delta z)}$ of two observation levels z and $z + \Delta z$

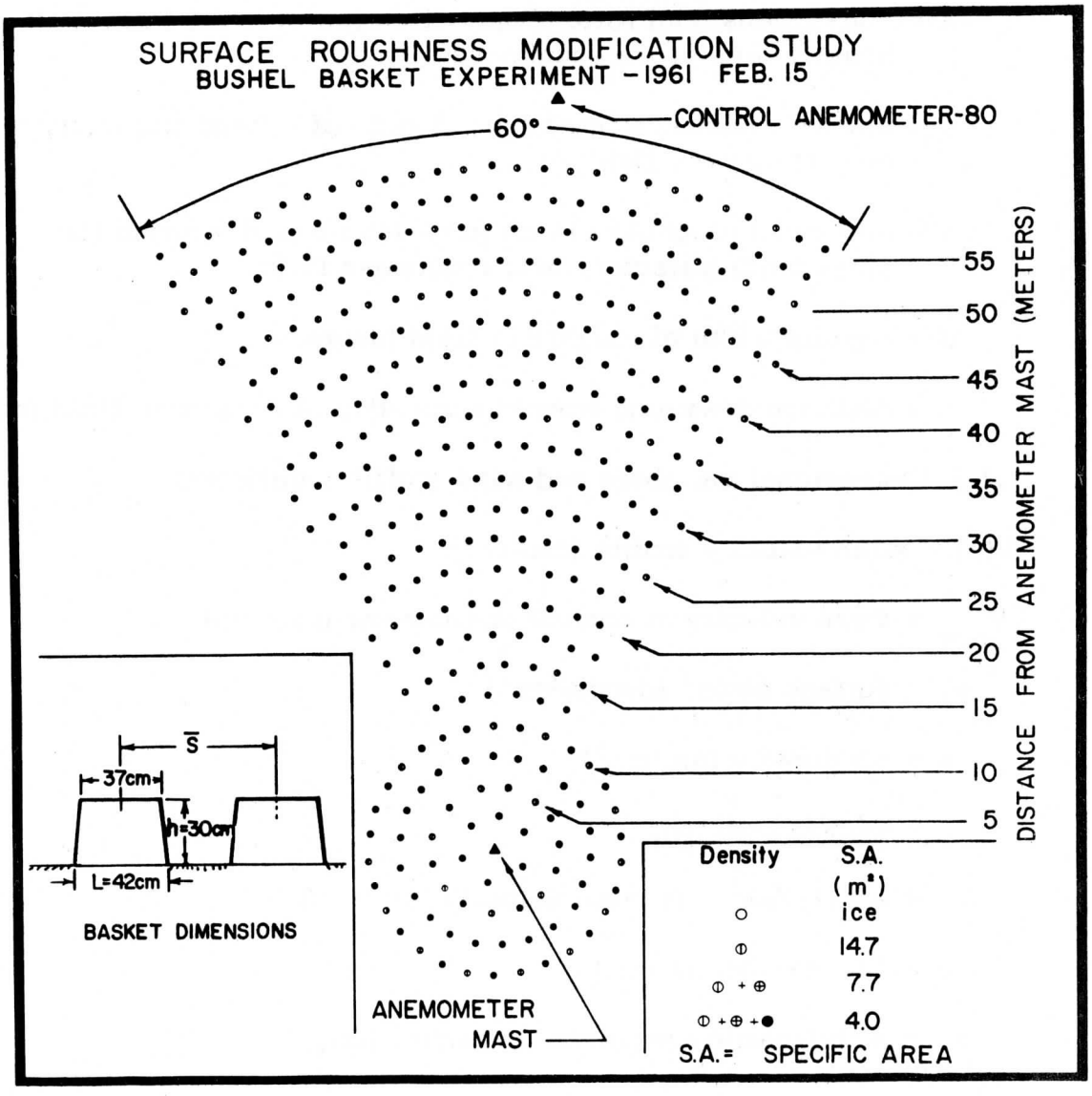

Fig. 2. Schematic illustration of the shape and size of the roughness field, the dimensions of the obstacles, and the sequence of obstacle densities (drawn to scale) of wind profile experiments on the ice of Lake Mendota, 1961.

⊕ — denotes first basket array, S. A. = 14.7 m^2

⊕ + ⊕ — denotes second basket array, S. A. = 7.7 m^2

⊕ + ⊕ + ● — denotes third basket array, S. A. = 4.0 m^2

$(Ri)' = \sum_i \underline{Ri}(z_i) / \sum_i (z_i)$ = bulk stability parameter (1/m)

7.1.4 Additional variables from duct flow

k_s = equivalent height of sand roughness elements (cm)

$N = h/z_0$ (or k_s/z_0) = Nikuradse's roughness ratio

$v^*_r = (\tau_{or}/\rho)^{\frac{1}{2}}$ = shearing velocity at rough wall (cm/sec)

$v^*_g = (\tau_{og}/\rho)^{\frac{1}{2}}$ = shearing velocity at smooth wall (cm/sec)

7.1.5 Additional variables from atmospheric flow

$V_{g,o}$ = geostrophic wind speed at surface (cm/sec)

u = horizontal component of mean velocity (cm/sec)

w = vertical component of mean velocity (cm/sec)

α = direction of surface wind (degrees)

$\alpha_{g,o}$ = direction of geostrophic wind at the surface (degrees)

7.2 Introduction

The functional relationship between the physical and vegetational structure of the earth/air interface and the basic parameters of the low-level wind profile is an important meteorological problem. The pertinent parameters of the problem (roughness length, zero point displacement, and surface stress) have been measured at a variety of micrometeorological sites under diverse atmospheric conditions. This information has limited usefulness for the physical understanding of the processes involved because the configuration of natural roughness elements is usually poorly defined.

Lettau (1959) has outlined the concepts of "passive" and "active" control in micrometeorological field experiments. He defines the terms in the following manner: ". . . passive control. . . means that the field experiment is made over a natural surface which is carefully chosen according to its physical structure, and scheduled at times when the weather conditions are defined and satisfy certain predetermined principles. . . . Active control requires a deliberately planned modification of at least one of the external parameters of physical

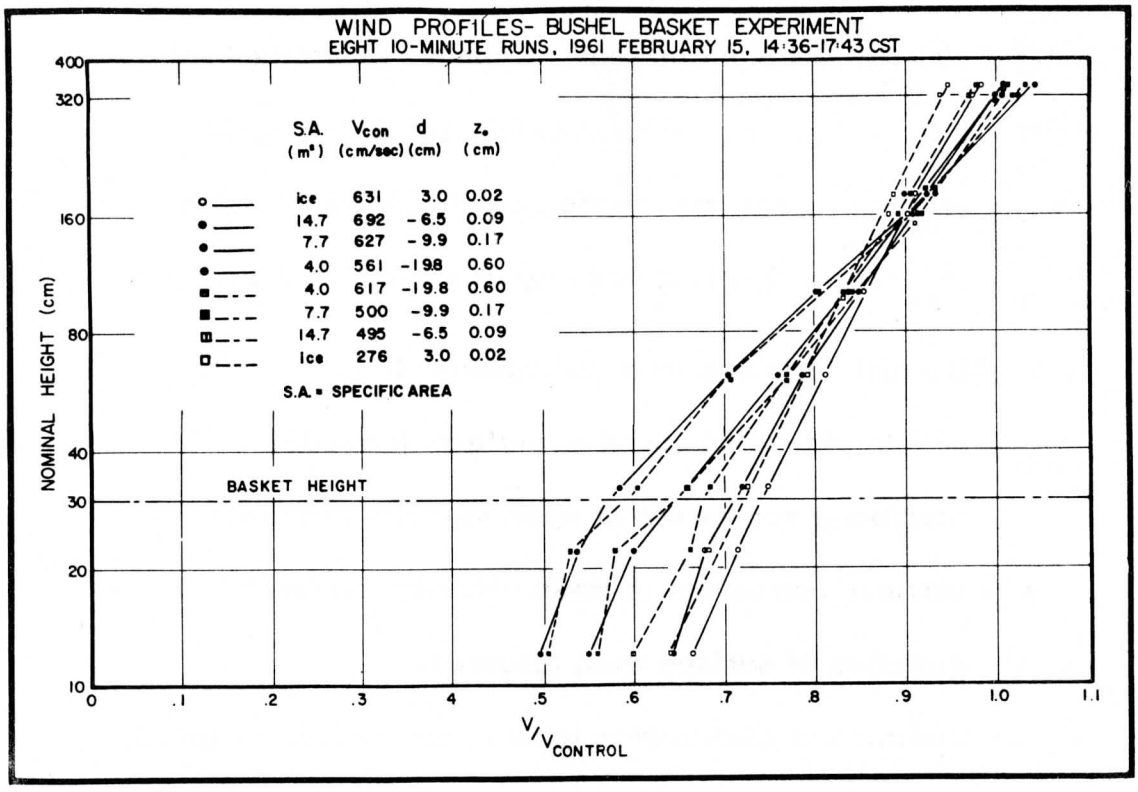

Fig. 3. The 10-minute mean wind profiles associated with the basket distributions of Fig. 2. Solid lines and circles indicate increasing obstacle density — broken lines and squares indicate decreasing obstacle density.

○ — denotes profile over unmodified ice

⊖ — denotes profile over first basket array, S. A. = 14. 7 m^2

⊕ — denotes profile over second basket array, S. A. = 7. 7 m^2

● — denotes profile over third basket array, S. A. = 4. 0 m^2

process in the lower atmosphere." Possibilities of exerting some degree of control on natural processes in the lower atmosphere deserve more attention in meteorological research.

The primary purpose of this paper is to examine changes in the wind profile parameters for controlled variations in the area density (number per unit area) of well-defined roughness elements. The nature of the experiments is discussed in Section 7.3. Section 7.4 deals with the effect of obstacle density (number per unit area) on the wind profile parameters and the dependence of the geostrophic drag coefficient on the Surface Rossby Number.

Some supplementary results are presented in Section 7.5. These include an experimental determination of the Kármán constant, the vertical motion pattern over the roughness field, the variation in wind speed in the air layer between the obstacles, and an estimate of the individual drag coefficient of the obstacle.

Section 7.6 contains an analysis of possible errors and a discussion of data evaluation. Particular attention is given to the growth of the "internal boundary layer" downwind over the roughness field. Conclusions are presented in Section 7.7.

7.3 The Nature of the Experiments

7.3.1 Passive control

The smooth, frozen surface of Lake Mendota at Madison, Wisconsin, is of sufficient extent (approximately 40 km^2 surface area) to allow the establishment of a representative, low-level wind profile. Lettau (1959) has suggested as a "rule of thumb" that the highest instrument level should not exceed 1/50th of the distance from significant discontinuities in the surface structure. The highest anemometer level was 3.4 m above the ice and the upwind fetch over the unobstructed ice was at least 2000 m during all experiments at the micrometeorological site located 400 m off Second Point (see Fig. 1). Therefore, Lettau's suggested criterion for representative profiles is more than satisfied.

Each experiment consisted of a pre-planned sequence of 6 to 10 ten-minute mean wind-profiles extending over a 2- to 3-hour period. Synoptic conditions were chosen such that moderate to strong, steady winds could be expected for several hours,

Ideally, the investigation should be restricted to cases of neutral thermal stratification (adiabatic lapse rate). In practice, it must be

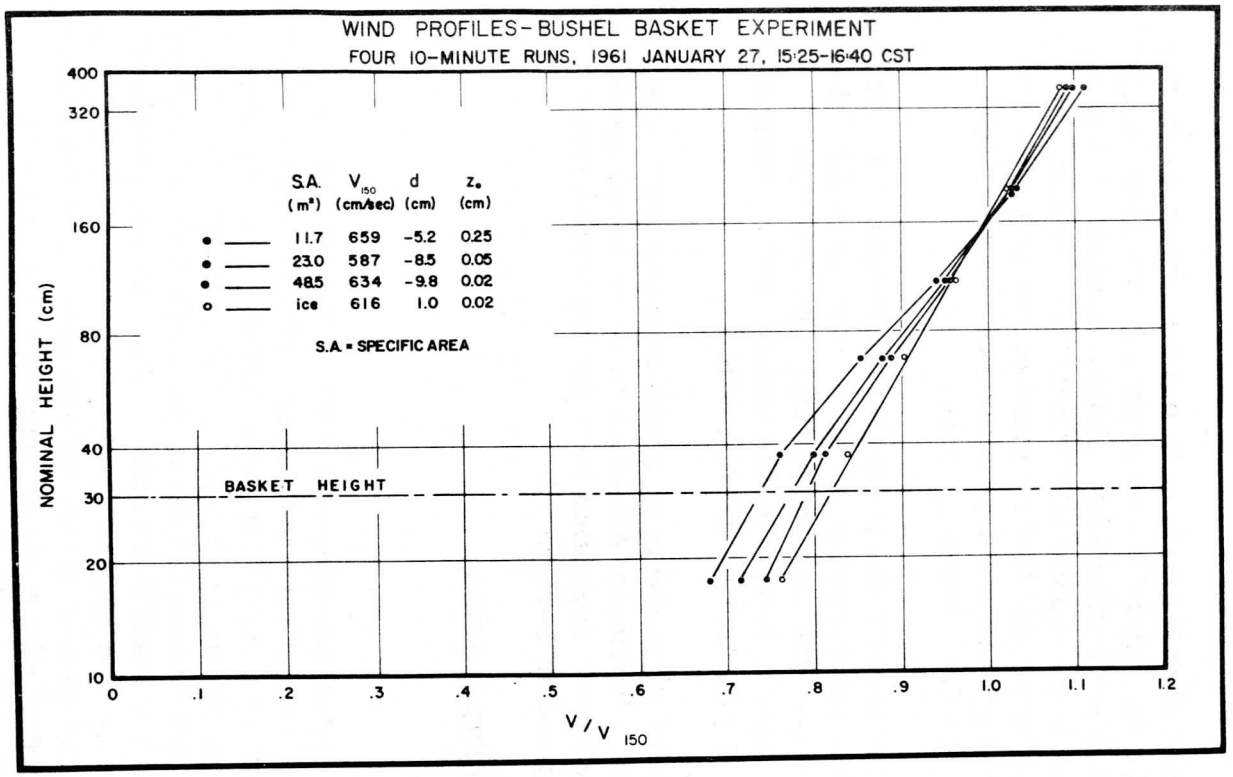

Fig. 4. Wind profile experiment on the ice of Lake Mendota, January 27, 1961. The controlled obstacle parameter was the specific area (S. A.); see Fig. 8 for illustration of obstacle array. Only one run was made at each obstacle density. No control anemometer was used; therefore, wind speeds are presented as the ratio of the wind speed at a given level to the wind speed at 150 cm.

realized that adiabatic lapse rates occur in the atmospheric surface layer as transient states only. Slightly diabatic conditions were permitted. Richardson number requirements will be discussed in Section 7.6.2.

The turbulence produced by an obstacle may be associated with mechanical effects, thermodynamic processes due to differential heating, or both. The effect of differential heating has been minimized in these experiments by the presence of generally overcast skies.

7.3.2 Active control

Approximately 500 commercial bushel baskets placed with their open ends down were used for the controlled modification of roughness at the air-ice interface. It was necessary to remove the handles (leaving 1 cm stubs) to prevent the baskets from sliding on the ice. Three or four people distributed the baskets by hand.

In a typical experiment, an initial number (approximately 100) of baskets were distributed in a fan-shaped area (of approximately 60° angular width) upwind of the main anemometer mast. The upwind extent of the roughness field (R) was usually 50 m or less. To eliminate any edge effect two to four rows of baskets were placed completely around the main anemometer mast. The outside radius (r) of this small circle of baskets was approximately 5 m. For a given area, the density of the baskets was systematically doubled two (or three) times. The general shape and size of the array, the dimensions of the baskets, and their distribution are illustrated in Fig. 2.

Ten-minute mean wind and temperature profiles were obtained before and after each surface modification as well as over the ice at the beginning and end of each experiment. This was done to insure reproducibility of the results, and to eliminate trends or over-all variations due to large-scale meteorological factors. Wind speeds are presented as the ratio of the wind speed at a given level to the wind speed at a control anemometer located at the 3.4 m level approximately 10 m upwind of the roughness field.

Fig. 3 illustrates the wind profiles associated with the basket distributions of Fig. 2. There is a consistent systematic change in wind shear as obstacle density is first increased (solid lines) and then decreased (broken lines). All wind profile parameter computations are based on the average of the two wind profiles obtained for each obstacle density.

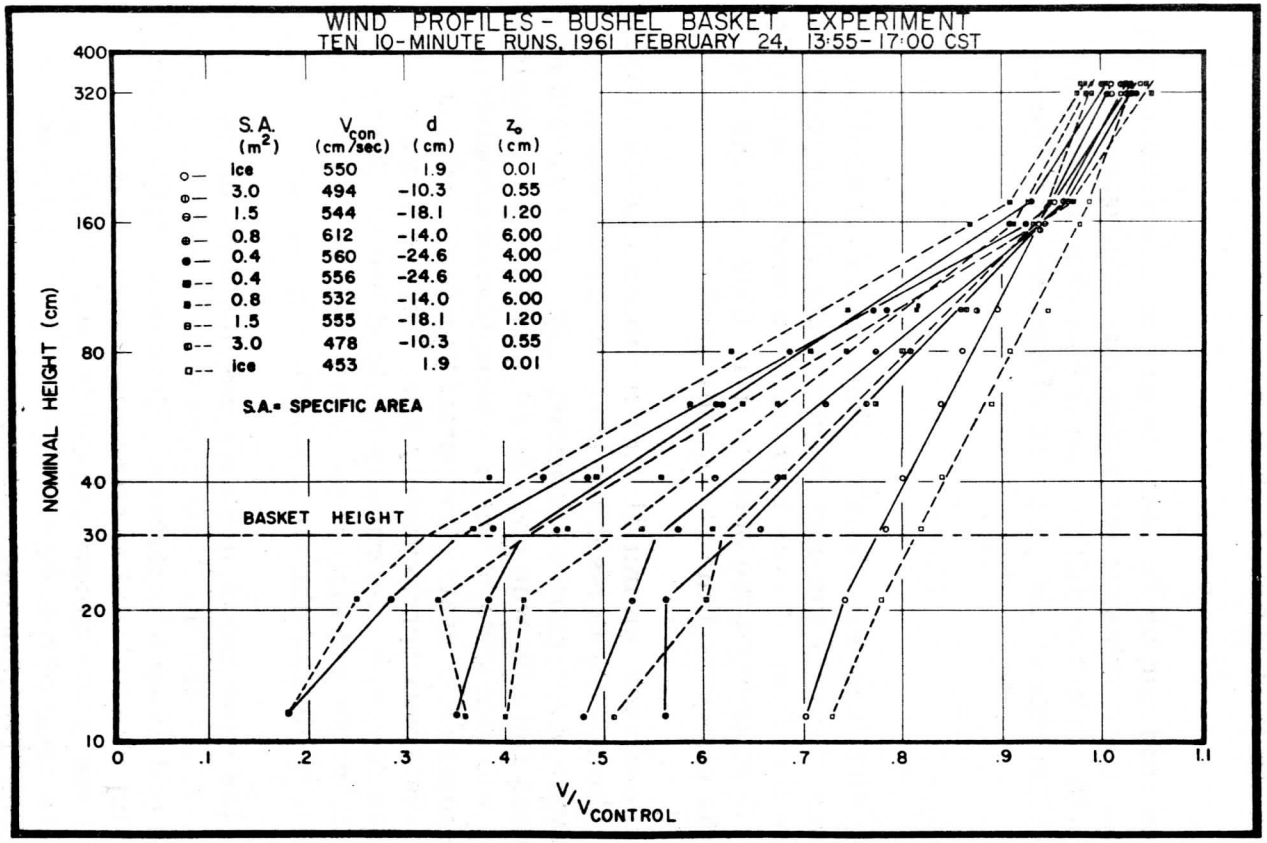

Fig. 5. Wind profile experiment on the ice of Lake Mendota, February 24, 1961. The controlled obstacle parameter was the specific area (S. A.); see Fig. 8 for illustration of obstacle array.

The results discussed in the following sections refer to observations obtained on five different days in the period January through March 1961. Since the experimental procedure and the external conditions varied somewhat from day to day, the date of the experiment is retained for purposes of identification on all graphs and tables. The wind profiles for the five experiments are presented in Figs. 3, 4, 5, 6, and 7. Each experiment is briefly described in the caption and the values of the controlled parameter, the wind speed at the control anemometer, and the computed values of zero point displacement and aerodynamic roughness parameter are summarized in the key.

The range of obstacle densities used in the study is illustrated in Fig. 8. To avoid the continual use of fractions, it is convenient to refer to "basket specific area" S. A. (m^2). As illustrated, S. A. ranged from 48.5 to 0.4 m^2 which is equivalent to the statement that the obstacle density ranged from one basket per 48.5 m^2 to one basket per 0.4 m^2.

Attention is called to the variation in upwind fetch (R) over the roughness field (see Fig. 8). This was unavoidable because of the limited number of baskets available. The possibility exists that the shortest roughness fetch (R = 18 m) was not sufficient for the establishment of a representative wind profile. This point will be discussed in the section on error analysis.

Detailed quantitative data on basket distribution, computed wind profile parameters, and Richardson numbers are summarized in Table 3 in the Appendix.

7.3.3 Instrumentation

It was anticipated that conclusive results could only be obtained with a sufficiently large number of anemometers, spaced more densely in the vertical than is customary for conventional micrometeorological observations. Therefore, the eleven anemometers were located at levels of 10, 20, 30, 40, 60, 80, 100, 160, 180, 320, and 340 cm on the main anemometer mast. The relative spacing of the anemometer levels (determined within a tolerance of ±1 mm) was fixed; however, the entire mast could be moved vertically — its usual zero position being approximately 3 cm above the ice. As a result, the nominal height z (i.e., the measured distance from the ice surface to the center of the anemometer cups) is obtained by adding 3 cm to each of the mast levels. A remote anemometer at a height of 340 cm was used for control purposes.

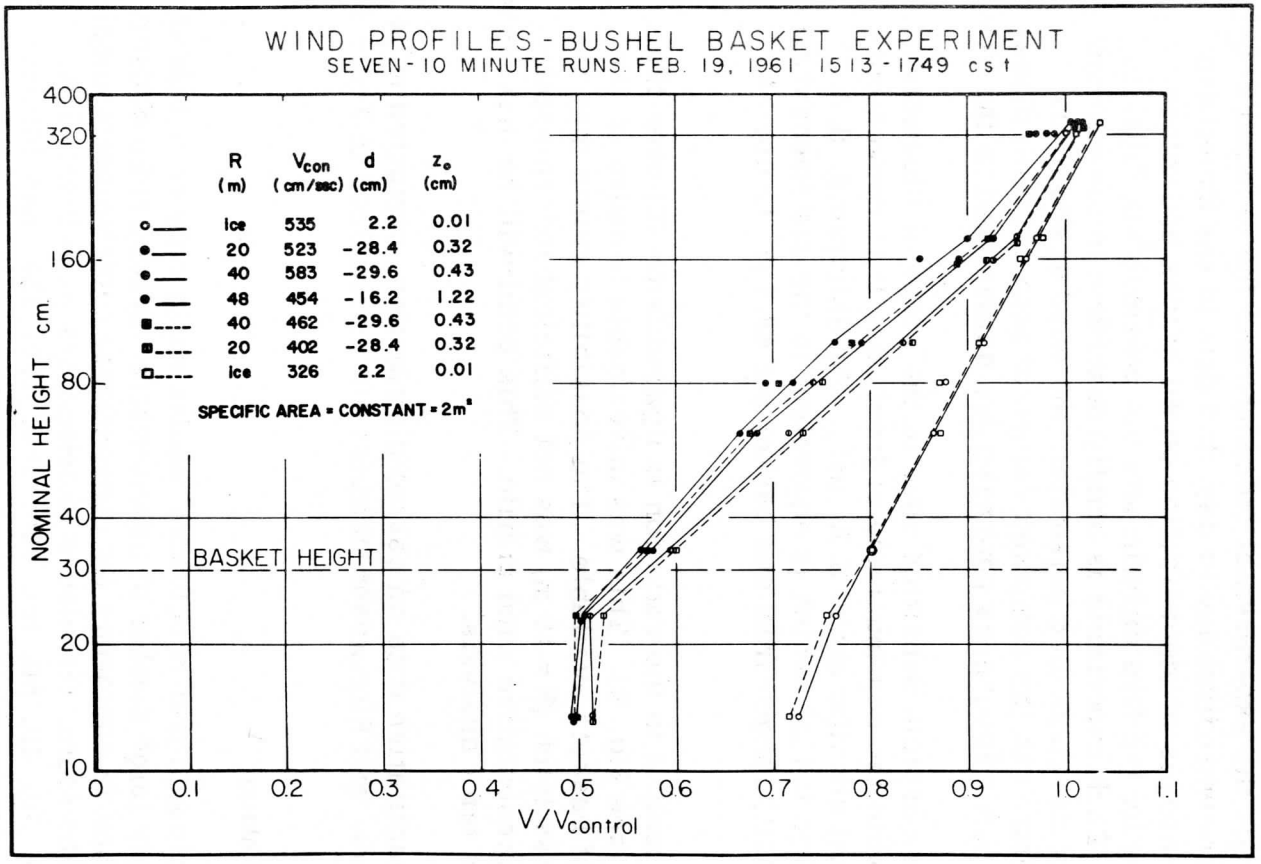

Fig. 6. Wind profile experiment on the ice of Lake Mendota, February 19, 1961. The controlled obstacle parameter was the roughness fetch (R). The specific area (S. A.) was kept constant at 2.0 m^2.

The anemometer (the 3-cup rotor variety with cups of light-weight molded plastic, reinforced with aluminum rings) were designed and manufactured by C. W. Thornthwaite Associates. Shielded, aspirated, thermocouple probes at 20, 40, 80, 160, and 320 cm above the ice provided the data for the temperature profiles. Reference is made to Stearns (1961) for a detailed description of the Department of Meteorology, University of Wisconsin, micrometeorological installation on Lake Mendota.

7.4 Effect of Variations in Obstacle Density on the Wind Profile Parameters

It is well known that under adiabatic conditions in the atmospheric surface layer the mean wind profile is satisfactorily determined by the aerodynamic roughness parameter (z_0), the zero point displacement (d), and the surface stress (τ_0). The three parameters are related by the following equation:

$$V(z) = \kappa^{-1}(\tau_0/\rho)^{\frac{1}{2}} \ln [(z + d + z_0)/z_0] \qquad (1)$$

$$= V^* \ln [(z + d + z_0)/z_0]$$

where κ is the Kármán constant and V^* is the friction velocity.

Lettau (1952, pp. 60 and 75; 1957, p. 334) discusses the necessity of introducing the zero point displacement because of the unlikelihood that the true reference level of the logarithmic model of the wind profile coincides exactly with the nominal reference level (from which z is measured) immediately below the anemometers. Notice that the boundary condition is that $V = 0$ where $z = -d$.

A least-square error technique for the determination of the three wind profile parameters on electronic digital computers is described in Section 6 by Robinson and has been used in the analysis of all wind profile data. The method is essentially the same as that described by Lettau (1957). The computer prints the values of V^*, $d + z_0$, and z_0 necessary to produce a least-squares fit for equation (1), along with the final sum of squared errors. This information is presented in tabular form in the Appendix (see Table 3).

The computed values of z_0, d, and τ_0 will be presented graphically as functions of a non-dimensional variable (A) defined as the ratio specific area (S. A.) over lateral silhouette area. The latter concept is used in aerodynamic drag studies and is defined as the frontal

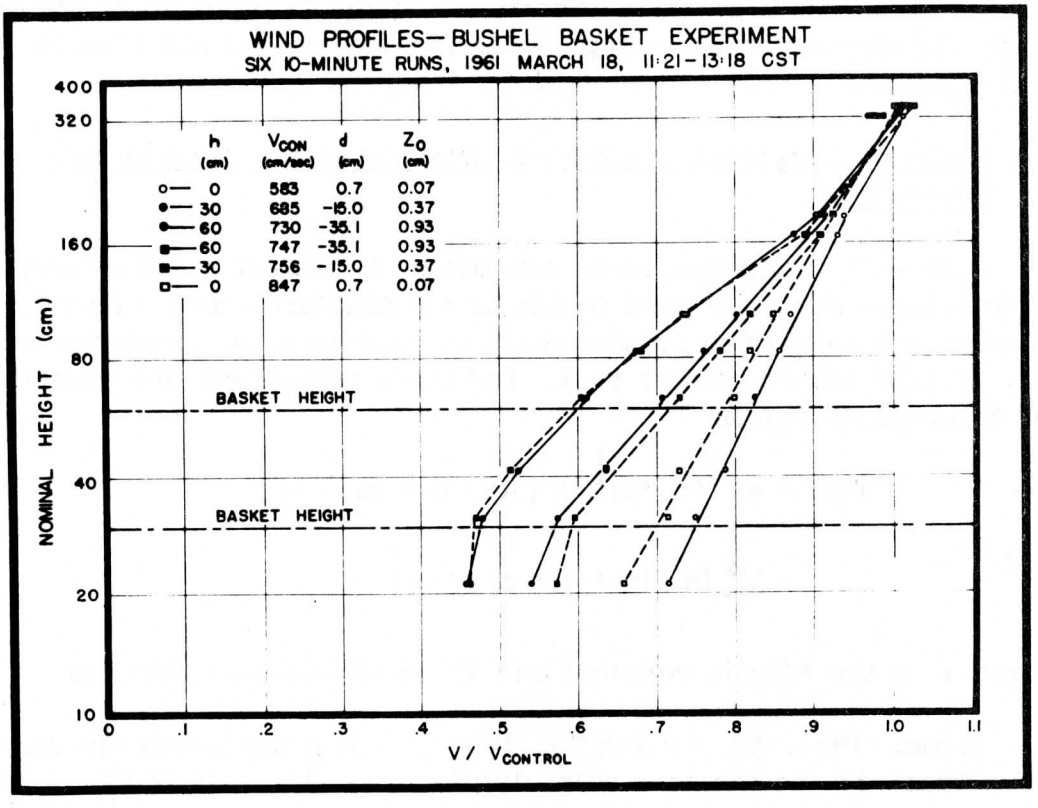

Fig. 7. Wind profile experiment on the ice of Lake Mendota, March 18, 1961. The obstacle height (h) was doubled by inverting the lower basket and placing another basket on top of it. The roughness fetch (R) and the specific area (S. A.) were kept constant at R = 26 meters and S. A. = 4.0 m^2 .

(crosswind, or lateral) area exposed by the body to the flow (Schlichting, 1955, p. 15). Because of the near equality between the silhouette area when the basket is viewed laterally (0.1185 m^2), and from above (0.1385 m^2), the quantity $100/A$ can also be interpreted as the percentage of the horizontal roughness field covered by obstacles. The area covered by baskets ranged from 0.25 to 30% of the total area of the roughness field when calculated in this manner — the exact range was from 0.3 to 35%. The use of the non-dimensional variable A allows the inclusion of the results from the variation in obstacle height (March 18, 1961) with the rest of the data.

A linear least-square error method was used to obtain a power law relating the computed values of z_0, d, and τ_0 to a non-dimensional variable A over the limited range of obstacle densities used in this study ($3.4 \leq A \leq 410$). It will be discussed later that these power law relationships cannot be expected to hold over the range of all possible obstacle densities, but they permit us to compare the results of this study with similar experiments conducted in ducts and wind tunnels.

7.4.1 Aerodynamic roughness parameter

The variation in the aerodynamic roughness parameter (z_0) with obstacle density from the results of the present study is indicated in Fig. 9. Notice that z_0 varied by more than two orders of magnitude from its initial value over the ice. The line of best fit shows that z_0 is proportional to $A^{-1.1}$. A decrease in z_0 is indicated for the final increase in obstacle density; however, this may be spurious due to scatter in the data.

Schlichting (1937) has reported on roughness experiments in the laboratory using obstacles of various shapes and sizes fastened to the bottom of a water-filled duct under fully developed turbulent conditions. He has described the hydrodynamic roughness of these obstacles in terms of k_s, the diameter of tightly packed grains of sand that would produce an equivalent hydrodynamic roughness. To compare Schlichting's data with our own we consider that z_0 equals h/N for fully turbulent flow in rough ducts when $h = k_s$. Nikuradse (1933) found $N = 30$ assuming a logarithmic velocity distribution for the entire duct cross section, and $\kappa = 0.40$. In Section 8 Lettau describes a new mathematical model for the universal velocity distribution law under fully turbulent conditions in rough ducts for which Nikuradse's measurements yield $\kappa = 0.428$ and $N = 23.9$. The expression $z_0 = k_s/23.9$ is used to transform Schlichting's values of k_s into values of z_0. This is done in Fig. 10, where the ordinate is a

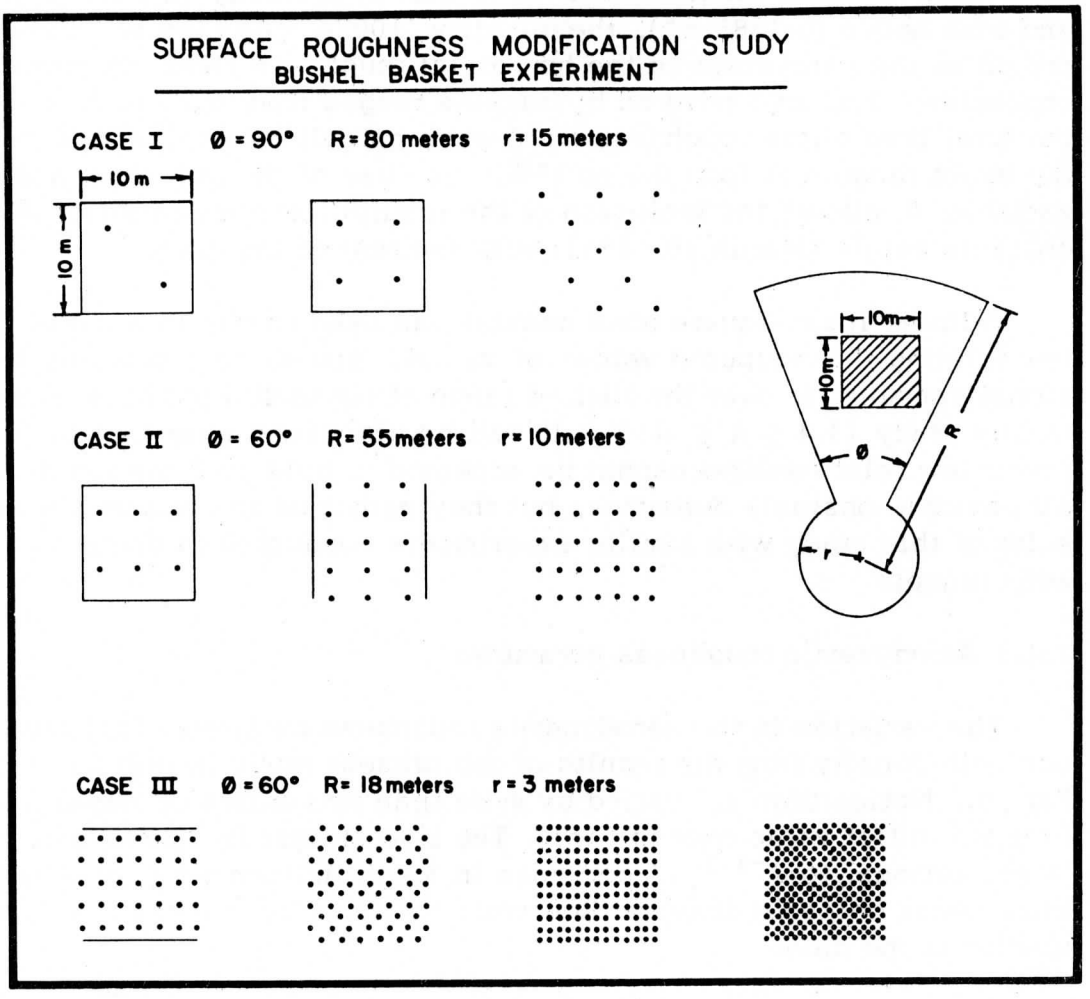

Fig. 8. The range of obstacle densities (drawn to scale) and the general shape and size of the roughness field for three controlled wind profile experiments on the ice of Lake Mendota, 1961.

Case I	January 27	S. A. = 48.5, 23.0, 11.7 m^2
Case II	February 15	S. A. = 14.7, 7.7, 4.0 m^2
Case III	February 24	S. A. = 3.0, 1.5, 0.8, 0.4 m^2

non-dimensional variable defined as the ratio of the aerodynamic roughness length (z_0) to the geometric height of the obstacle (h). The similarity between the line of best fit from the basket experiments and the data from Schlichting's experiments is apparent. Notice that z_0/h for Schlichting's spheres reaches a maximum at A-values of approximately 3 and decreases for further increases in obstacle density.

More recently, Sayre (1961) has described the effect of roughness spacing on open channel flow for roughness elements consisting of sheet-metal baffles. He notes the general tendency for his spacing parameter (hydrodynamic roughness/obstacle height) to increase with increasing roughness density. Using our notations, his obstacle density varied from A approximately equal to 67 to A approximately equal to 4.

The reason for the observed variations in aerodynamic and hydrodynamic roughness can be explained as follows. The addition of obstacles at an initially smooth surface causes increased resistance to the flow near the surface. If the obstacle density approaches saturation (100% of the total area) and if there is little separation between obstacles (i.e., parallel sides) another smooth surface is established at the height of the obstacles. Therefore, the optimum roughness may occur at an obstacle density less than saturation.

It is perhaps instructive to compare certain expressions that have been used to relate z_0 to h with the plots of z_0/h versus A illustrated in Fig. 10. From observations obtained over snow, grassland, and beet fields, Paeschke (1937) has found $z_0 = h/7.35$. In Section 3 Kung shows that $z_0 = h^{1.19}/17.4$ for tall vegetation ranging from grass types ($z_0 \approx h/10$) to forest trees ($z_0 = h/4$). The ratios given by Nikuradse and Lettau have been discussed. The values of z_0/h obtained by these investigators are illustrated along the left-hand margin of Fig. 10. The expressions of both Paeschke and Kung seem to be valid only for the maximum obstacle densities used in this study (i.e., A = 3.4 to 7 or roughly 30 to 14% of the surface area covered with baskets), and for the region containing the peak in the roughness curve of Schlichting's spheres. The ratios of both Nikuradse and Lettau, which pertain to sand type roughness in duct flow, seem to be valid only when $A \approx 16$ for the baskets and $A \approx 1.3$ or 30 for the spheres. Clearly, aerodynamic roughness is a function of obstacle density as well as obstacle height.

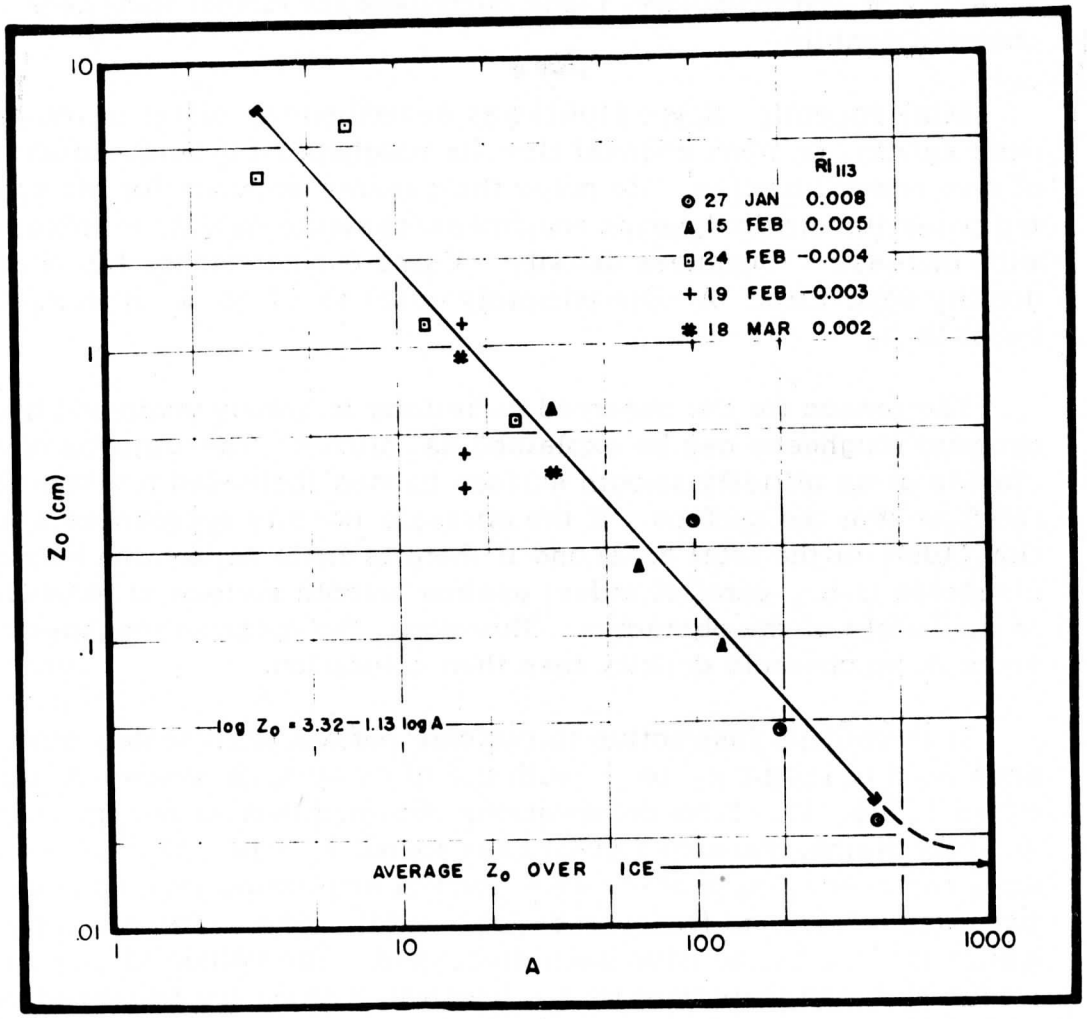

Fig. 9. The aerodynamic roughness parameter (z_0) versus A for five controlled wind profile experiments on the ice of Lake Mendota, 1961. The solid line indicates the linear least-square error fit. The broken line indicates an asymptotic approach to the average value of z_0 over the unmodified ice.

7.4.2 Zero point displacement

The values of d obtained over the unmodified ice are very small (approximately 2 cm) and are presented in Section 7.6. Recalling the boundary condition for equation (1) and noting that all values of d obtained from wind profiles over obstacles are negative and that $|d| \leq h$, we conclude that $V = 0$ for the logarithmic model of the wind profile at some height between the surface of the ice and the tops of the obstacles. Actual wind profiles and computed solutions to equation (1) from the actual wind profile data are plotted on a linear height scale in Fig. 11 to illustrate the zero point displacement. The cases shown refer to the wind profile over the unmodified ice and the wind profile over the maximum obstacle density (S. A. = 0.4 m^2) on February 24.

The variation in d with obstacle density is shown in Fig. 12. The ordinate is a non-dimensional variable defined as the ratio -d over h. The line of best fit shows that -d/h is proportional to $A^{-0.29}$. That is, -d increases with obstacle density but at a significantly smaller rate as z_0 increases with obstacle density.

Neither of these power law relationships should be expected to hold for further increases in obstacle density. The quantity -d/h must approach unity asymptotically as obstacle density approaches 100%, while z_0/h may have a maximum for some obstacle density and be decreasing as the obstacle density approaches 100% (as in the case of Schlichting's spheres).

7.4.3 Surface stress

The variation in surface stress τ_0 with obstacle density is illustrated in Fig. 13. The ordinate is the square of a non-dimensional variable defined as the ratio os the friction velocity at the modified rough surface to the friction velocity at the ice surface — $(V^*/V^*_{ice})^2$. This expression reduces the ratio τ_0 for the obstacle field over τ_0 for the ice if κ is a true constant. Notice that τ_0 over the maximum density is nearly an order of magnitude greater than τ_0 over the ice. The line of best fit shows that $(V^*/V^*_{ice})^2$ is proportional to $A^{-0.49}$. A heavy dashed line extends from the line of best fit at low obstacle densities to indicate that $(V^*/V^*_{ice})^2$ must approach unity asymptotically as obstacle density becomes small.

Comparison with Schlichting's data is possible. He lists values of shearing velocity v^*_r for the rough wall of his duct and v^*_g for the

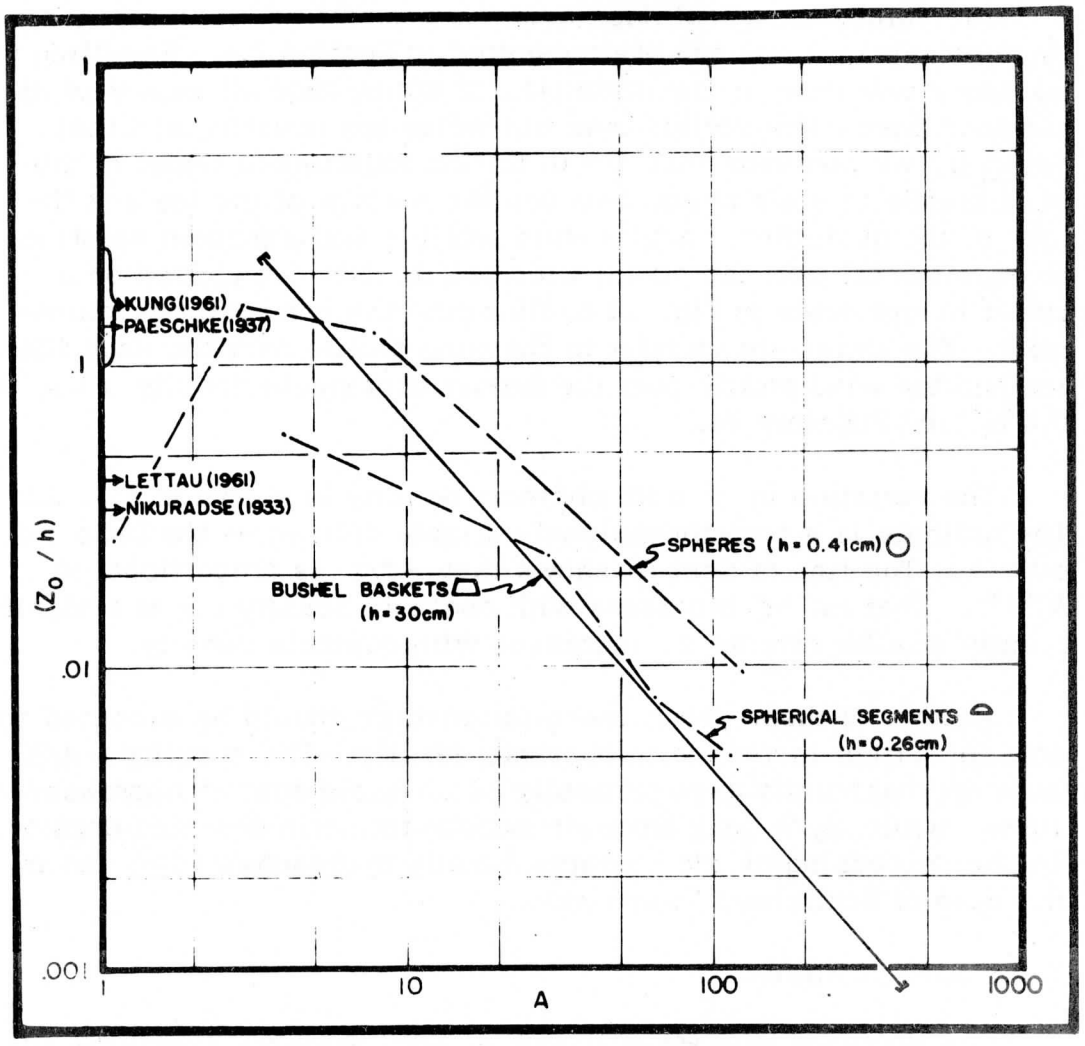

Fig. 10. The ratio of the aerodynamic roughness parameter (z_0) to the obstacle height (h) versus A. The solid line indicates the line of best fit from the basket study. The broken lines refer to recomputed data from the laboratory experiments of Schlichting (using $z_0 = k_s/23.9$). The ratios of z_0/h obtained by various investigators are indicated along the left-hand margin.

smooth wall, for a number of different obstacles and a variety of duct flow speeds. Using this data, values of $(v^*_r/v^*_g)^2$ have been computed for spheres and spherical segments as functions of A and are illustrated in Fig. 13. The values pertain to flow speeds at the center of the channel of 570 ±20 cm/sec. The rate of increase in surface stress with obstacle density indicated by Schlichting's data is less than that indicated by the baskets. A maximum surface stress is indicated for the spheres at $A \approx 3$.

Moore (1951), in a series of wind tunnel tests, determined aerodynamic drag as a function of the density of small wooden cubes arranged in a diagonal square pattern. He states that a curve of drag versus spacing exhibited a broad maximum extending from a relative spacing of 3 to 6 times the side of the cube, which corresponds to $16 \leq A \leq 49$ in our notation. This effect was not observed in the basket experiments. A slight decrease in $(V^*/V^*_{ice})^2$ does occur for the final increase in obstacle density; however, this may be spurious due to scatter in the data.

7.4.4 Geostrophic drag coefficient — Surface Rossby Number

Attention is called to the drastic changes in the appearance of the wind profiles and in the values of the computed profile parameters that are produced by the controlled modification of the surface roughness. This is particularly noticeable in the profiles of February 24, 1961 (see Figs. 5 and 12). Wind shear between 50 and 150 cm is tripled, wind speed immediately above the obstacles is more than halved, z_0 is increased by more than two orders of magnitude and τ_0 by nearly one. Ellison (1957) has made the following statement: "The only effect of a change in the value of z_0 is to superimpose a uniform translation on the whole flow without modifying its internal mechanism." Clearly, our experiments show that a change in z_0 does have more complex consequences than a simple translation. There is an additional adjustment between surface stress and surface wind speed. This leads us to search for a truly ambient wind speed, or reference speed.

Lettau (1958) has suggested that the horizontal pressure gradient, or, consequently, the geostrophic wind in the atmospheric surface layer, assumes the role of an over-all forcing function similar to that of the pressure head, or the center speed in duct flow, or the ambient speed in wind tunnel experiments. He has shown the dependency of the geostrophic drag coefficient,

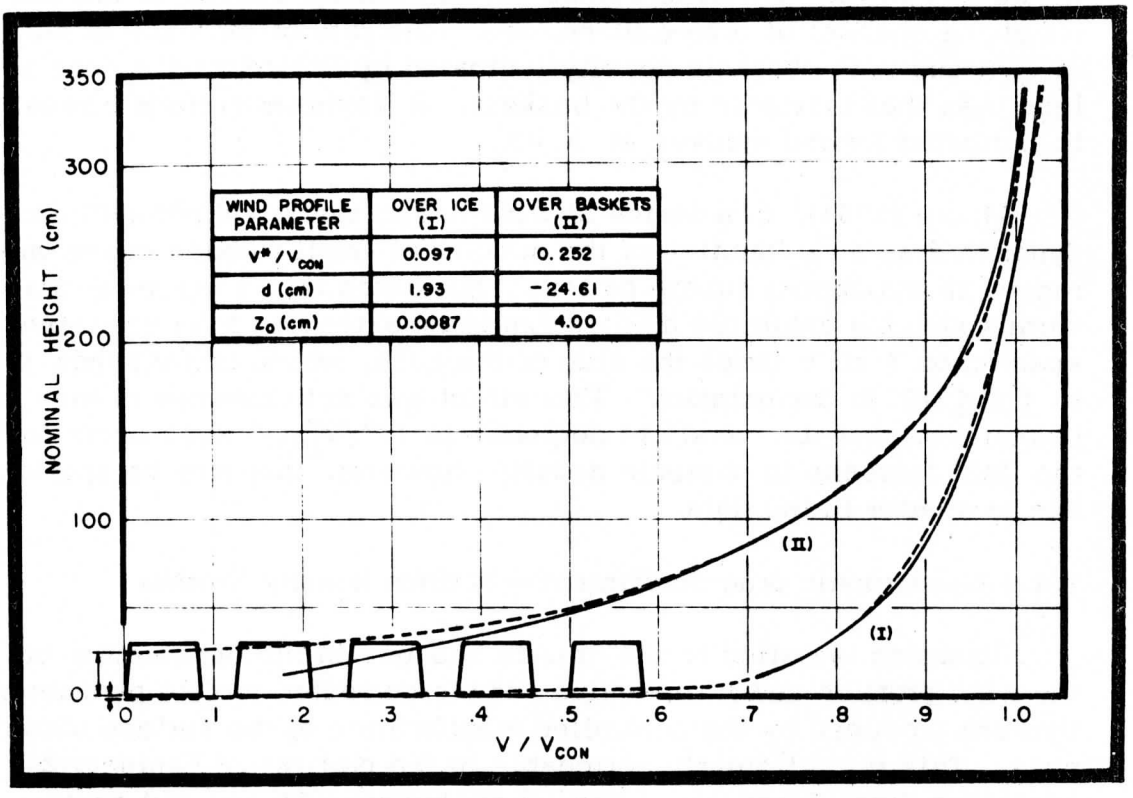

Fig. 11. Actual wind profiles (solid lines) and computed solutions to equation 1 (broken lines) over the unmodified ice (I) and over the maximum obstacle density (II — S. A. = 0.4 m^2) for a controlled wind profile experiment on the ice of Lake Mendota, February 24, 1961. The zero point displacement (d) for each of the computed profiles is indicated along the left-hand margin.

$$C = (\tau_0/\rho)^{\frac{1}{2}}/V_{g,o} \qquad (2)$$

on what he defines as the Surface Rossby Number,

$$\underline{Ro}_0 = V_{g,o}/z_0 f \ . \qquad (3)$$

Lettau obtained an empirical relationship relating C and $\underline{Ro}_0$ from micrometeorological data available at that time. More recently, Lettau (see Section 9) has computed the geostrophic drag coefficient of theoretical wind spirals (a generalized concept of Ekman spirals) as functions of $\underline{Ro}_0$. The present theoretical and 1958 empirical relationships along with the data from the basket experiments are presented in Fig. 14.

The shape of the experimental curve is steeper than that of the 1958 empirical relationship, which in turn is steeper than the theoretical curve. This result, however, should be expected. In the theory, full adjustment between wind and stress distribution throughout the entire planetary boundary layer is assumed. In view of the average thickness of this layer, upwind fetches over uniform terrain of the order of 100 km are required. In the selection of conventional micrometeorological sites, actual fetches over uniform terrain will normally be between 100 m and 10 km. The roughness fetches in our experiments were always less than 100 m. Clearly, such short distances will not allow the wind profile to establish a balance. The establishment of a balance requires a change in the direction of the surface wind — namely, an increasing component towards lower pressure to compensate for increasing frictional drag. No changes in wind direction were evident in our experiments.

The discrepancy between the January 27 data and the rest of the points in Fig. 14 is probably due to an over-estimate of $V_{g,o}$. The method used in the determination of $V_{g,o}$ and the values obtained are summarized in the Appendix (Table 5).

7.5 Supplementary Results

A determination of τ_0 independent of equation (1) is desirable. Lettau (1961) has outlined such a method based on continuity of horizontal momentum for two-dimensional, steady state flow. The generalized equation of conservation reduces to the form,

$$\frac{\partial}{\partial x}(\rho q u) + \frac{\partial}{\partial z}(\rho q w) = 0 \qquad (4)$$

where q = conservative property of the fluid per unit mass.

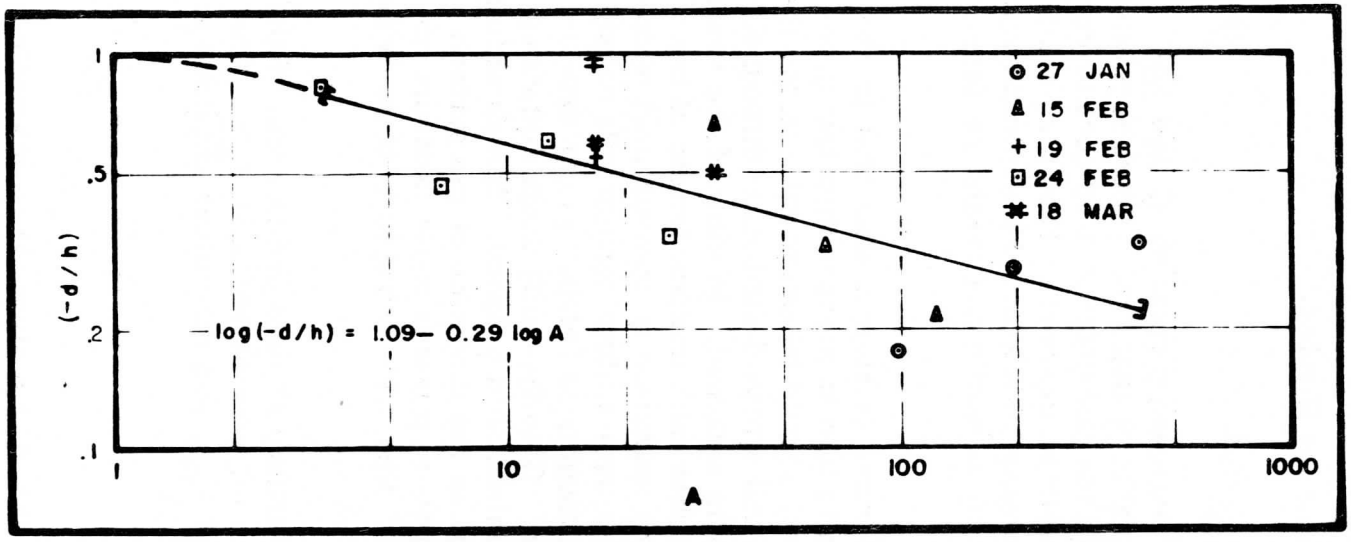

Fig. 12. The ratio of negative zero point displacement (-d) to the obstacle height (h) versus A for five controlled wind profile experiments on the ice of Lake Mendota, 1961. The solid line indicates the linear last-square error fit. The broken line indicates that (-d/h) must approach unity asymptotically (for the baskets) as A approaches unity.

Integrating with respect to height from the surface to some height z, and interchanging the sequence of integration (with respect to z) and differentiation (with respect to x), we obtain

$$(\rho qw)_o = (\rho qw)_z + \frac{\partial}{\partial x}\int_o^z \rho q u dz \quad . \tag{5}$$

Setting $q = 1$ in (5), and noting that for a horizontal solid boundary $(\rho w)_0 = 0$, we have

$$(\rho w)_z = -\frac{\partial}{\partial x}\int_o^z \rho u dz \quad . \tag{6}$$

Equation (6) can be used to determine the vertical velocity at various heights (z) in a truly two-dimensional flow.

Substituting (6) into (5) gives

$$(\rho qw)_o = -q_z \frac{\partial}{\partial x}\int_o^z \rho u dz + \frac{\partial}{\partial x}\int_o^z \rho q u dz \quad . \tag{7}$$

Select a level H such that for $z \geq H$ we have $\partial q/\partial x = 0$ for any x. Then,

$$(\rho qw)_o = \frac{\partial}{\partial x}\int_o^H \rho u(q - q_H)\, dz \quad . \tag{8}$$

The result of averaging over the finite distance $R = x_2 - x_1$ is

$$\overline{(\rho qw)_o}^{x_1}{}_{x_2} = \frac{1}{R}\int_o^H \rho[u_2(q_2 - q_H) - u_1(q_1 - q_H)]\, dz \quad . \tag{9}$$

Finally, for the case of horizontal momentum, substitute $q = u$, $q_H = U$ (such that $\partial U/\partial x = 0$).

$$\overline{\tau_0}^{x_1}{}_{x_2} = \overline{-(\rho uw)_o}^{x_1}{}_{x_2} = \frac{\rho}{R}\int_o^H [u_2(U - u_2) - u_1(U - u_1)]\, dz$$

$$= \frac{\rho}{R}\int_o^H [U(u_2 - u_1) - (u_2^2 - u_1^2)]\, dz \quad . \tag{10}$$

This solution reduces to the von Kármán relation (see Sutton, 1953, p. 55) for the special case when $u_1 = U$ at $x_1 = 0$ and $u_2 = u$ at $x_2 = x$, which is true for the development of a flat-plate boundary

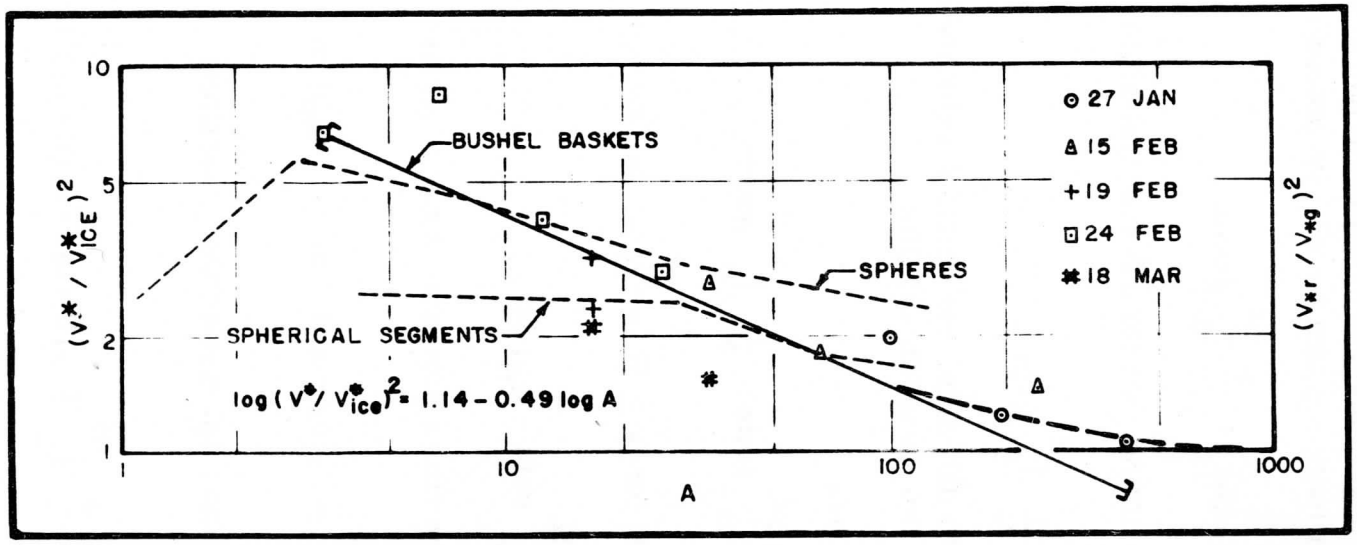

Fig. 13. The square of the ratio of the friction velocity over the roughness field (V^*) to the friction velocity over the unmodified ice (V^*_{ice}) versus A for five controlled wind profile experiments on the ice of Lake Mendota, 1961. The solid line indicates the linear least-square error fit. The heavy broken line indicates that $(V^*/V^*_{ice})^2$ must approach unity asymptotically (for the baskets) as A becomes large. The thin broken lines refer to recomputed data from the laboratory experiments of Schlichting.

layer downstream from the leading edge, in an initially uniform wind tunnel flow.

7.5.1 Experimental determination of the Kármán constant

Combining the result of equation (10) with the slope of the wind profile V^* from equation (1) we obtain a direct estimate of the Kármán constant,

$$\kappa = \left(\int_{x_1}^{x_2} \tau_0 \, / \rho \right)^{\frac{1}{2}} / V^* \quad . \tag{11}$$

Equation (11) is used to estimate κ during three experiments in which less than $\pm 3\%$ change in wind speed occurred at the uppermost anemometer level (see Figs. 5, 6, and 7). The method is not exact because the velocity distribution above the highest anemometer level is unknown. The κ-values obtained are listed in Table 1.

The average of the nine κ-estimates is 0.41 with a standard deviation of 0.07. The average value is in satisfactory agreement with accepted values and the spread is not unreasonable for a calculation of this type.

The numerical evaluation of equation (10) was accomplished by plotting the profiles on a linear height scale and reading values of u_2 (wind profile over baskets) and u_1 (wind profile over unmodified ice) at 5 cm height intervals. The velocity defect $(u_2 - u_1)$ was obtained directly from a velocity defect profile, thus eliminating the effect of systematic errors in measurement.

7.5.2 Vertical velocity pattern over the roughness field

As previously mentioned, equation (6) allows the deduction of the vertical motion pattern over the roughness field. The experiment of February 19 is well suited for this purpose because the roughness fetch R was varied. The resulting values of mean vertical velocity apply to mean distances of 10, 20, and 24 meters from the leading edge of the roughness field and indicate the rate at which the mean streamlines are displaced upward.

Assuming $w \sim x^n$, the value of n was obtained for each of three levels from a log-log plot of the data (see Fig. 15). The exponent n varied from -0.7 to -0.6 to -0.5 for w evaluated at 1, 2, and 3.4 meters, respectively, above the surface. Vertical motions of 3 to 4 cm/sec are indicated at heights of 2 m and distances of 15 to 20 m downwind from the leading edge of the roughness field.

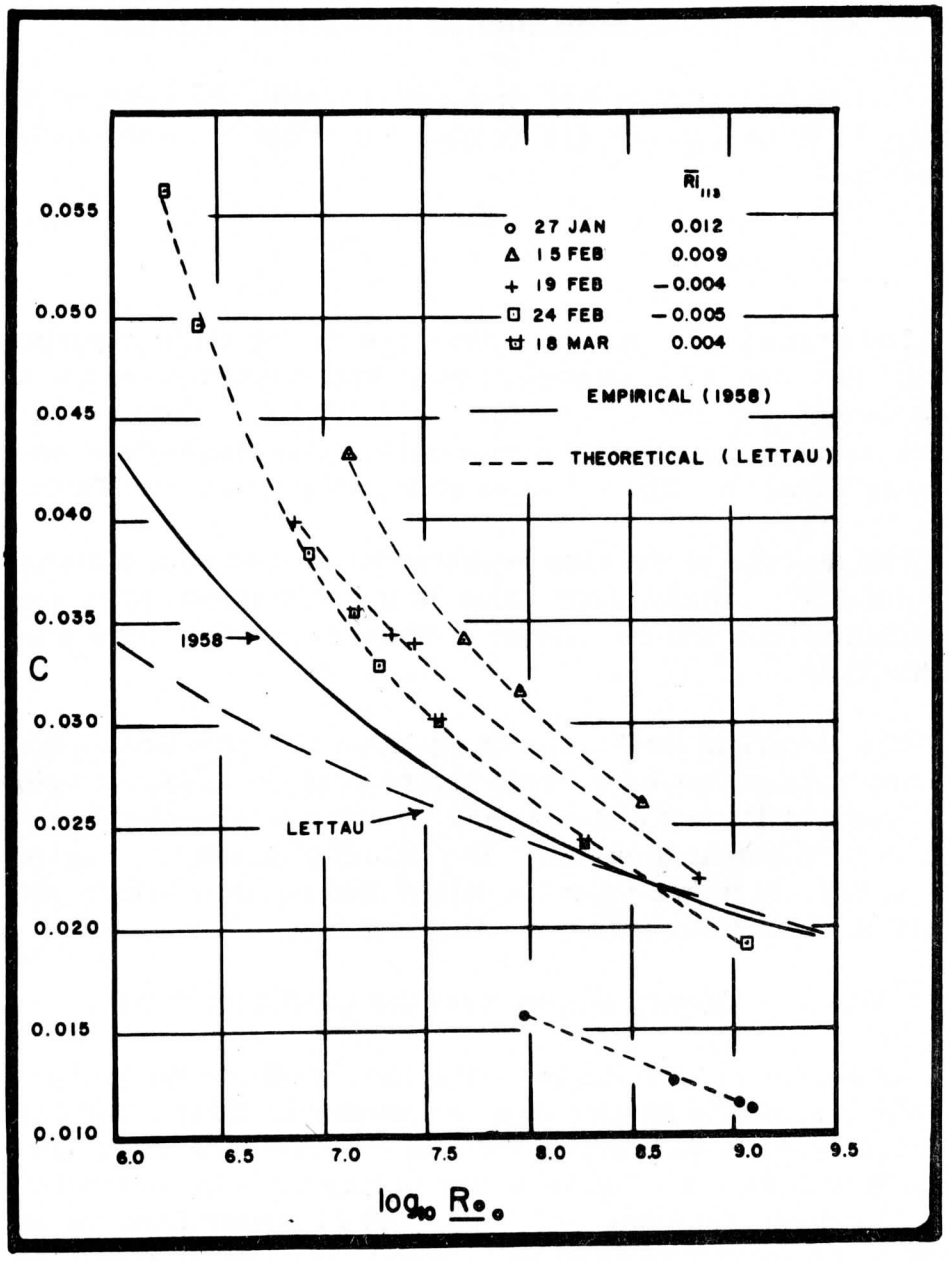

Fig. 14. Geostrophic drag coefficient versus Surface Rossby Number. The short broken lines refer to the values obtained during five controlled wind profile experiments on the ice of Lake Mendota, 1961.

If we assume that at and above some level the mean flow pattern is undisturbed by the presence of the roughness field, momentum continuity for two-dimensional, steady state flow requires an increase in horizontal wind speed below this level to compensate for the decrease in horizontal wind speed within and immediately above the roughness field. This effect is observed in the profiles of February 15 (see Fig. 3).

7.5.3 Wind speed between the obstacles

The wind speed in the air layer between the roughness elements is strongly dependent upon the position of the nearest obstacles. The baskets near the anemometer mast were arranged such that the mast occupied the position that would ordinarily be occupied by an obstacle. As a result, the indicated speeds should be quite representative. Fig. 16 illustrates the ratio of wind speed at 20 cm within the layer of air between the baskets (V_{20}) to the wind speed at the same level over the unmodified surface ($V_{20,ice}$) as a function of A. Notice that $V_{20}/V_{20,ice}$ is 0.5 when only 15% of the roughness field is covered with obstacles.

7.5.4 The drag coefficient of the individual basket

The drag coefficient of an individual bushel basket was not determined directly. Schlichting (1937) gives an expression for determining the drag coefficient (C_f) of an individual roughness element from measurements of the geometry of the obstacle field, the fluid velocity at the obstacle height, and the friction velocity at the rough wall (basket roughness field) and the smooth wall (unmodified ice).

A nearly constant value of $C_f = 0.45$ was obtained for the bushel basket using Schlichting's equation. This was in contrast to the behavior of Schlichting's spheres which show a decrease in C_f from approximately 0.89 at $A = 100$ to approximately 0.20 at $A = 3$.

7.6 Error Analysis

7.6.1 Anemometry

Simultaneous comparison of the twelve Thornthwaite anemometers on a horizontal bar was made immediately before and after each experiment. The results were averaged and correction terms applied to individual anemometers. In general, corrections were less than 1%.

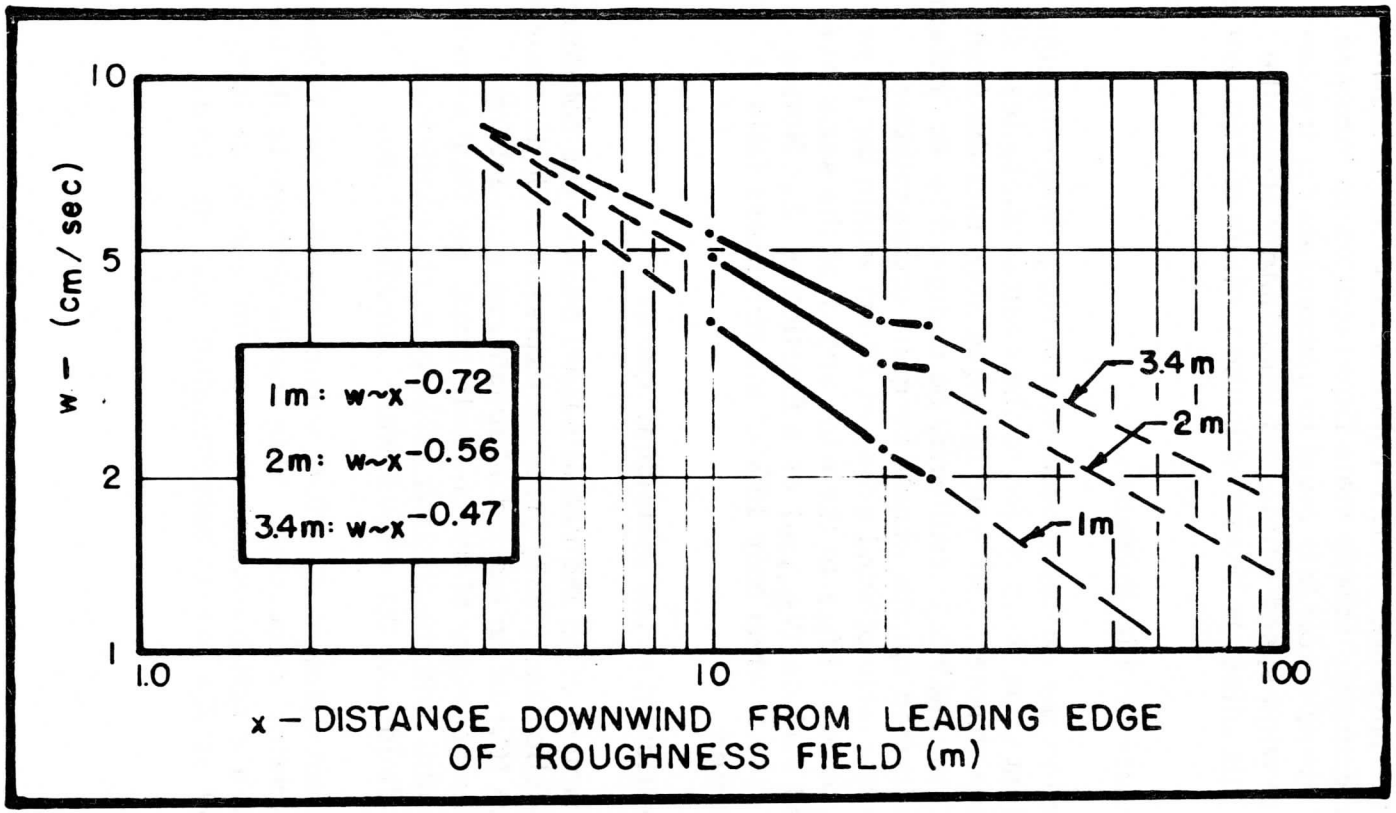

Fig. 15. Vertical component of mean velocity (w) computed from equation (6) versus downwind distance from the leading edge of the roughness field (x) for a controlled wind profile experiment on the ice of Lake Mendota, February 19, 1961.

In an attempt to obtain a more detailed profile, it was necessary to stagger the anemometers on the mast. Slight changes in wind direction caused the anemometers more nearly "upwind" of the mast to slow down. The resulting spread in measured wind speeds at adjacent levels is obvious on the profiles of February 24 and February 19 (see Figs. 5 and 6). This spread introduces some uncertainty into the wind profile, but the use of the least-square technique in the analysis of the wind data avoids any serious misinterpretations.

7.6.2 Effect of thermal stratification

The Richardson number, $\underline{Ri}$, was computed at four levels from averages of temperature samples obtained every 30 seconds and from the 10-minute average wind shear. These values are listed in Table 3 in the Appendix. A practical criterion for thermal stratifications sufficiently close to neutral is $|\underline{Ri}_{100}| \leq 0.003$.

Lettau (1957) defines a bulk parameter (Ri)' as a measure of the over-all convective stability of a layer.

$$(Ri)' = \sum_i Ri(z_i) / \sum_i z_i \quad . \tag{12}$$

For practical purposes (Ri)' expressed in units of 10^{-3} per meter can be considered numerically equal to $\underline{Ri}$ times 10^{-3} at $z = 100$ cm. For the Great Plains Turbulence Field Program, using the bulk parameter (Ri)' Lettau (1957, p. 331) has classified as weak lapse (Ri)' between -9 and -5, as neutral (Ri)' between -4 and +4, and as weak inversion (Ri)' between +5 and +6. These terms are used in a relative sense because the over-all wind speed during the program was large.

The values of $\underline{Ri}_{113}$ and (Ri)' from this study have been averaged for all wind profiles over the baskets and for the wind profiles over the ice. The results are summarized in Table 2. The presence of the baskets increases the wind shear sufficiently to reduce $\underline{Ri}_{113}$ and (Ri)' to near neutral conditions. The extent of reproducibility of the wind profile parameters over the ice is also noted in Table 2.

Hourly observations of cloud cover, temperature, wind direction and wind speed, and station pressure have been obtained from the United States Weather Bureau located at Truax Field, Madison, Wisconsin. These observations, along with computed values of air density are summarized for each experiment in Table 4 in the Appendix.

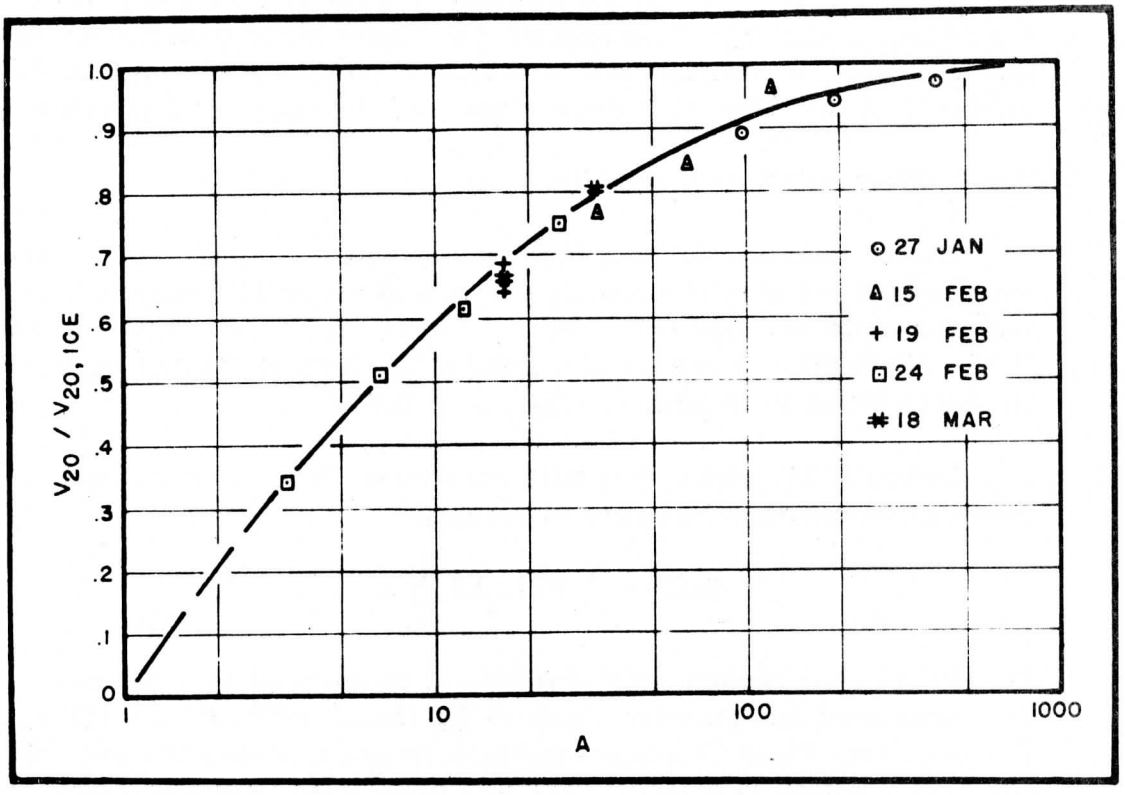

Fig. 16. The ratio of the wind speed at 20 cm within the layer of air between the obstacles (V_{20}) to the wind speed at 20 cm over the unmodified ice ($V_{20,ice}$) versus A for five controlled wind profile experiments on the ice of Lake Mendota, 1961. The broken line indicates the limiting values of ($V_{20}/V_{20,ice}$).

7.6.3 Representativeness of the wind profiles

There is some question concerning which anemometer levels to include in the wind profile parameter computations.

Anemometers below and immediately above the basket height reflect the flow over and around an individual obstacle and not the statistical effect of all obstacles. A number of computations were made on all profiles omitting the lowest anemometers one by one. It was found that systematic variations in the profile parameters could be obtained only by excluding the anemometer located immediately above the baskets (31, 32 cm), and all levels within the layer of air between the baskets. This result was considered for all computations.

The possibility that in some cases the anemometers at the highest levels might be outside the modified layer was discussed in Section 7.4. The problem is somewhat akin to the growth of an "internal boundary layer" referred to in fluid dynamics. An attempt was made on February 19 to investigate this effect by systematic variation of the upwind extent of the roughness field while keeping the density distribution constant. The resulting profiles are indicated in Fig. 6 and are discussed below.

R = 20 meters: A "kink" appeared in the profile above the 160 cm level. This suggests that higher levels were not yet modified by the roughness field. A similar "kink" was observed in the profiles of February 24 when R = 18 m (see Fig. 5).

R = 40 meters: Further modification (approximately a 5% decrease in wind speed) occurred in the middle portion of the wind profile. The "kink" in the profile was not as sharp as on the previous run and the slope of the profile above the 160 cm level increased. This indicates that modification extended above the 160 cm level.

R = 48 meters: Further modification (less than a 5% decrease in wind speed) occurred in the middle and upper portion of the profile. Unfortunately, no second run was made for this fetch.

If all anemometer levels above the height of the baskets are used in the computation of the profile parameters for the case R = 20 m, we find $-d = 44.6$ cm and $z_0 = 0.025$ cm. If anemometer levels above the 180 cm level (i.e., above the "kink") are omitted, we find $-d = 28.4$ cm and $z_0 = 0.322$ cm. The latter values are in close agreement with the results of the computations for R = 40 m in which all

levels were included. Using anemometer levels located above the modified layer will lead to overestimating the -d value and underestimating z_0. The decrease in -d and the increase in z_0 for R = 48 m must be considered uncertain because only one run was made for this roughness fetch.

The following convention was adopted:

1. Anemometer levels above 180 cm were not included in the analysis of the profile parameters for $R \leq 20$ meters.

2. All anemometer levels were included in the analysis of the profile parameters for $R > 20$ meters.

As previously mentioned, Lettau (1959) has suggested as a "rule of thumb" that the highest instrument level should not exceed $\approx$ 1/50th of the upwind distance from significant discontinuities in the surface structure. On the basis of the appearance of the profiles, instrument levels at heights $\tilde{=}$ 1/10th the upwind fetch over the baskets have been included. As a result, the parameters obtained may not be completely representative of the surface.

The problem of the growth of the internal boundary layer must be examined more closely in future experiments.

7.7 Conclusions

The value of controlled modification of surface roughness on wind profile structure has been demonstrated by the results of this study.

The systematic increase in obstacle density on the ice surface results in a tripling of the wind shear, an increase of more than two orders of magnitude in z_0, and an increase of nearly one order of magnitude in τ_0. In addition to providing direct information on the variation of the wind profile parameters with the geometry of the surface, the technique has obvious applications to the study of various other micrometeorological problems.

Future plans, as outlined by Lettau (1959), include the use of obstacles with different albedo to absorb or reflect solar radiation — thus producing varying correlation between the momentum sink structure and the heat source pattern. Also, the vertical fluxes of heat and moisture and the power spectrum of turbulence near the surface can be observed as functions of surface roughness, wind shear, and thermal stratification.

Table 1. Determination of Kármán's constant (κ) based on stress estimates from momentum continuity, and the slope of the logarithmic wind profile, for three controlled wind profile experiments on the ice of Lake Mendota, 1961.

Date	Controlled Parameter	R (m)	S. A. (m^2)	h (cm)	κ
February 19	Roughness fetch (R)	20	2. 0	30	0. 55
		40	2. 0	30	0. 45
		48	2. 0	30	0. 38
February 24	Specific Area (S. A.)	18	3. 0	30	0. 41
		18	1. 5	30	0. 45
		18	0. 8	30	0. 30
		18	0. 4	30	0. 37
March 18	Obstacle height (h)	26	4. 0	30	0. 39
		26	4. 0	60	0. 37

Table 2. Average values of $\underline{Ri}_{113}$ and (Ri)' obtained over the modified and unmodified surfaces, and computed values of the wind profile parameters over the unmodified surface for five controlled wind profile experiments on the ice of Lake Mendota, 1961.

Date	Average over baskets		Average over ice		Wind profile parameters over ice			Condition of surface
	$\underline{Ri}_{113}$ (10^{-3})	(Ri)' (10^{-3}/m)	$\underline{Ri}_{113}$ (10^{-3})	(Ri)' (10^{-3}/m)	z_0 (cm)	d (cm)	V^*/V_{con}	
January 27	8.5	3.7	22.6	8.6	.020	1.05	.111	smooth, traces of ice and wind-blown snow
February 15	5.2	6.0	21.9	26.7	.022	2.95	.100	smooth, ice
February 19	-3.9	-2.5	- 3.8	- 6.2	.013	2.17	.101	smooth, ice
February 24	-3.5	-7.6	-12.5	-17.4	.009	1.92	.097	smooth, ice
March 18	2.3	3.9	7.4	6.6	.073	0.65	.119	irregular, melting snow

Table 3. Roughness field, wind profile, and temperature profile parameters for 20 ten-minute mean runs during five controlled wind profile experiments on the ice of Lake Mendota, 1961.

Date	Controlled Parameter	Roughness Field Parameters*					
		S. A. (m^2)	R (m)	r (m)	ϕ (deg)	ΔR (m)	h (m)
January 27	Specific Area (S. A.)	ice	—	—	—	—	—
		48. 5	80	15	90	5. 0	30
		23. 0	80	15	90	5. 0	30
		11. 7	80	15	90	2. 5	30
February 15	Specific Area (S. A.)	ice	—	—	—	—	—
		14. 7	55	10	60	5. 0	30
		7. 7	55	10	60	2. 5	30
		4. 0	55	10	60	2. 5	30
February 24	Specific Area (S. A.)	ice	—	—	—	—	—
		3. 0	18	3	60	2. 0	30
		1. 5	18	3	60	1. 0	30
		0. 8	18	3	60	1. 0	30
		0. 4	18	3	60	0. 5	30
March 18	Obstacle Height (h)	ice	—	—	—	—	—
		4. 0	26	2	60	2. 5	30
		4. 0	26	2	60	2. 5	60
February 19	Roughness Fetch (R)	ice	—	—	—	—	—
		2. 0	20	4	45	1. 5	30
		2. 0	40	4	45	1. 5	30
		2. 0	48	4	45	1. 5	30

*All listed values are ±5%

ΔR = distance between basket rows

ΔS (not listed) = distance between baskets in each basket row = S. A./ΔR .

Table 3, continued — Temperature profile parameters

Date	$\underline{Ri}_{226}$ (10^{-3})	$\underline{Ri}_{113}$ (10^{-3})	$\underline{Ri}_{56.5}$ (10^{-3})	$\underline{Ri}_{28.2}$ (10^{-3})	$(Ri)'$ (10^{-3}/m)
January 27	7.50	22.60	2.900	3.500	8.60
	5.70	15.50	2.200	2.200	6.00
	6.10	8.70	2.400	0.510	4.20
	2.20	1.30	0.650	-0.250	0.90
February 15	79.40	21.90	9.440	2.610	26.70
	29.40	8.61	4.000	3.260	10.70
	15.70	4.91	1.780	0.509	5.41
	5.79	2.01	0.263	0.271	1.97
February 24	-51.50	-12.60	-6.580	-3.250	-17.40
	-44.10	- 7.30	-2.080	-1.110	-12.90
	-28.10	- 3.63	-1.070	-0.890	- 7.95
	-18.20	- 1.58	-0.345	-0.565	- 4.89
	-17.80	- 1.59	-0.234	-0.466	- 4.74
March 18	12.90	7.46	4.010	3.710	6.63
	11.10	2.99	1.400	2.930	4.35
	8.22	1.41	0.990	4.040	3.46
February 19	-16.00	- 3.81	-1.630	-3.300	- 6.19
	- 4.93	- 3.50	-0.410	-0.350	- 2.17
	- 3.03	- 2.88	-1.710	-0.842	- 1.83
	- 2.16	- 6.92	-4.160	-2.240	- 3.65

Table 3, continued — Wind profile parameters

Date	Wind Direction (deg)	V_{con} (cm/sec)	V^*/V_{con}	d (cm)	z_0 (cm)	E (10^{-4})
January 27	230	616	0.1112	1.05	.0197	.529
	225	634	0.1138	-9.77	.0222	.730
	240	587	0.1239	-8.55	.0465	.815
	235	659	0.1557	-5.22	.2462	.736
February 15	001	453.6	0.1000	2.95	.0221	.653
	001	593.0	0.1209	-6.51	.0896	.210
	007	563.3	0.1336	-9.85	.1703	.787
	006	588.6	0.1655	-19.83	.6061	2.100
February 24	299	501.8	0.0971	1.93	.0087	2.940
	293	486.3	0.1669	-10.33	.5483	3.180
	292	549.8	0.1934	-18.14	1.1980	4.060
	295	571.8	0.2846	-14.05	6.0010	4.080
	299	557.9	0.2520	-24.61	4.0050	11.900
March 18	57	715.0	0.1187	0.65	.0730	1.440
	57	720.7	0.1477	-15.01	.3659	7.650
	47	738.4	0.1744	-35.10	.9323	18.500
February 19	295	430.1	0.1011	2.17	.0133	8.420
	290	462.3	0.1535	-28.38	.3216	9.370
	293	522.8	0.1541	-29.56	.4262	3.430
	292	469.2	0.1801	-16.17	1.2200	2.040

$(d + z_0)$ was computed to a tolerance of 0.001 (see Section 6)

E = sum of squared errors (see Section 6)

Table 4. Hourly observations of sky cover, station pressure, air temperature, wind direction, and wind speed, and computed air densities for five controlled wind profile experiments on the ice of Lake Mendota, 1961.

Date	Hourly Observations		United States Weather Bureau Truax Field, Madison, Wisconsin				
	Hrs (CST)	Sky Cover (Tenths)	Station Pressure (Inches)	Air Temperature (°F)	Wind Direction	Wind Speed (Knots)	Computed Average Air Density ($gm/cm^3 \times 10^{-3}$)
January 27	15	7	29.07	7	SW	14	1.33
	16	8	29.05	4	SW	13	1.33
	17	6	29.04	3	SW	11	1.33
February 15	14	10	29.19	40	NW	12	1.25
	15	10	29.23	37	N	15	1.25
	16	10	29.26	35	N	12	1.25
	17	10	29.29	33	N	11	1.25
	18	10	29.32	32	N	8	1.25
February 24	13	10	28.95	27	W	10	1.27
	14	10	28.94	27	WNW	11	1.27
	15	10	28.94	27	W	10	1.27
	16	10	28.95	27	W	9	1.27
February 24	17	10	28.96	26	WNW	11	1.27
	18	10	28.97	26	NW	10	1.27
March 18	11	10	29.19	32	ENE	15	1.25
	12	10	29.15	33	ENE	13	1.25
	13	10	29.11	33	NE	16	1.25
	14	10	29.11	33	ENE	14	1.25
February 19	15	2	29.30	27	W	13	1.28
	16	4	29.32	25	W	11	1.28
	17	0	29.33	25	WSW	9	1.28
	18	0	29.36	22	W	7	1.28

Table 5. Determination of the geostrophic wind speed ($V_{g,o}$) in m/sec and direction ($\alpha_{g,o}$) in degrees from a regional network of synoptic stations* during five controlled wind profile experiments on the ice of Lake Mendota, Madison, Wisconsin, 1961.

Date	Triangle method		Surface pattern method		Average	
	$V_{g,o}$	$\alpha_{g,o}$	$V_{g,o}$	$\alpha_{g,o}$	$V_{g,o}$	$\alpha_{g,o}$
January 27	23.2	288	23.6	288	23.4	288
February 15	8.7	023	7.4	020	8.0	021
February 19	12.2	300	6.0	294	9.1	297
February 24	11.2	336	9.5	332	10.3	334
March 18	13.3	121	13.8	118	13.5	120

*Hourly station pressures reduced to sea level and wind observations were obtained from a network of synoptic stations within a radius of 200 km of Madison for all experiments. Stations: Green Bay, La Crosse, Lone Rock, Madison, Milwaukee, and Wausau, Wisconsin; Chicago (Midway airport), and Rockford, Illinois; and Dubuque, Iowa.

The hourly observations were averaged over the duration of the experiment and plotted on a surface map. The value of the Coriolis parameter f was taken as 1.0×10^{-4} sec^{-1}. Air density (ρ) was computed from Madison station pressure and temperature (Table 4).

Triangle method. Five pressure triangles were formed between the various synoptic stations such that the Madison station was located within each of the triangles. The horizontal pressure gradient was obtained from the slope of each triangular pressure surface and the values obtained were averaged.

Surface pattern method. A smoothed surface pressure map was drawn and the gradient obtained from the spacing of the surface isobars. It was noted that some stations appeared to differe systematically from the over-all pressure pattern derived from the continental United States Weather Bureau charts. Therefore, a mean map was drawn using all of the hourly observations from the different days. This map had a very flat pressure surface and the systematic differences were easy to identify. Station corrections varying within ± 2 mb were then applied to the individual maps and taken into consideration in the analysis.

Average. The average of the two methods was used in the computation of the Surface Rossby number (Ro_0) and the geostrophic drag coefficient (C).

References

Ellison, T. H.: "Turbulent transport of heat and momentum from an infinite rough plane," Journal of Fluid Mechanics 2, 456, 1957.

Lettau, H. H.: "The present position of selected turbulence problems in the atmospheric boundary layer," Sec. 1.3 of International Symposium on Atmospheric Turbulence in the Boundary Layer (E. W. Hewson, ed.); Geophysical Research Papers No. 19, GRD, AFCRC, Cambridge, Mass., 1952.

Lettau, H. H.: "Computation of Richardson numbers, classification of wind profiles, and determination of roughness parameters," and "Summary of non-dimensional characteristics of boundary layer theory," Sec. 7.4 and 7.5 of Exploring the Atmosphere's First Mile, Vol. 1 (H. H. Lettau and B. Davidson, eds.); Pergamon Press, Inc., New York, 1957.

Lettau, H. H.: "Wind profile, surface stress, and geostrophic drag coefficients in the atmospheric surface layer," in Atmospheric Diffusion and Air Pollution (F. N. Frankel and P. S. Sheppard, eds.), 1958; Vol. 6 of Advances in Geophysics, Academic Press, New York, 1959.

Lettau, H. H.: "Research Problems in Micrometeorology," University of Wisconsin, Department of Meteorology, Final Report, Contract DA-36-039-SC-80063, Madison, Wisconsin, 1959.

Lettau, H. H.: Class notes, Department of Meteorology, University of Wisconsin, 1961.

Moore, W. L.: "An experimental investigation of boundary-layer development along a rough surface," Ph. D. Dissertation, Department of Mechanics and Hydraulics, Graduate College of State University of Iowa, 1951.

Nikuradse, J.: "Stroemungsgesetze in Rauhen Rohren," V. D. I. Forschungsheft, No. 361, 1933.

Paeschke, W.: "Experimentelle Untersuchungen zum Rauhigkeitsund Stabilitatsproblem," Beitr. Phys. fr. Atm., 24, 163, 1937.

Sayre, W. W., and M. L. Albertson: "Roughness spacing in rigid open channels," Journal of the Hydraulics Division, Proceedings of the American Society of Civil Engineers, 87, No. HY3, Part 1, 1961.

Schlichting, H.: "Experimentelle Untersuchungen zum Rauhigkeitsproblem," Ing.-Arch., 7, 1936. English translation in N. A. C. A. Tech. Memo. No. 823, 1937.

Schlichting, H.: Boundary Layer Theory, Pergamon Press, New York, 1955.

Stearns, C. R.: Unpublished report, Department of Meteorology, University of Wisconsin, 1961.

Sutton, O. G.: Micrometeorology, McGraw-Hill, New York, 1953.

Scanner's note:

This page is blank.

8

A Generalized Mathematical Model of the Mean-Velocity Distribution in Fully Turbulent Duct Flow

Heinz H. Lettau

Department of Meteorology
and
Department of Civil Engineering
University of Wisconsin

Abstract. Existing mathematical models of the mean-velocity distribution in fully turbulent duct flow are critically reviewed, in terms of analytical expressions for the length-scale of turbulence (as a function of radial distance from the center of the duct). A new theoretical form for the length-scale of turbulence is proposed which contains no empirical constant in addition to Kármán's constant and which satisfies a principle of similarity between duct flow and atmospheric boundary-layer flow. The resulting universal velocity-distribution in cylindrical ducts, with smooth or rough walls, agrees satisfactorily with the observations reported by Nikuradse and Laufer. It is found that Kármán's constant is a true constant (equal to 0.428) only for fully developed flow in ducts with rough walls. It is suggested that turbulent viscosity is adjusted so that an "effective Reynolds" number is less than a critical value (in the vicinity of 1,000), independent of the actual Reynolds number.

8.1 List of Symbols

8.1.1 Fluid properties, and duct characteristics

ρ = fluid density

ν = kinematic viscosity of the fluid

$2R$ = lateral diameter of the duct

k = average height of the wall-roughness elements

z_0 = aerodynamic roughness-length of the wall

8.1.2 Mathematical symbols, subscripts

$'$ = prime, denoting differentiation with respect to y (or $-x$)

$\bar{}$ = bar, denoting an average across the duct

o = subscript, indicates the value of a quantity at the wall

c = subscript, indicates the value of a quantity at the center

8.1.3 Dimensional variables and flow parameters

r = lateral distance from the center (independent coordinate)

$u = u(r)$ = mean-velocity profile

$U = u_c$ = maximum velocity at the center

$\tau = \tau(r)$ = shearing-stress profile

$u^* = (\tau/\rho)^{\frac{1}{2}} = u^*(r)$ = friction-velocity profile

u_0^* = wall friction-velocity

$L = u^*/(\partial u/\partial r) = L(r)$ = profile of characteristic length-scale of turbulence

8.1.4 Dimensionless duct characteristics, variables, and flow parameters

$Re = 2R\bar{u}/\nu$ = Reynolds number

$y = r/R$ = dimensionless lateral distance from the center

$x = 1 - y$ = dimensionless lateral distance from the wall

$x_0 = z_0/R$ = aerodynamic roughness-parameter of the wall surface

$N = k/z_0$ = Nikuradse's roughness ratio

ε = correction-term function

$\eta = (U-u)/u_0^* = \eta(y)$ = dimensionless velocity-defect profile

$\bar{\eta} = (U-\bar{u})/u_0^*$ = average dimensionless velocity-defect

$C = u_0^*/U = 1/\eta_0$ = wall friction-velocity coefficient

κ = Kármán's numerical constant

$F = L/R = F(y)$ = dimensionless length-scale of turbulence

$f = 4\tau_0/(\rho\bar{u}^2/2)$ = conventional friction-factor

a, c, m, n = numerical constants

8.2 Introduction

The discussion will be restricted to fully turbulent steady mean flow in a straight duct of uniform cross section, with a defined wall roughness. Such conditions are realized for Reynolds numbers larger than approximately 10^4, and distances of at least 40 to 50 diameters from the entry of the duct. For this flow, the lateral distribution of mean velocity will be independent of the down-stream coordinate (i.e., uniformity of flow), and also of the fluid viscosity. For steady mean-flow states, the Navier-Stokes equation reduces to an equality between the lateral gradient of eddy shearing stress and the down-stream pressure gradient which equals a constant for a given experiment. Consequently, the shearing-stress profile must be exactly linear in lateral distance r, with $\tau_C = 0$ at the center; thus

$$\tau = \tau_0 y \; ; \quad \text{or,} \quad u^* = u_0^* \sqrt{y} \; , \tag{1}$$

where τ_0/R is determined by the constant pressure-gradient. Fluid compressibility effects will be neglected.

The velocity profile must satisfy the boundary conditions that, at the center of the duct, u_C equals its maximum value U, while $u_0 = 0$ at the wall. In place of u(r) we can consider the velocity defect U - u, or its dimensionless form $\eta(y)$ with the boundary conditions of $\eta_C = 0$ at the center, and $\eta_0 = U/u_0^*$ = maximum value at the wall.

Let a characteristic length-scale (L) of turbulence be defined with

the aid of the dimensionless equation

$$L/R = F(y) = u^*/u' \quad . \tag{2}$$

Equations (1) and (2) determine uniquely the mean-velocity profile $u(r)$, or $\eta(y)$ in the following relation

$$\eta' = F^{-1}\sqrt{y} \; ; \quad \text{or,} \quad \eta = \int_0^y F^{-1} y^{\frac{1}{2}} dy \quad . \tag{3}$$

The integral in equation (3) can be evaluated when $F(y)$ is a known analytical function of y. It can also be stated that a defined function $F(y)$ must exist if a mean-velocity profile is determined.

Note that only dimensional and purely kinematic arguments are necessary for the definition of L in equation (2). This length L is basically the same as the "mixing length" which was introduced by Prandtl (1925) and expressed independently by Taylor. In the first part of his famous discussion of the "statistical theory of turbulence," Taylor (1935) made the following remarks: "This length could only be defined in relation to the definite but quite erroneous conception that lumps of fluid behave like the molecules of a gas, preserving their identity till some definite point in their path, when they mix with their surroundings and attain the same velocity and other properties as the mean value of the corresponding property in the neighborhood." Although Taylor referred specifically to a Lagrangian discussion, his statements seem to have resulted in a rather widespread discredit and a rejection of the basically Eulerian concept as used in shearing flow. In fact, since equation (2) is purely kinematic, the concept of mixing need not enter. Objections can only be raised against oversimplified interpretation but not against the legitimacy of the kinematic definition of L. As an Eulerian concept the length L is just as realistic and useful as that of mean-velocity for shear-flow in ducts.

In fact, the historical development of the theory of fully turbulent duct flow can be adequately documented by the special explicit functions $F(y)$ used by various investigators. A review of the problem, in terms of F-functions, also establishes the basis for the generalization of the mathematical approach to the mean-velocity distribution proposed in this paper. The fact is important that atmospheric boundary-layer flow is more closely related to duct flow than to flat-plate boundary layer flow, even though the atmospheric fluid is bounded only on the lower side. The physical reason for this statement is that for constant and uniform pressure gradient in the atmosphere the resulting large-scale air flow is steady and horizontally uniform, because the Coriolis force balances exactly the forces due to pressure

and friction. This leads to two-dimensionality of air flow (i.e., significant change of both speed and wind direction with height) in the layer of frictional influence, but the two horizontal components of air motion are horizontally uniform, as in duct flow, and the height of the friction layer is independent of the down-stream coordinate. In experimental flat-plate boundary-layer flow, with or without pressure gradient, the Coriolis force is negligible (with the exception of experiments involving rapid rotation of the boundary), and the friction force is essentially balanced by the inertia force; this leads to a down-stream growth of boundary-layer thickness, and horizontally non-uniform velocity, which makes this flow type significantly dissimilar to atmospheric flow.

Consequently, atmospheric flow resembles duct flow, although only the lower boundary is a material wall. The upper wall, or the duct, is provided by the geostrophic control (i.e., the balance between pressure gradient and Coriolis forces) in the free atmosphere, where the geostrophic wind blows perpendicular to the pressure gradient. The equivalent of the one-dimensional velocity-defect in duct-flow is the two-dimensional "geostrophic departure" in atmospheric boundary-layer flow. With this in mind, some degree of similarity between F-functions for experimental duct flow and atmospheric boundary-layer flow must be expected. In order to apply duct-flow theories to the atmosphere (see Section 9), it is convenient to discuss F as a function of distance from the boundary, i.e., $F(x)$ rather than $F(y)$, considering that $x = 1 - y$. A substitute for the duct-diameter is the height of the "geostrophic wind level" or any related height parameter, for example, the "geostrophic displacement thickness."

The practical value or the success of a theoretic model can only be judged on the basis of a comparison between theoretical and well-established empirical results. Thus far, the geometrical form of the duct was not specified. In view of the fact that the largest amount of empirical data available in the literature concerns turbulent flow in round tubes, let us restrict the discussion to cylindrical ducts of diameter 2R. Readily observed quantities are the wall shear-stress, or u_0^* (from measurements of the pressure head, pipe length and radius), the average velocity $\bar{u}$ (from discharge measurements), and the mean-velocity distribution $u(r)$, including $u_C = U$ (by direct measurement of dynamic pressure at various positions r/R). Most conclusive are comparisons of the dimensionless characteristics such as $\eta(y)$ in place of $u(r)$, including the "bulk" characteristics η_0 and $\bar{\eta}$, i.e., the extreme and the average velocity-defect. The difference $(\eta_0 - \bar{\eta})$ relates the average velocity $\bar{u}$ to the wall shear-stress and, consequently, results in a theoretical expression for the

conventional friction-factor — reference can be made to any textbook of fluid mechanics; see, for example, Rouse and Howe (1953, page 140) —

$$4\tau_0/(\rho\bar{u}^2/2) \equiv f \equiv 8/(\eta_0 - \bar{\eta})^2 \quad . \tag{4}$$

A simpler measure of friction effects is the wall friction-velocity coefficient $C = 1/\eta_0$. By definition,

$$\tau_0 = C^2 \rho U^2 \quad . \tag{5}$$

In equation (5) all conventional but unnecessary numerical factors are avoided. This form is especially useful in atmospheric flow because the velocity U is determined by the geostrophic wind which can be computed with the aid of the horizontal pressure gradient.

In fully turbulent flow the friction-factors f and C are independent of the Reynolds number because the average and the extreme mean-velocity defects are determined only by the wall roughness. It has been well established for cylindrical ducts that f depends solely on the ratio k/R or $z_0 = k/N$ or $x_0 = k/NR$, for fully turbulent states. Nikuradse (1933) has found $N \approx 30$ for sandgrain roughness. Similar results hold true for the atmosphere and the C coefficient. Lettau (1959) has shown that C is a function of a dimensionless combination (of geostrophic speed, Coriolis parameter, and z_0) which is referred to as the "Surface Rossby Number."

With the exception of extremely rough walls in relatively narrow ducts, the order of magnitude of k/R is $1/100$ or less. Consequently, $x_0 \approx k/30R$ is very small in comparison to unity, and terms containing x_0 as a factor can be safely neglected in comparison to both $\ln x_0$ and numbers of the order of unity. This is important for the investigation of the theoretical velocity-defect profiles $\eta(y)$ in the region near the wall. Inasmuch as near the wall the mean velocity tends to go to zero in proportion to $\ln(x/x_0)$, we must consider as the effective duct radius the range from $0 \leq y \leq 1 - x_0$ or $x_0 \leq x \leq 1$. Examples of η_0 values obtained by putting $y = 1 - x_0$ and $\sqrt{y} = 1 - x_0/2$, etc., in various analytical expressions for $\eta(y)$ are presented in the following section.

8.3 Survey of Previous Theories

In a critical survey of existing theories of the mean-velocity distribution of fully turbulent duct flow, it is practical to organize them according to the specific F-functions employed, regardless of whether

or not the original authorities quoted their F-function explicitly. For convenience of comparison, a few of the F-functions discussed here are illustrated in Fig. 1, and the resulting velocity-defect profiles in Fig. 2.

One of the simplest family of analytical forms for F(y) is represented by the "power law,"

$$F = a^{-1} y^m \tag{6a}$$

which, upon combination with equation (3), yields (with exception of $m = 3/2$)

$$\eta = \eta_0 \, y^{(3-2m)/2} \quad ; \quad \text{with} \quad \eta_0 = 2a/(3-2m) \, . \tag{6b}$$

It is historically interesting that one of the oldest known solutions, namely that given more than 100 years ago by Darcy (1858), is of this type, for the special case of $m = 0$ in equations (6). For this assumption F is independent of the distance from the center of the duct, and Darcy's value of the constant $F = 1/a$ was 0.1212. It is readily seen that, if $m > 0$, F increases monotonically from zero at the center to a maximum value at the wall. For $m < 0$, F is smallest at the wall but approaches infinity when y approaches zero. A special case is $m = \frac{1}{2}$ for which the velocity distribution is linear in y. The excluded case, $m = 3/2$, yields η proportional to $\ln y$, which is entirely unrealistic, since empirical data suggest, at least for the region near the wall, proportionality of η to $\ln(1 - y)$, i.e., $\ln x$.

In view of the structure of equation (3) it can be expected that another family of basically simple analytical solutions $\eta(y)$ or $\eta(x)$ is obtained when the F-function is a "modified power law,"

$$F = a^{-1}(1 - y)^m \, y^{\frac{1}{2}} = a^{-1} x^m \, y^{\frac{1}{2}} \quad . \tag{7a}$$

The combination of (7a) with equation (3) yields (with the exception of $m = 1$ which will be discussed later)

$$\eta = \eta_0 (1 - x^{1-m}); \quad \text{or} \quad \eta_0 - \eta \equiv u/u_0^* = \eta_0 x^{1-m} \, , \tag{7b}$$

$$\text{where} \quad \eta_0 = a/(1 - m) \quad .$$

The simple power law of mean-velocity distribution, equation (7b), is still in use as a convenient interpolation formula, normally with an m-value of approximately 6/7, so that the exponent $1 - m$ in equation (7b) is approximately 1/7.

The disadvantage of the power form, equation (7b), is that both constants in equation (7a), the exponent (m) and the factor (a), were found to depend on local conditions. For example, near the wall, m varies with roughness parameter and also with x.

Prandtl (1925, 1932) has shown that most of the discrepancies are removed if one considers the case of $m = 1$ in equation (7a) and the resulting logarithmic distribution of mean velocity, $(\eta_0 - \eta) \sim \ln x$. This is the asymptotic case of the power-form equation (7b) for $1 - m$ approaching zero. Prandtl also showed that for $m = 1$ in equation (7a) the remaining constant is of a universal nature, i. e., independent of the local geometrical and kinematic conditions of the flow type. He demonstrated that this is consistent with the assumption that the "mixing-length" near the wall will increase in direct proportion to the distance from the wall. All this together can be expressed by the requirement that

$$\lim_{y \to 1} (-\partial F/\partial y) = \text{constant} = \kappa \quad , \tag{8}$$

where κ is named Kármán's constant. For both, turbulent flow in pipes and in the atmosphere, the most frequently quoted value in the literature is $\kappa = 0.40$; reference is made to Schlichting (1955); Hinze (1959, page 516) uses $\kappa = 0.41$; and other authorities values which may be somewhere between 0.3 and 0.5.

In view of the uncertainty of the constant, numerical relationships will be derived, as far as possible, without specifying the value of κ. For example, the velocity-defect profile will be quoted numerically as $\kappa\eta$ rather than η. A new appraisal of Kármán's constant will be presented in Section 8.6, and it shall be shown that κ is a true constant only for fully developed flow in rough pipes with a "best" value of $\kappa = 0.428$.

In the author's opinion, it is desirable that the physical nature of this constant be more convincingly demonstrated, and its value established on the basis of first principles. Possibly this can be achieved by assuming a variety of values for κ and showing that a particular value, in the vicinity of 0.4, will lead to minimum conditions in the simultaneous processes of continuous generation and decay of eddy energy.

Discarding the "power laws," equations (6) and (7), we turn to families of F-functions which satisfy equation (8). Among the simplest of such forms are the "linear law,"

$$F = \kappa(1 - y) = \kappa x \quad , \tag{9a}$$

whereupon, in equation (3),

$$\kappa\eta = -2\sqrt{y} + \ln(1 + \sqrt{y}) - \ln(1 - \sqrt{y}) \quad , \tag{9b}$$

with

$$\kappa\eta_0 = -0.6137 - \ln x_0 \quad , \tag{9c}$$

and the "parabolic law,"

$$F = \kappa(1 - y^2)/2 = \kappa x(2 - x)/2 \quad , \tag{10a}$$

whereupon, in equation (3),

$$\kappa\eta = -2\tan^{-1}\sqrt{y} + \ln(1 + \sqrt{y}) - \ln(1 - \sqrt{y}) \, , \tag{10b}$$

with

$$\kappa\eta_0 = -0.1845 - \ln x_0 \quad . \tag{10c}$$

Equation (9a) was first suggested by Prandtl. However, in solving for the mean-velocity profile, Prandtl disregarded the shear-stress variation with r, and discussed the strictly logarithmic profile, which is a correct solution of (3) only if instead of equation (9a) we consider a "modified linear law,"

$$F = \kappa(1 - y)\sqrt{y} = \kappa x\sqrt{1 - x} \quad , \tag{11a}$$

whereupon, in equation (3),

$$\kappa\eta = -\ln(1 - y) \quad \text{with} \quad \kappa\eta_0 = \ln(1/x_0) \quad . \tag{11b,c}$$

Equation (11b) has an extremely simple analytical structure, and gives for the dimensional velocity profile, as a function of the distance from the wall, $u(x) = (u_0^*/\kappa)\ln(x/x_0)$. This purely logarithmic distribution is taken frequently as a standard or reference, in comparison with more complex forms, such as equations (9b) and (10b), or the following theoretical expressions. The difference between actually observed distributions $\kappa\eta_{obs}$ and equation (11b) is sometimes referred to as the "correction-term function;" see, for example, Hinze (1959, page 518). In a revised form, this concept will be discussed and utilized in Section 8.5.

It follows from the above that Prandtl has implicitly introduced a modification of the linear law — i. e., the F-function equation (11a) —

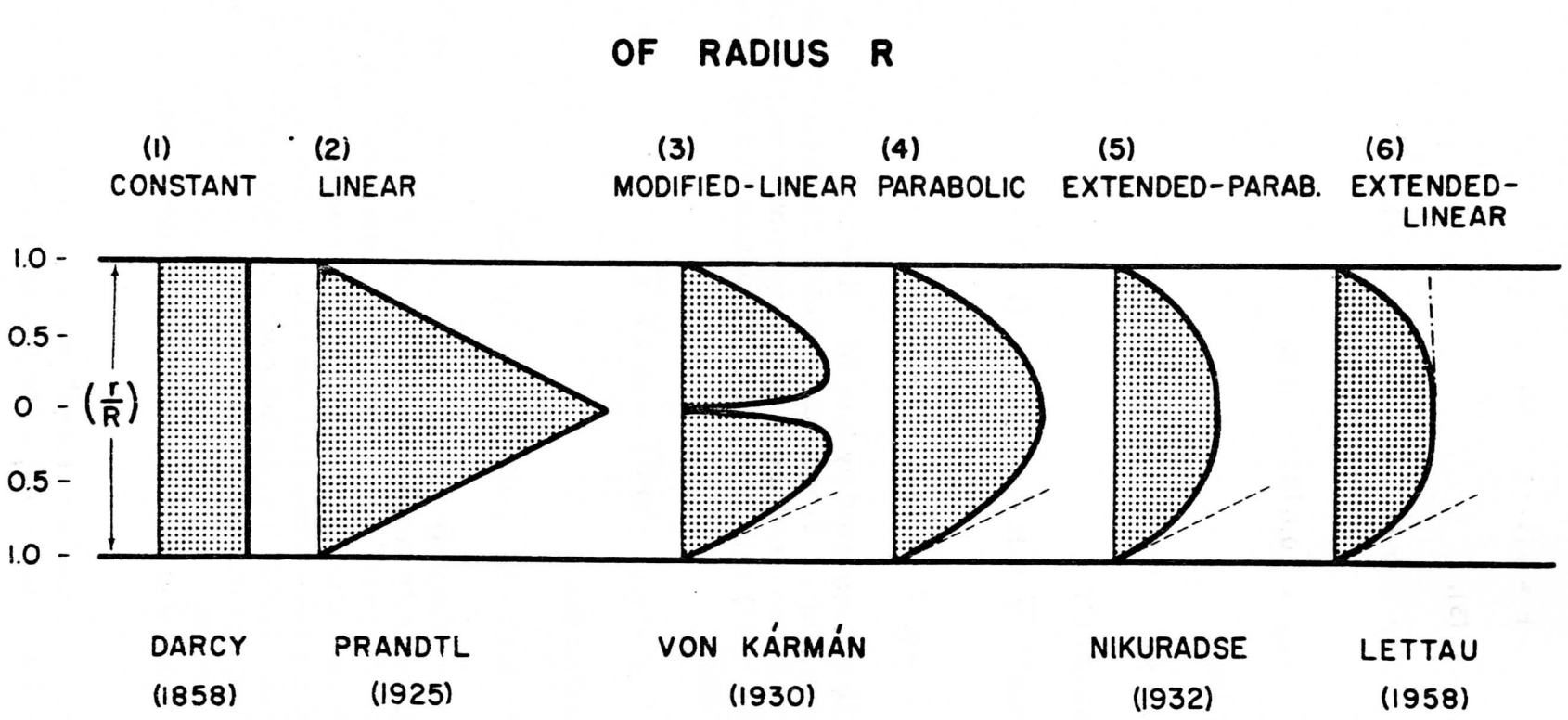

Fig. 1. Schematical illustration of various analytical forms which express the length-scale (F) of turbulence as a function of radial distance in cylindrical ducts. With the exception of F = const in (1), all F's have the same slope in the region close to the wall. The dash-dot line for (6) indicates the shape of F for $1 \leq x < 2$; see the explanation in the text.

on the basis of explicitly quoting only the resulting $\kappa\eta$-function, equation (11b). Kármán (1930) has, also implicitly, introduced another modification of the linear law,

$$F = 2\kappa(1 - \sqrt{y})\sqrt{y} = 2\kappa(1 - \sqrt{1-x})\sqrt{1-x} , \qquad (12a)$$

whereupon, in equation (3),

$$\kappa\eta = -\sqrt{y} - \ln(1 - \sqrt{y}), \text{ with } \kappa\eta_0 = -0.3068 - \ln x_0 . \qquad (12b,c)$$

Kármán's original and explicit starting point was a certain "similarity hypothesis" for the length-scale of turbulence which relates the F-function to the first- and second-order derivatives of the velocity profile in the following equation

$$F = \kappa\eta'/\eta'' . \qquad (12d)$$

Upon differentiation of equation (3)

$$\eta''/\eta' = -F'/F + 1/2y . \qquad (3')$$

When F is given by equation (12a), differentiation with respect to y yields

$$F' = -\kappa + F/2y \quad \text{or} \quad F'/F = -\kappa/F + 1/2y , \qquad (12a')$$

and a combination of equations (12a') with (3') shows that equation (12d) is satisfied. Thus, equation (12a) is necessary and sufficient for satisfying the requirement of Kármán's similarity hypothesis. However, the correction-term function resulting from equations (12b,c) is not in good agreement with reality, as will be demonstrated in Section 8.5. Therefore, the value of Kármán's similarity hypothesis for turbulent shear flow is questionable.

It will also be shown in Section 8.5 that none of the above discussed solutions produces tolerably small and unsystematic correction terms. Inasmuch as the F-functions in the region near the wall are adjusted to satisfy equation (8), the reason for the deficiencies of the theoretical η-distributions must be explained by unrealistic behavior of the F-function in the region near the center of the duct. Exactly at the center — i.e., for $y = 0$ — Kármán's and Prandtl's modified linear laws — i.e., equations (12a) and (11a) — give $F_C = 0$; the parabolic law, equation (10a), gives $F_C = \kappa/2$; in Prandtl's original linear law, equation (9a), $F_C = \kappa$. Empirical data seem to indicate that, in reality, F_C should lie between 0 and $\kappa/2$, or, more specifically, near $\kappa/3$.

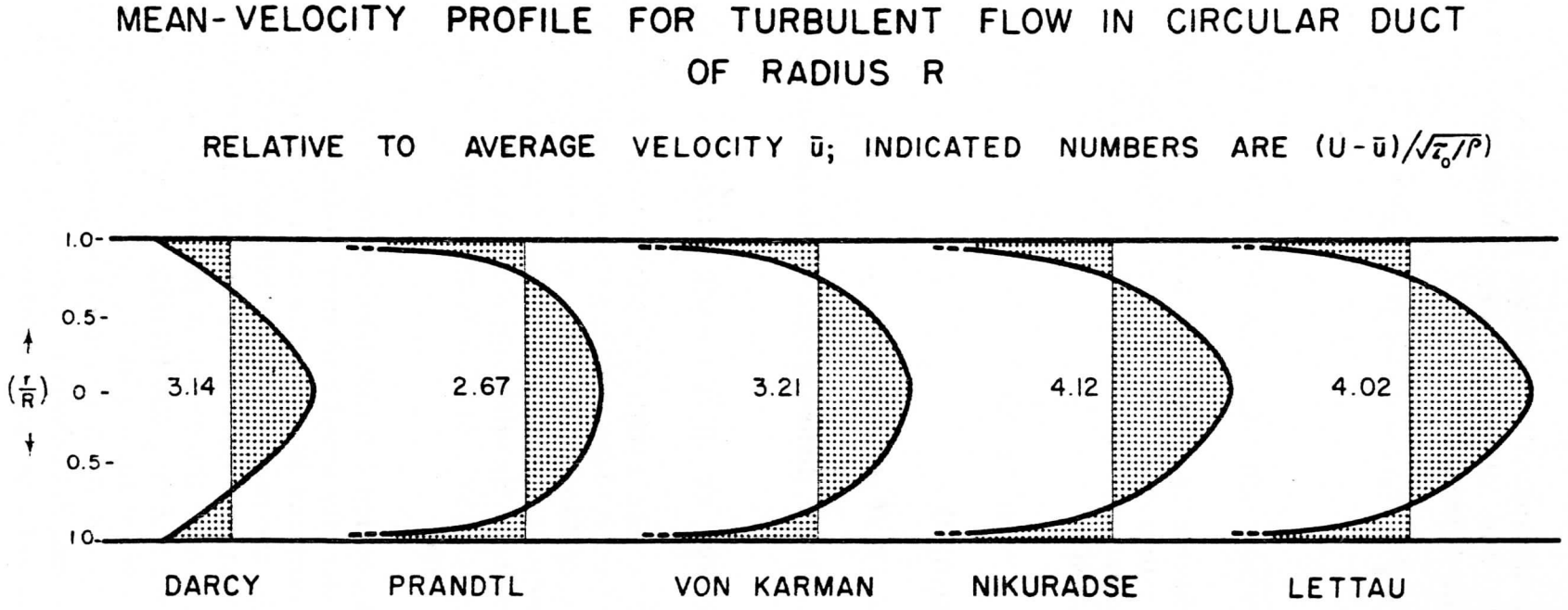

Fig. 2. Schematic illustration of various mean-velocity distributions (as a function of the radial distance from the center of a cylindrical duct) which derive from five of the F-functions illustrated in Fig. 1. The velocity profiles are graphed relative to the average of velocity across the duct. The indicated numbers give the average velocity defect $(U - \bar{u})/\sqrt{\tau_0/\rho}$ computed for a 0.40-value of the Kármán constant.

In 1932, Nikuradse has referred to "an interpolation formula by Prandtl" by introducing what we can call the "extended parabolic law,"

$$F = \frac{\kappa}{2}(1 - y^2)[\,1 - c(1 - y^2)\,] = \frac{\kappa}{2}[\,1 - c - (1 - 2c)y^2 - cy^4\,] \quad . (13a)$$

Equation (13a) satisfies equation (8) for any value of the constant c. Nikuradse suggested the value of $c = 0.3$ so that

$$F_c = \kappa(1 - c)/2 = 0.35\,\kappa \quad .$$

It is convenient to define, as an abbreviation, $c/(1 - c) \equiv a^2$, with $a = 0.6546$ for $c = 0.30$, or $c/(1 - c) = 3/7$. Using a^2 in place of $c/(1 - c)$, we can reformulate equation (13a) as follows

$$\frac{\kappa}{2F} = \frac{1}{1 - y^2} + \frac{c}{1 - c + cy^2} = \frac{1}{1 - y^2} + \frac{a^2}{1 + a^2y^2} \quad , \qquad (13a')$$

whereupon, in equation (3),

$$\kappa\eta = \kappa\eta_{par} + \sqrt{\frac{a}{2}}\,[\ln\frac{1 + ay - \sqrt{2ay}}{1 + ay + \sqrt{2ay}} + 2\tan^{-1}(1 + \sqrt{2ay}) - 2\tan^{-1}(1 - \sqrt{2ay})]\,, \qquad (13b)$$

with

$$\kappa\eta_0 = 0.3046 - \ln x_0 \qquad (13c)$$

where $\kappa\eta_{par}$ is defined by $\kappa\eta$ in equation (10b), i.e., for the parabolic law. The resulting η-distribution, equation (13b) is rather complicated but it is not surprising that it produces relatively small correction terms. However, unless the new constant c in equation (13a) can be justified on the basis of theoretical reasonings, or shown to be of universal nature, equation (13b) must be regarded as a semi-empirical interpolation formula.

8.4 A Generalized Mathematical Model

It has been explained in Section 8.2 that the objective of the generalization is to establish an F-function which, basically, applies to both turbulent duct flow and atmospheric boundary layer flow. The fact that there is no geometrically defined duct diameter in the atmosphere (because only the lower boundary is material) has an important consequence. Namely, it is imperative to utilize the F-function as $F(x)$ rather than $F(y)$, and it is necessary to consider $F(x)$ not only for the limited region $x_0 \leq x \leq 1$ but also for $x > 1$. The physical reason is as follows: even for a perfectly constant horizontal pressure

gradient, the shear-stress distribution in the atmosphere is not a linear function of the lateral distance from the wall. Owing to the Coriolis forces in the atmosphere, the horizontal shearing stress is a vector and changes both intensity and direction with height. Both horizontal components of the shearing stress asymptotically approach zero at considerable height, in relation to the vertical changes of the two horizontal components of wind shear. It is natural to assume that the length-scale of turbulence can be defined in atmospheric boundary-layer flow, and that it is independent of the orientation of a horizontal reference-frame of coordinates. By virtue of its concept, F would then be the same for the two horizontal components and only positive F-values can have physical reality, for any $x > 0$.

In view of these requirements, Prandtl's and Kármán's modified linear laws — equations (11a) and (12a) — must be discarded because both result in imaginary F-values when $x > 1$. The parabolic law — equation (10a) — and Nikuradse's extended parabolic law — equation (13a) — are eliminated because both result in negative F-values for $x > 2$. The only F-function in Section 8.2 which is positive for any value of x is equation (9a), $F = \kappa x$, Prandtl's original linear law. However, the resulting η-distribution was not satisfactory for duct flow. For the atmosphere, an ever-increasing scale of turbulence with height is unlikely, and not suggested by observational experience.

Rossby (1932) has modified Kármán's similarity hypothesis in an attempt to apply it to atmospheric and oceanic turbulence. He found that the length-scale of turbulence should increase with approach towards the boundary, which is exactly the opposite of Prandtl's concept. In patching together the two solutions, i.e., by assigning Prandtl's form to the lowest part, and Rossby's form to the upper and larger part of the atmospheric boundary-layer, Rossby and Montgomery (1935) succeeded in explaining several features of actual wind profiles. However, their solution is unsatisfactory owing to lack of continuity in the composite solution, as well as a certain arbitrariness in the individual solutions.

To a certain degree one could draw a parallel to the state of knowledge concerning the laws of black-body radiation at the end of the last century. Two different asymptotic expressions were derived originally from classical physics. For small wave-length Wien's radiation law gave an increase of intensity with wave-length. For large wave-length, the Rayleigh-Jeans law of radiation gave a decrease of intensity with wave-length. It was Planck's great achievement to conceive the universal law which contained the two previously known solutions as asymptotic cases.

Unfortunately, in contrast to classical physics, conditions of turbulence structure are still only poorly understood. We are restricted to more or less heuristic accounts of the problem. It can be concluded that the immediate problem is to generalize the approach indicated by Rossby and Montgomery.

The search for a universal similarity principle and a subsequent F-function which is applicable to both turbulent duct flow and atmospheric boundary layer flow, has led — Lettau (1958) — to another extension of Prandtl's basic linear law, which may be referred to as the "extended linear law," or the "linear-hyperbolic law,"

$$F = \varkappa(1 - y)/[\,1 + m(1 - y)^{1+1/m}] = \kappa x/(1 + m x^{1+1/m}) \,, \qquad (14)$$

which, when differentiated once with respect to x, gives

$$\partial F / \partial x = F(1 - x^{1+1/m})/x(1 + m\, x^{1+1/m}) \,. \qquad (14')$$

It can be readily verified that equation (8) is satisfied for any value of m. F reaches its maximum value, for any m, at $x = 1$, i.e., $(y = 0)$, and approaches monotonically zero for increasing x, but always $F > 0$ for $0 \leq x < \infty$.

Equation (14) contains only one additional number (m) in addition to the universal constant $\varkappa$. Comparison with observational findings suggests that m equals 2 for the one-dimensional duct-flow while m equals 4 for the two-dimensional atmospheric boundary flow. The fact is highly significant that the parameter m seems to be determined by the flow structure. It means that there remains no arbitrary or empirical constant in equation (14). For an illustration of the two F-functions see Fig. 3. Thus, for duct flow,

$$F = \kappa(1 - y)/[1 + 2(1 - y)^{\frac{3}{2}}] = \kappa x/(1 + 2x^{\frac{3}{2}}) \,, \qquad (15a)$$

whereupon, in equation (3),

$$\kappa\eta = \ln \frac{1 + \sqrt{y}}{1 - \sqrt{y}} - 2\sqrt{y} + (y - \tfrac{1}{2})\sqrt{y - y^2} + \tfrac{1}{2} \sin^{-1}\sqrt{y} \,, \qquad (15b)$$

with

$$\kappa\eta_0 = 0.2210 - \ln x_0 \,. \qquad (15c)$$

For the region of duct flow, $0 \leq y \leq 1 - x_0$, the F's in equations (15a) and (13a) are very similar to each other. They are identical close to the wall; at the center, equation (15a) yields $F_C = \kappa/3 = 0.333\kappa$,

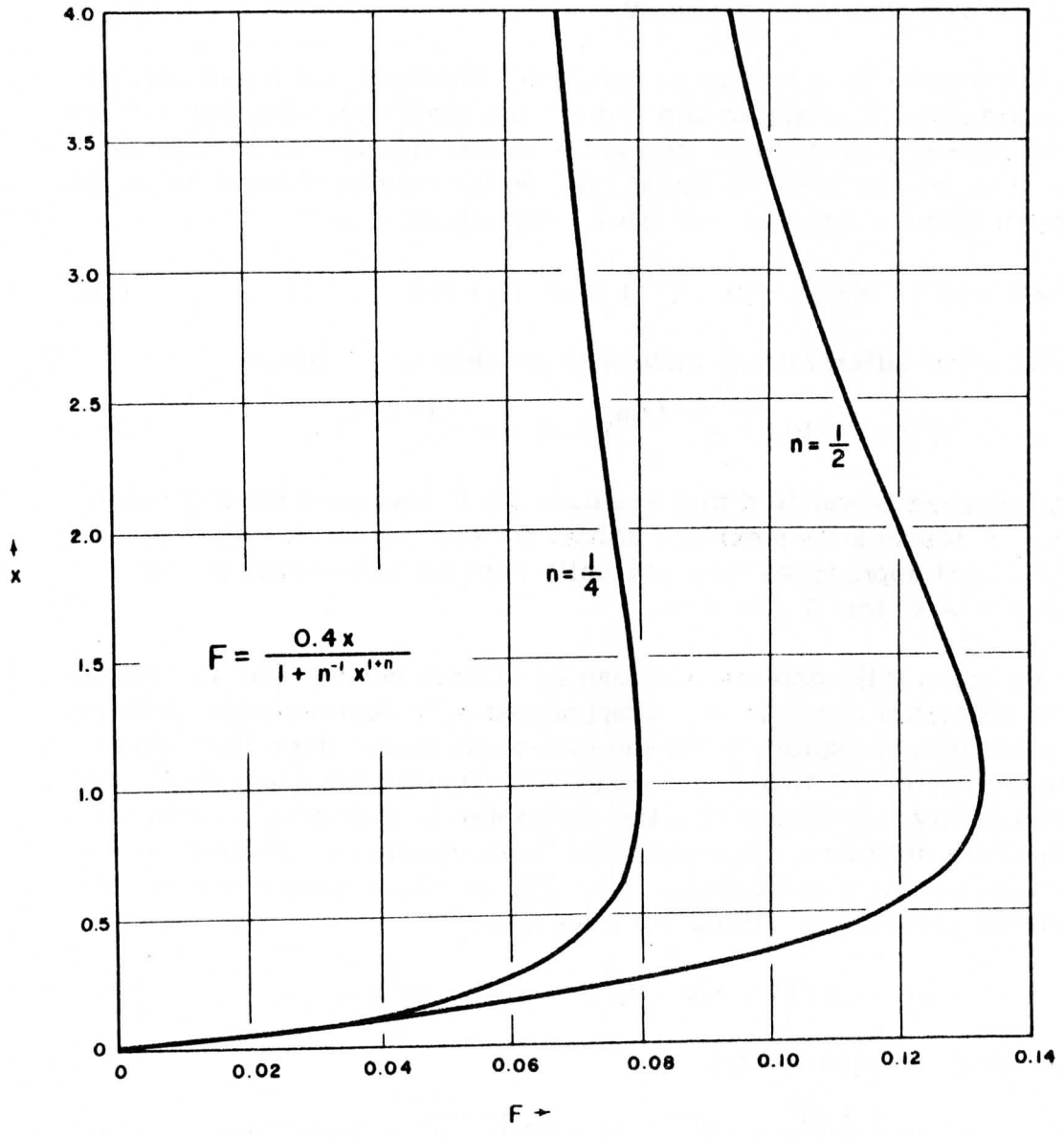

Fig. 3. The non-dimensional length-scale (F) of turbulence as a function of the non-dimensional distance (x) from the boundary. Note that the parameter m as defined in the text equals $1/n$ in this graph. For duct flow, n equals $\frac{1}{2}$ (or $m = 2$) and $0 \leq x \leq 1$. For the two-dimensional atmospheric boundary layer flow n equals $\frac{1}{4}$ (or $m = 4$).

which is within 5% of Nikuradse's F-value for $y = 0$, $F_c = 0.35\kappa$. This agreement is certainly within permissible limits of the empirical determination of Nikuradse's constant c.

A consequence of the similarity of the two F-functions in the region $0 \leq y \leq 1$ is that the resulting η-distributions agree closely with each other. However, the mathematical structure of equation (15b) is obviously less complicated than that of equation (13b). For an illustration, see Fig. 2, and for numerical comparisons see Section 8.5.

A summary of the various F-functions discussed is represented in Fig. 1. It can be assumed that those F-curves which show sharp corners or other discontinuities are less realistic than those with rounded forms. Among the latter group the F-function given by equation (15a) is unique in that it contains no empirical constant, and satisfies an important similarity principle relating duct flow and atmospheric boundary layer flow.

8.5 Average Velocity Defect, and Comparison with Observations

The average of the velocity defect over the cross-section in a cylindrical duct is

$$\bar{\eta} = \int_0^{1-x_0} \eta \, d y^2 \quad . \tag{16}$$

Due to $x_0 \ll 1$, the integration can be performed between the limits of zero and one. In order to facilitate the integration let us consider the following transformations

$$\eta \, d y^2 = d(\eta y^2) - y^2 d\eta = d[\eta(y^2 - 1)] + (1 - y^2) d\eta \, . \tag{17}$$

Now, consider that $d\eta = \eta' dy$, whereupon, with the aid of equation (3),

$$\kappa \bar{\eta} = \kappa[\eta(y^2 - 1)]_0^1 + \int_0^1 \kappa(1 - y^2) y^{\frac{1}{2}} F^{-1} dy \quad . \tag{18}$$

The first member on the right-hand side of equation (18) is zero, because of $\eta = 0$ for $y = 0$. The second term can be readily evaluated for the F-functions given by equations (9a, 10a, 11a, 12a, 13a, and 15a). The resulting numerical constants obtained for $\kappa\bar{\eta}$ are summarized in the following listings; for comparison, the numerical constants $(\kappa\eta_0 + \ln x_0)$ from equations (9c, 10c, 11c, 12c, 13c, and 15c) are also included.

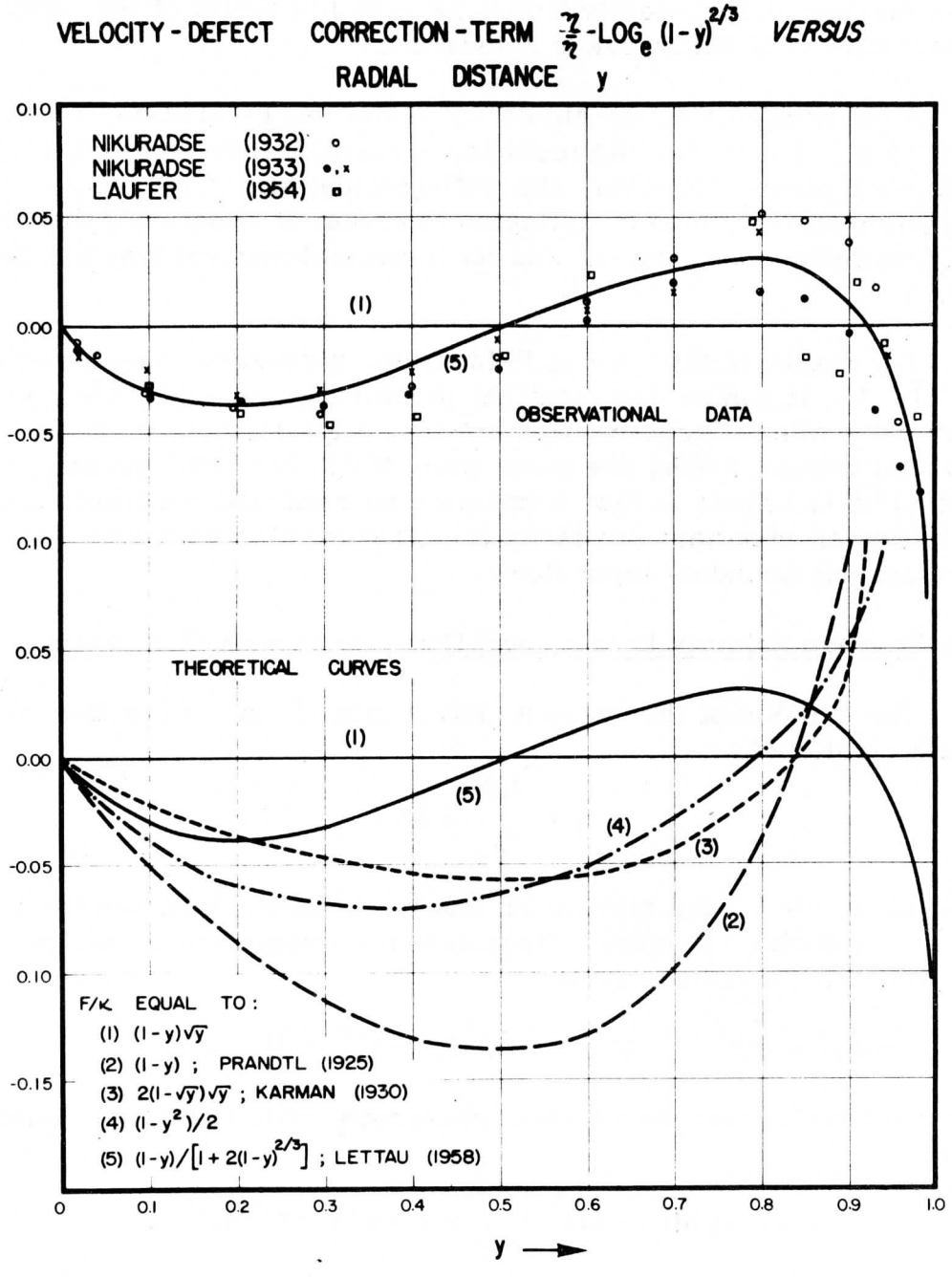

Fig. 4. Observed and theoretical variation of the normalized velocity-defect correction term ($\varepsilon = (\eta/\bar{\eta}) - \ln(1-y)^{2/3}$) as a function of the non-dimensional distance (y) from the center of a cylindrical duct.

For F in equation

(9a)	$\kappa\bar{\eta} = 16/15 = 1.067$;	$\kappa\eta_0 + \ln x_0$	$= -0.614$
(10a)	" $= 4/3 = 1.333$;	"	$= -0.184$
(11a)	" $= 3/2 = 1.500$;	"	$= 0.000$
(12a)	" $= 77/60 = 1.283$;	"	$= -0.307$
(13a)	" $= 1.647$;	"	$= 0.305$
(15a)	" $= 1.607$;	"	$= 0.221$

Darcy's power law, i. e., $m = 0$ in equation (6a) yields $\bar{\eta} = 8a/21 = 3.14$. It is significant that the ratio $\kappa\eta/(\kappa\bar{\eta}) = \eta/\bar{\eta}$ is independent of the particular value of the Kármán constant κ, and that all theoretical η-distributions are essentially logarithmic in $(1 - y)$. Therefore, it is practical to take the logarithmic velocity-defect distribution, i. e., equation (11b) and the resulting $\kappa\bar{\eta} = 3/2$, as a standard or reference distribution.

Let us define a "normalized correction-term function" in the following equation

$$\varepsilon = \frac{\eta}{\bar{\eta}} - \ln(1 - y)^{\frac{2}{3}} \quad . \tag{19}$$

The average value across the duct, $\bar{\varepsilon}$, equals zero. Fig. 4 illustrates observed and theoretical ε-distributions as a function of the non-dimensional distance from the center of the duct. The observational distributions were obtained from data presented by Nikuradse (1932, 1933) and Laufer (1954). They agree with each other within tolerable error limits although the measurements were made for quite different flow conditions. Nikuradse investigated flow of water in smooth and rough pipes, and Laufer the flow of air in a smooth tube. The theoretical ε-distributions show characteristic differences, especially in their behavior at y-values close to one, i. e., near the wall. This is explained by differences in the values of the numerical constant (additional to $\ln x_0$) in the equations for $\kappa\eta_0$ which were found in Section 4 and are summarized in the above listings.

An objective measure of the agreement between observed and theoretical velocity distribution is given by the sum, or average of the deviation squares $(\varepsilon_{obs} - \varepsilon_{theor})^2$. Inspection of Fig. 4 shows that the ε-distribution based on the extended linear F law — i. e., F as given by equation (15a) — evidently produces the least sum of deviation squares. A similar statement is true for F given by the extended

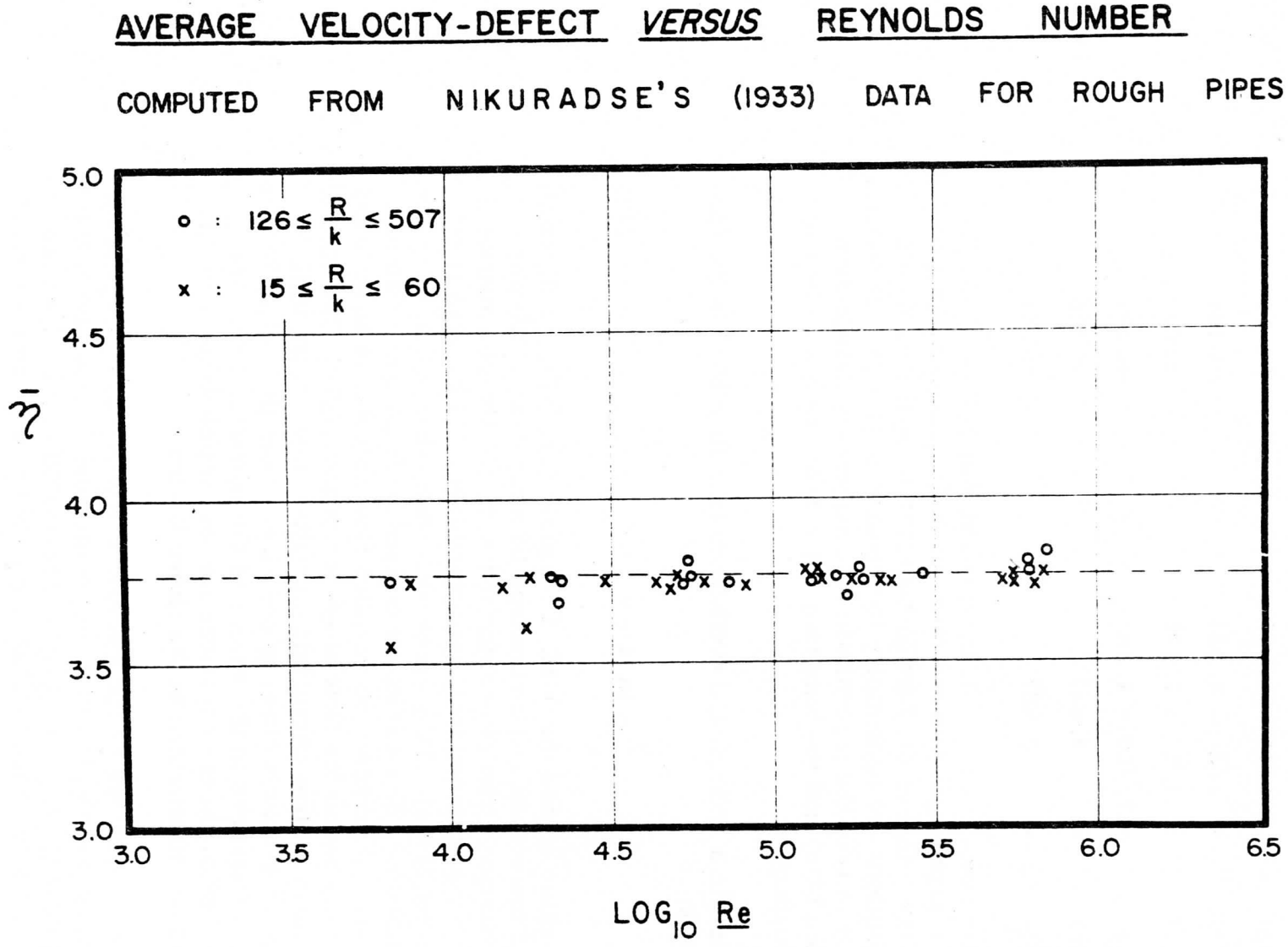

Fig. 5. Average velocity-defect in cylindrical ducts with defined wall-roughness (R/k) as a function of the Reynolds number, recomputed from empirical data tabulated by Nikuradse (1933).

parabolic law, equation (13a), which is not shown in Fig. 4 because it is inherently an interpolation formula.

It can be concluded that a universal velocity-distribution applies to turbulent flow in smooth as well as rough ducts, and that an engineering approximation to such flows is obtained by equation (15b), i. e., the proposed generalization of the mathematical expression for the kinematic length-scale of turbulence, as a "linear-hyperbolic" function of the distance from the wall.

8.6 Kármán's Constant, and Relationship between Geometric and Aerodynamic Wall-Roughness

The existence of a universal velocity distribution implies that $\kappa\bar{\eta}$ is a universal constant. From the discussion in Section 8.5 it was concluded that the best value for this constant is $\kappa\bar{\eta} = 1.607$. If this is accepted it follows logically that κ will be a universal constant only when $\bar{\eta}$ is independent of flow conditions. This can only be tested with the aid of empirical data.

Fig. 5 is based on Nikuradse's (1933) investigation of water flow in rough pipes. The data show indeed that, within tolerable error limits, $\bar{\eta}$ varies neither with the Reynolds number nor wall roughness. Nikuradse gave $\bar{\eta} = 3.75$, and a recalculation confirmed this value, $\bar{\eta} = 3.754$. Consequently, for the new form of the universal velocity distribution, equation (15b), the value of Kármán's constant for fully turbulent flow is

$$\kappa = 1.607 / 3.754 = 0.428 \quad . \tag{20}$$

The most frequently used value of $\kappa = 0.40$ would be true when the universal velocity distribution is assumed to be logarithmic, i. e., $\kappa\bar{\eta} = 3/2$ and $\bar{\eta} = 3.75 = 15/4$. However, in view of the facts illustrated in Fig. 4, there is no justification for the hypothesis that the universal velocity law is best represented by the simple logarithmic form, equation (11b). The use of $\kappa = 0.4$ is legitimate only in connection with the logarithmic distribution, equation (11b), and will lead to error when used with real data.

Because Fig. 4 suggests a rather universal validity of the same velocity-distribution law, it is interesting to discuss, briefly, turbulent flow in ducts with smooth walls. Fig. 6 is based on Nikuradse's (1932) investigations of water flow in smooth pipes. From his tabulations of Re, $\log_{10}(1/\sqrt{f})$, and $\bar{u}/U$ — considering that $(\eta_0 - \bar{\eta}) = \sqrt{8/f}$, and $\bar{u}/U = (\eta_0 - \bar{\eta})/\eta_0$ — a total of 125 values of $\bar{\eta}$ were recomputed

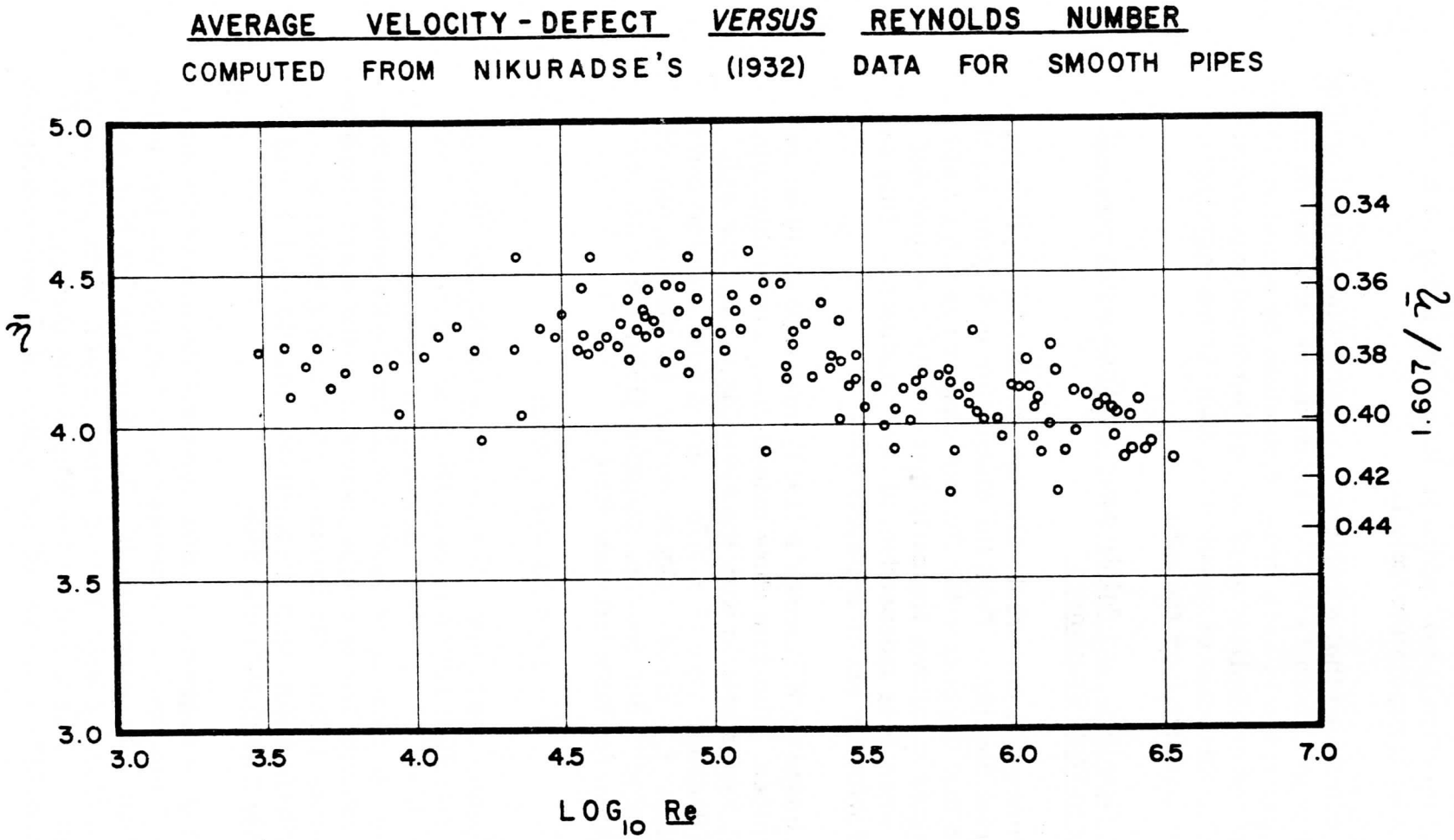

Fig. 6. Average velocity defect in cylindrical ducts with smooth walls as a function of the Reynolds number, recomputed from empirical data tabulated by Nikuradse (1932). The scale at the right-hand margin indicates the value of the Kármán constant for the universal velocity-distribution derived from the extended linear F-law.

and plotted in Fig. 6. Another careful evaluation of $\bar{\eta}$ with the aid of Laufer's (1954) graphically presented $\bar{u}/U$-data, for air flow at Re = 428,000 resulted in $\bar{\eta} = 4.10$, while $\eta_0 = 28.4$. Laufer's $\bar{\eta}$ agrees satisfactorily with Nikuradse's data for this region of Reynolds number.

The $\bar{\eta}$-values for smooth tubes are significantly larger than $\bar{\eta} = 3.75$ which was found for flow in rough pipes. Furthermore, in contrast to Fig. 5, the data on Fig. 6 indicate that $\bar{\eta}$ for smooth pipes displays a relatively weak but significant variation with Reynolds number. The 3.75 value for rough pipe seems to be asymptotically approached at extremely high Reynolds number.

This behavior of $\bar{\eta}$ must of necessity mean that in smooth-duct turbulence the Kármán constant does vary systematically with the Reynolds number and, therefore, κ is not a universal constant. The possible range of κ is between 0.35 and 0.42. Its relationship to Re can be estimated with the aid of the scale on the right-hand margin of Fig. 6 if equation (15b) is taken as the universal velocity distribution law.

Returning now to fully developed turbulent flow in rough pipes, let us re-analyze the relationship between geometric and aerodynamic measures of the wall roughness with the aid of the new velocity-distribution law. Nikuradse has derived the empirical relation

$$\eta_0 = 8.48 + 5.75 \log_{10}(R/k) = 8.48 + 2.5 \ln(R/k) . \qquad (21)$$

Since Nikuradse assumed that $\kappa = 0.40$, equation (21) can be reformulated as

$$\kappa\eta_0 = 3.392 + \ln(R/k) = \ln(29.7\,R/k) \qquad (22)$$

The empirical equation (22) was compared with the theoretical relationship equation (11c), i. e., assuming that the universal velocity distribution is actually given by equation (11b); hence,

$$\kappa\eta_0 = \ln(1/x_0) = \ln(NR/k) , \qquad (11c)$$

whereupon the value of Nikuradse's number N was obtained as $N = 29.7 \approx 30$.

If equation (15b) is taken as the best representative of the universal velocity distribution law, the empirical equation (22) must be compared with the subsequent theoretical relation

$$\kappa\eta_0 = 0.2210 + \ln(1 - x_0) = \ln(1.246/x_0) , \qquad (15c)$$

whereupon it follows that the value of Nikuradse's number is

$$N = 29.7/1.246 = 23.9 \approx 24 . \qquad (23a)$$

This establishes the non-dimensional relationship between the geometrical and the aerodynamic measure of wall roughness,

$$z_0 = k/N = k/23.9 , \qquad (23b)$$

for the new mathematical model of the universal velocity-distribution law in fully turbulent flow in rough ducts.

With the aid of equations (4) and (5),

$$f = 8/[-3.23 + 5.38 \log_{10}(R/24k)]^2 , \qquad (24)$$

$$C^{-1} = \eta_0 \approx 5.38 \log_{10}(R/24k) . \qquad (25)$$

The last two equations can be used to estimate the conventional pipe-friction factor f and the wall friction-velocity coefficient C for the new velocity law.

8.7 Turbulent Viscosity and Effective Reynolds Number

The turbulent viscosity ν_T is defined as the quotient of actual shearing stress (or τ/ρ) and rate of shear, $\partial u/\partial r$. It follows from equations (1) and (2) that ν_T must be a function of the radial distance r from the center, and that a non-dimensional form of this function is obtained as

$$\nu_T/Ru_0^* = F\sqrt{y} . \qquad (26)$$

For any of the F-functions discussed in Sections 8.3 and 8.4, ν_T is relatively small not only at the wall but also at the center, and reaches a maximum value in between. Let us consider the average over the cross-section of a cylindrical duct,

$$\bar{\nu}_T/Ru_0^* = \int_0^1 F\sqrt{y}\, dy^2 = 2\int_0^1 F y^{\frac{3}{2}}\, dy . \qquad (27)$$

For the purpose of the following discussion it is sufficiently accurate to approximate the universal velocity distribution by the logarithmic law, i.e., $F = \kappa(1 - y)\sqrt{y}$ and, consequently, $\kappa = 0.40$.

Then, the turbulent viscosity ν_T in equation (26) is proportional to $y(1 - y)$ which equals $(1 - x)x$. The symmetry of this form indicates that ν_T reaches its maximum value exactly at mid-radius, where $x = \frac{1}{2} = y$. Hence, in equation (27),

$$\bar{\nu}_T = R u_0^* \, 2\kappa/12 = R u_0^*/15 \quad . \tag{28}$$

When F is expressed by Darcy's equation (6a) for $m = 1$, the numerical factor in equation (28) would be $3a/2 \approx 1/12.4$ instead of $1/15$. It has been pointed out by several investigators — for example, Corrsin (1957) — that it can be interesting to utilize a suitably defined turbulent viscosity for the definition of an effective Reynolds number Re_{eff}. In order to preserve its characteristic as a bulk modulus, let us consider

$$Re_{eff} = 2R\bar{u}/\bar{\nu}_T = Re\, \nu/\bar{\nu}_T \quad . \tag{29}$$

With the aid of equation (28), and remembering that $\bar{u}/u_0^* = \eta_0 - \bar{\eta}$, equation (29) yields

$$Re_{eff} = 30\bar{u}/u_0^* = 30(\eta_0 - \bar{\eta}) \quad . \tag{30}$$

Fully developed turbulent flow requires that the actual Reynolds number must be in excess of at least 10,000, but the effective Reynolds number as defined by equation (30) will be less than 1,000 which is considered to be the order of a critical value. For example, in Laufer's experiment mentioned in Section 8.5 and 8.6, $\eta_0 = 28.4$, and $\bar{\eta} = 4.10$, so that $Re_{eff} = 729$, while $Re = 428{,}000$.

For ducts with significant wall roughness $\bar{\eta}$ equals 3.75 which is a truly universal constant. Then, the magnitude of Re_{eff} is uniquely determined by the value of η_0. Equation (30) shows that Re_{eff} is below 1,000 when

$$\eta_0 < (3.33 + \bar{\eta}) \approx 37 = 14.8/0.4 \tag{31a}$$

From the results discussed in Section 6, we substitute $\ln(1/x_0)$ for $\kappa\eta_0$, with $\kappa = 0.40$, and $x_0 = k/30R$, whereupon

$$\ln(1/x_0) < 14.8 \approx \ln(3.10^6) \tag{31b}$$

or

$$1/30x_0 = (R/k) < 1.0 \times 10^5 \quad . \tag{31c}$$

The physical meaning of the last inequality can be interpreted as follows. Fully turbulent flow can possibly produce $Re_{eff} < 1{,}000$ only

when k/R is larger than 10^5. This seems indeed to be a reasonably close approximation to the practical limit for which wall roughness has been found significant; reference can be made to any textbook of basic fluid mechanics — for example, Rouse and Howe (1953).

When the walls of the duct must be considered "smooth" the effective Reynolds number in equation (30) will remain below a critical value of approximately 1,000 if $\bar{\eta}$ is larger than 3.75. This is actually the case as was shown in Section 8.5. Perhaps it is worthwhile to investigate these relationships more thoroughly. It appears possible that the success of a turbulent viscosity is not as superficial as it has been often assumed.

8.8 Conclusion

This paper is intended to be primarily a heuristic account of the specific problem of mean-velocity distribution in fully turbulent flow. A generalization of a similarity principle is introduced and it can be concluded that certain aspects of the proposed new mathematical expression for the mean length-scale of turbulence merit closer investigation. It is perhaps possible that certain parallels to developments in classical physics, mentioned in Section 8.4, are physically meaningful. The structure of the suggested F-function (see Fig. 3) and the interpretation of its characteristic parameter (m) as indicating the "degrees of freedom" (or the number of dimensions) makes it similar to the structure of probability functions — for example, the Maxwell distribution of molecular speeds. This feature can help to consolidate the dual picture of turbulence, in building a bridge between the engineering concepts (which are deterministic, and based on bulk parameters and mean-flow properties) and the theoretician's concepts (which are quantum-mechanistic and based on turbulence structure, statistical parameters, and spectra).

Aside from these philosophical aspects there are several questions which are capable of more direct answers. For example, a detailed study of wind profiles in the atmospheric boundary layer, in terms of the generalized similarity principle and the subsequent F-function, has been completed and is discussed in Section 9. Also under way are investigations of the structure of shear flow in flat-plate boundary layers.

References

Corrsin, S.: "Some Current Problems in Turbulent Shear Flows," Chapter XV in Naval Hydrodynamics, Publ. 515, Nat. Acad. Sciences, Nat. Res. Council; Washington, D. C., 1957.

Darcy, H.: "Recherches Experimentales Relative Au Mouvement de l'Eau dans les Tuyaus," Mem. Acad. Science Inst. Imp. France, 15, 141, 1858.

Hinze, J. O.: Turbulence. McGraw-Hill Book Company, Inc., New York, Toronto, London, 1959.

von Kármán, T.: "Mechanische Aehnlichkeit und Turbulenz," Nachr. Ges. Wiss., Goettingen, Math.-Phys. Kl., 58, 1930.

Laufer, J.: "The Structure of Turbulence in Fully Developed Pipe Flow," Nat. Advis. Comm. Aeronaut., Tech. Rep. No. 1174, 1954.

Lettau, H.: "A Unified Theory for Turbulent Flow in Conduits and in the Atmosphere," unpublished paper, presented December 1958, Hydraul. Seminar, U. of Wisconsin; also March 1959, "Civ. Eng. Lecture," Purdue University, Lafayette, Ind.

Lettau, H.: "Wind Profile, Surface Stress, and Geostrophic Drag Coefficients in the Atmospheric Surface Layer," in Atmospheric Diffusion and Air Pollution (F. N. Frenkiel and P. S. Sheppard, eds.), Vol. 6 of "Advances in Geophysics," Academic Press, New York and London, 1959.

Nikuradse, J.: "Gesetzmaessigkeiten der Turbulenten Stroemung in Glatten Rohren," V. D. I. Forschungsheft, No. 356, 1932.

Nikuradse, J.: "Stroemungsgesetze in Rauhen Rohren," V. D. I. Forschungsheft, No. 361, 1933.

Prandtl, L.: "Bericht ueber Untersuchungen zur Ausgebildeten Turbulenz," Z. Angew. Math. Mech., 5, 136, 1925.

Prandtl, L.: "Meteorologische Anwendung der Stroemungslehre," Beitr. Phys. d. Atmosph., 19, 188, 1932.

Rossby, C. G., and R. B. Montgomery: "The Layer of Frictional Influence in Wind and Ocean Currents," Mass. Inst. Techn., Meteorol. Papers, 3, No. 3, 1935.

Rouse, H., and J. W. Howe: Basic Mechanics of Fluids. John Wiley and Sons, New York, 1953.

Schlichting, H.: Boundary Layer Theory. Pergamon Press, London, 1955.

Taylor, G. I.: "Statistical Theory of Turbulence, Part I," Proc. Roy. Soc., London, A91, 421, 1925.

9

Theoretical Wind Spirals in the Boundary Layer of a Barotropic Atmosphere

Heinz H. Lettau

Department of Meteorology
University of Wisconsin

Abstract. A new theoretical form for the length-scale of turbulence as a function of distance from the lower boundary is proposed which contains no empirical constant other than Kármán's constant. An integration of the equation of motion with height-dependent friction-velocity is performed. The resulting universal wind-spiral solution for the atmospheric boundary layer is tabulated. It can be verified for given sets of V_g = geostrophic wind, f = Coriolis parameter, and z_0 = aerodynamic roughness parameter of the ground surface. The solution is completed with the analytical formulation of various coefficients (geostrophic drag coefficient, unit-height coefficient, etc.) as unique-valued functions of the surface-Rossby number $Ro_0 = V_g/z_0 f$. In the atmospheric surface layer the solution is equal to the conventional logarithmic wind profile. Computed wind spirals compare satisfactorily with observed wind spirals for the boundary layer of an adiabatic atmosphere. Agreement is also found between computed and empirical surface-stress relationships. Applications of the theory in estimating the dissipation of energy in the lower troposphere are discussed.

9.1 Introduction

The discussion is restricted to cases of steady and horizontally uniform large-scale air motion above level terrain of uniform and defined surface roughness. At any point in the lower troposphere a perfect balance between the pressure gradient force, the Coriolis force, and the friction force is assumed. This excludes inertia forces, and vertical components of the mean air motion. The resulting mean

wind is a strictly horizontal vector ($\vec{V}$) independent of horizontal coordinates, but possibly changing direction and intensity from level to level. Furthermore barotropy is assumed, i. e. the air density ρ is a unique-valued function of atmospheric pressure. This excludes "thermal winds" so that the geostrophic wind ($\vec{V}_g$) is independent of height.

An atmospheric boundary layer will exist in which the wind increases with height from the boundary condition of $V_0 = 0$ at the surface ($z = 0$) asymptotically approaching the geostrophic wind at sufficiently large distance from the ground ($z \geq H$). In comparison with the height of the atmosphere (or the tropopause), the thickness (H) of the atmospheric boundary layer is sufficiently small to justify the neglecting of vertical density differences; this implies that terms like $\vec{V}\,\partial\rho/\partial z$ are small in comparison with $\rho\,\partial\vec{V}/\partial z$ and can be disregarded in the boundary layer.

When f = Coriolis parameter and $\vec{\tau}$ = vector of shearing stress at height z, the equation of motion reduces for the above formulated assumptions to

$$\rho f i(\vec{V} - \vec{V}_g) = \partial\vec{\tau}/\partial z \quad , \tag{1}$$

where complex vector notation is used, $i = \sqrt{-1}$. It is assumed that the vector of shearing stress is horizontal and at any level proportional to the vector of shear ($\partial\vec{V}/\partial z$). Then the factor of proportionality is a scalar quantity (function of height) which defines the effective dynamic viscosity (ρK). K is referred to as the eddy viscosity or diffusivity. When $\partial\vec{V}_g/\partial z = 0$, the equation which defines K can be written in terms of geostrophic departure,

$$\vec{\tau} = \rho K\,\partial\vec{V}/\partial z = \rho K\,\partial(\vec{V} - \vec{V}_g)/\partial z \quad . \tag{2}$$

It is useful to transform the variables and the equations into dimensionless forms. Let X denote a parameter having the physical dimension of a length; X will be referred to as the scale-height of the boundary layer. The dimensionless form of the independent variable will be denoted by $x \equiv z/X$, and differentiations with respect to x by primes. Using the symbol $\vec{i}$ for the horizontal unit vector in the direction of the geostrophic wind, we define dimensionless wind components (U, u, v), dimensionless shearing-stress components (s, t), and a dimensionless eddy viscosity (y) by the following four identities:

$$\vec{i}(u + iv) \equiv \vec{V}/Xf$$

$$\vec{i}U \equiv \vec{V}_g/Xf$$

$$\vec{i}(s + it) \equiv \vec{\tau}/\rho X^2 f^2$$

and $$y \equiv K/X^2 f \quad .$$

With the aid of the dimensionless independent and dependent variables, the two vector equations (1) and (2) yield a scalar system of four simultaneous first-order differential equations,

$$s = yu' \; ; \quad s' = -v \; ; \quad t = yv' \; ; \quad t' = u - U \; , \tag{3a}$$

which is equivalent to a scalar system of two simultaneous second-order differential equations,

$$s = yt'' \; ; \quad t = -y s'' \; , \tag{3b}$$

which also is equivalent to one scalar fourth-order differential equation,

$$s = -y(y s'')'' \; . \tag{3c}$$

It can be readily verified that equation (3c) applies for t in the same form as for s. The transformation to corresponding differential equations in u and v is possible but results in more complicated expressions than that for s and t.

The boundary conditions at large height ($x >> 1$) are

$$s = t = s' = t' = 0 \; ,$$

while at the surface,

$$s = s_0 > 0 \; ; \quad t = t_0 > 0 \; ; \quad (s')_0 = 0 \; ; \quad (t')_0 = -U \; .$$

In view of the later discussion of conditions at rough boundaries, with a defined aerodynamic roughness parameter z_0 of the earth's surface, it is useful to define the independent variable in dimensionless form as $x \equiv (z + z_0)/X$. This does not affect the above definitions and equations. The only consequence is that the lower boundary conditions (at $z = 0$) now refer to $x = x_0 = z_0/X$, which is a very small number in comparison to unity.

The problem is to integrate the basic equations (1) and (2), or one of the equivalent systems (3), in order to obtain the vertical profiles (spirals) of geostrophic departure and shearing stress in the atmospheric boundary layer. Obviously, the solution depends exclusively on the analytical formulation of the height dependency of K, or $y = y(x)$. The simplest possible case, that of $K = K_0 = \text{const}$ (or $y' = 0$), results in the classical Ekman-spiral solution. For K being a linear or an exponential function, or a power law of height, closed solutions exist and are given by Bessel functions (Hankel functions). For K being a quadratic function of height, the closed solution is expressed by elementary functions and is known as the Rossby-spiral solution. None of these, or related solutions, using explicit height functions for the eddy viscosity K, has produced satisfactory agreement with observational data.

The reason for this lack of success can be explained by the fact that eddy viscosity K is the product of a length times a velocity. Only the length term can be expected to be an explicit function of the distance from the lower boundary, while the velocity term will depend on the shearing velocity, which, in turn, depends on the solution of the basic differential equations. Consequently, the problem involves a characteristic degree of non-linearity.

It is the purpose of the following discussion to derive a new solution of the atmospheric boundary layer problem. The new theory is based on concepts which have been found useful in the treatment of fully developed flow in straight ducts — Lettau (1961); see Section 8.

9.2 Theoretical Model Hypotheses

The absolute value of the horizontal vector of shearing stress is a scalar quantity τ which decreases monotonically with height, from the surface-stress value, τ_0, to zero at the top of the boundary layer. The scalar shearing velocity is defined as $\sqrt{\tau/\rho}$. It is assumed that the eddy viscoscity K in a scalar form of equation (2) can be expressed as

$$\tau/(\rho\, \partial V/\partial z) \equiv K = \ell \sqrt{\tau/\rho}\ ; \quad \text{thus,} \quad \ell = \sqrt{\tau/\rho}\,/\,\partial V/\partial z\ . \qquad (4a)$$

This establishes the defining equation of the characteristic length scale of turbulence, ℓ. Let the dimensionless length scale of turbulence (ℓ/X) be denoted by $F = F(x)$. Recalling that the dimensionless components of the shearing stress vector were s and t, equation (4a) is, in dimensionless form,

$$y = F(s^2 + t^2)^{\frac{1}{4}} = F\,T = F(x) \cdot T(x) \ , \qquad (4b)$$

where the convenient abbreviation $T^4 \equiv s^2 + t^2$ is introduced. The dimensionless shearing stress intensity, therefore, can be written as $T^2 = \tau/\rho X^2 f^2$.

The above definition of the characteristic length scale of turbulence conforms with eddy-spectrum concepts in that ℓ corresponds closely to the largest eddy size of the inertial subrange. The scalar product $\vec{\tau} \cdot \partial\vec{V}/\partial z = \tau\, \partial V/\partial z \equiv \rho\varepsilon$ (ergs/cm^3 per sec) represents the rate at which mean-motion energy is locally converted to turbulent energy. If the mean flow and turbulence energy are in steady states, the local conversion rate $\rho\varepsilon$ must be equal to the local value of viscous energy dissipation. It is generally assumed that in fully developed turbulence this conversion process feeds mean-motion energy primarily and directly only into eddies of relatively large size (of characteristic scale ℓ) while viscous dissipation is important only in eddies of much smaller size. The physical quantities which describe the latter process are the above ε (cm^2/sec^3) and the molecular viscosity ν (cm^2/sec). Dimensional reasoning shows that the only possible combination of these two quantities which has the dimension of a length is $(\nu^3/\varepsilon)^{1/4}$. With a numerical factor sufficiently close to unity this relatively small length is considered to represent the lower limit of the inertial subrange of eddy sizes. With the effective or eddy viscosity (K), in place of molecular viscosity (ν), a corresponding dimensional argumentation results in the length $(K^3/\varepsilon)^{1/4}$, but this is the same as $\sqrt{\tau/\rho}\,/(\partial V/\partial z) = \ell$ and thus can be considered to represent the upper limit of the inertial subrange of eddy sizes.

A general hypothesis is introduced now as follows. F, the dimensionless length scale of turbulence in equation (4b) is assumed to be a universal function of the dimensionless distance from the lower boundary, of the analytical form

$$F = \kappa x/(1 + n^{-1}x^{1+n}) \ ; \ \text{so that} \ F'/F = nx^{-1}(1 - x^{1+n})/(n + x^{1+n}) , \qquad (5a)$$

where the two numerical parameters are $\kappa = 0.4$ = universal Kármán constant, while $n = 1/2$ for duct flow and $n = 1/4$ for atmospheric boundary layer flow. Equation (5a) is an extension of Prandtl's linear law of the length-scale of turbulence. For any value of n the F-function has a maximum value at $x = 1$, while

$$\lim_{x \to x_0} F' = \kappa \ .$$

In principle, such an extension of Prandtl's concept was first suggested and discussed by Rossby (1932); see Section 8.4.

When $n = 1/2$, i.e., for duct flow,

$$F = 0.4x / (1 + 2x^{\frac{3}{2}}) , \tag{5b}$$

and the F-maximum occurs at the center of the duct, so that $X = R =$ radius of the duct which is externally prescribed. In view of the exactly linear dependency of τ on x, no further hypothesis is necessary for the turbulent duct-flow problem, and the mean velocity profile is directly obtained by a closed integration; reference is made to Lettau (1961), see also Section 8.4.

In the atmosphere the width of the duct would correspond to the height of the geostrophic wind level. However, this level is not externally prescribed but depends on the flow conditions and must be obtained as the result of an integration of the equation of motion. Moreover, in contrast to duct flow, the height-dependency of shearing stress is not a priori known and must also be obtained as a result of the integration. Consequently, the general hypothesis, equation (5a), with $n = 1/4$ for atmospheric flow,

$$F = 0.4x/(1 + 4x^{\frac{5}{4}}) , \tag{5c}$$

must be supplemented by two additional hypotheses.

Upon logarithmic differentiation of equation (4b),

$$y'/y = F'/F + T'/T . \tag{6}$$

With $F'/F = 0$ at $x = 1$, it follows from equations (5a-c) that $F'/F > 0$ at $x < 1$. However, T'/T will be negative throughout the entire boundary layer. Consequently, a level $z^* < X$ must exist so that at $x^* = z^*/X$ we find that $y'/y = 0$ due to $F'/F = -T'/T$. In other words, a level z^* must exist where eddy viscosity reaches its maximum value.

The first hypothesis is that x^* is universally equal to $1/2$. This specific choice of the level of maximum eddy viscosity at half the scale-height (X) is suggested by empirical findings concerning both aerodynamic duct flow and atmospheric boundary flow.

The second hypothesis is that the level of maximum eddy viscosity in atmospheric boundary layers coincides with the level of maximum

cross-isobar flow. In non-dimensional terms, the cross-isobar component is v, and a maximum value requires that $v' = 0$, or, according to the third member of equation system (3a), $t = 0$.

Let starred symbols refer to values at the level of maximum eddy viscosity, $x^* = 0.5$. From equation (5c),

$$F^* = 0.2/(1 + 4/2^{\frac{5}{4}}) = 0.0746 ,$$

$$(F'/F)^* = 2(2^{\frac{1}{4}} - 1)/(2^{\frac{1}{4}} + 1) = 0.4322 .$$

From equation (6), considering that $(y'/y)^* = 0$,

$$(T'/T)^* = -(F'/F)^* = -0.4322 .$$

With the aid of the defining equation, $T^4 = s^2 + t^2$, and the subsequent form obtained by logarithmic differentiation, $4T'/T = (2s's + 2t't)/(s^2 + t^2)$, for $t^* = 0$, one finds that

$$T^* = \sqrt{s^*} \quad ; \quad \text{and} \quad 2(T'/T)^* = (s'/s)^* ,$$

whereupon,

$$y^* = F^* T^* = 0.0746 \sqrt{s^*} \quad ;$$

and

$$(s'/s)^* = -2(F'/F)^* = -0.8644 .$$

In summary, three function-values are fixed relative to s^*, at $x = x^*$, namely,

$$s^* = s^* \; ; \quad t^* = 0$$

$$(s')^* = -0.8644\, s^*$$

$$(s'')^* = -t^*/y^* = 0 \; ; \quad (t'')^* = s^*/y^* = 13.40\sqrt{s^*} .$$

A fourth value is at our disposal, which amounts to a choice of the ratio $(s'/t')^*$, or $(t')^*$.

9.3 Method of Integration

Given the function values of s and t, and their derivatives s', t', s'', and t'', at $x = x^*$, we want to solve a two-parameter family of curves, $s(x)$ and $t(x)$, by an integration of equations (3b). With the data-summary at the end of the preceding section, the problem is to find for what values (if any) of s^* and $(t')^*$ we obtain a spiral

solution in $s(x)$ and $t(x)$ which converges monotonically to the point $(0, 0)$, according to the boundary conditions at large x.

For the actual solution, the simple Cauchy method of numerical integration was employed, writing

$$s'(x + \Delta x) = s'(x) + \Delta x\,[s''(x) + s''(x + \Delta x)]/2 \ ,$$

$$s(x + \Delta x) = s(x) + \Delta x\,[s'(x) + s'(x + \Delta x)]/2 \ ,$$

and two corresponding forms for $t'(x + \Delta x)$ and $t(x + \Delta x)$.

Given a set of values $(x, F, s, s', s'', t, t', t'', y)$, we calculate a new set for $x + \Delta x$ by the following procedure:

(a) $F(x + \Delta x)$ is calculated directly.

(b) Using the value of $s''(x)$ as a first approximation for $s''(x + \Delta x)$ we calculate s' and s, at $x + \Delta x$, by the Cauchy formula.

(c) Using the value of $y(x)$ we obtain $t'' = s/y$ at x, and using $t''(x)$ as a first approximation for $t''(x + \Delta x)$ we calculate t' and t, at $x + \Delta x$, by the Cauchy formula.

(d) With the aid of the above obtained values of s and t at $x + \Delta x$, we calculate new values of y and s'' at $x + \Delta x$ by $y = F(s^2 + t^2)^{1/4}$, and $s'' = -t/y$.

(e) In the fashion of a true iteration, we repeat the procedures (b) through (d), using the improved y and s'', until the values which are generated at $x + \Delta x$ agree with the values used to generate them.

Tentatively, using hand-computations, it was found that convergency of the spiral solution at large heights ($x > 3$) depended very delicately on the proper choice of the values of s^* (or $y^* = 0.0746\sqrt{s^*}$), and $(t')^*$. The quality of the convergence can be judged by plotting the spiral curves in an orthogonal u versus v (or t' versus s') diagram. Another criterion is that the value of y must decrease monotonically with x, at any $x > 0.5$.

A program was written for the IBM-704 using FORTRAN II. A constant increment of $\Delta x = 0.1$ was employed. The iteration was required to keep the difference between generated and assumed values for each step within 0.0001%. The numerical integration was performed from $x = x^* = 0.5$ up to $x = 4.5$, requiring 40 steps. During July and August,

1960, a total of 72 runs was made, with a systematic variation in values for y^* and $(t')^*$. The following example illustrates the narrow tolerance with which the quality of convergence was judged. When y^* was kept equal to 0.8318, $(t')^* = -93.284$ resulted in slight overshooting, $(t')^* = -93.291$ in slight undershooting of the desired convergence point (0, 0), at x larger than 3.5. Values of $(t')^*$ larger or smaller than the above mentioned figures, and also any slight variation of the y^* value, produced spiral distortions, and spurious minimum values of y at large x. It was concluded that the convergence criterion has absolute and objective significance.

After finding the correct values at $x = x^* = 0.5$, that is,

$$s^* = 124.41, \qquad (s')^* = -107.54,$$

$$t^* = 0.00, \quad \text{and} \quad (t')^* = -93.29,$$

the solution was completed by a numerical integration of equations (3b) downward from $x = 0.5$ to $x = 0.0050$. Eleven steps with a constant increment of $\Delta x = 0.045$ were used. At $x \leq 0.0050$ logarithmic extrapolation was employed.

9.4 Integration Results — Universal Wind Spiral

To facilitate a practical application of the wind profile computation, the results are presented not only as sets of x, F, s, s', s'', t, t', t'', y values (see Table 1) which were directly written out in great detail by the IBM-704, but also after certain transformations were made. We recall that s' and t' represent the two rectangular components of the dimensionless geostrophic departure. Let

$$r = \sqrt{s'^2 + t'^2} \quad \text{and} \quad \beta = \tan^{-1}(s'/t'), \tag{7}$$

so that r is the absolute value and β the azimuth of the dimensionless geostrophic departure. These functions are listed in Table 2. The dependent variable is quoted in two forms, $x = (z + z_0)/X$ and $\zeta = (z + z_0)/Z$ with $\zeta = 2x$ or $Z = X/2$. The scale-height of the boundary layer (X) was defined as the level where the length-scale of turbulence has the maximum value; the unit-height Z is defined as the level where eddy diffusivity has the maximum value and where, in the basic solution, the cross-isobar flow has a maximum value, too.

For any assumed set of lower boundary values (r_0, β_0), the two rectangular wind components parallel with, and perpendicular to the geostrophic wind, are

Table 1. Basic spiral solution as a function of relative altitude. $x = z/X$; F = relative scale of turbulence; s, t = rectangular components of relative stress; s', s'', t', t'' = first and second-order derivatives of s and t with respect to x; y = FT = dimensionless eddy diffusivity (where $T^4 = s^2 + t^2$).

x	F	s	s'	s''	t	t'	t''	y
4.0	0.0670	0.14	0.14	-6.6	0.23	-1.60	3.9	0.0349
3.6	.0691	-0.69	4.36	-12.2	0.90	0.88	-9.4	.0735
3.2	.0706	-3.19	7.36	-0.1	0.02	6.27	-25.3	.1261
2.8	.0723	-5.52	2.76	24.2	-4.70	17.53	-28.3	.1947
2.4	.0741	-3.98	-12.01	48.9	-13.70	26.55	-14.2	.2800
2.0	0.0761	5.25	-35.11	64.7	-24.76	26.99	13.7	0.3828
1.8	.0771	13.59	-48.37	67.5	-29.75	22.25	30.8	.4409
1.6	.0781	24.61	-61.83	66.6	-33.51	14.59	48.9	.5034
1.4	.0790	38.28	-74.73	62.0	-35.32	2.98	67.2	.5699
1.2	.0797	54.41	-86.35	53.9	-34.43	-12.25	85.1	.6394
1.0	0.0800	72.67	-96.02	42.5	-30.15	-31.01	102.4	0.7096
0.9	.0799	82.47	-99.93	35.7	-26.52	-41.67	110.9	.7435
0.8	.0795	92.62	-103.12	28.1	-21.77	-53.19	119.5	.7752
0.7	.0786	103.05	-105.51	19.7	-15.83	-65.59	128.4	.8029
0.6	.0771	113.68	-107.02	10.5	- 8.61	-78.91	138.1	.8234
0.5	0.0746	124.41	-107.54	0.0	0.0	-93.29	149.6	0.8318
0.4	.0704	135.13	-106.92	-12.3	10.11	-109.01	164.9	.8196
0.3	.0636	145.72	-104.89	-28.4	21.90	-126.70	188.9	.7715
0.2	.0521	156.00	-100.77	-54.1	35.63	-147.97	236.6	.6593
0.1	.0327	165.78	- 92.90	-120.1	51.59	-177.25	385.0	.4303
0.05	0.0183	170.21	- 84.44	-248	61.04	-202.5	693	0.2457
0.005	.00199	173.36	- 55.04	-2620	71.87	-278.7	6330	.0273
0.0005	.000200	173.53	- 24.61	-26700	73.29	-351.3	63000	.00275
0.00005	.000020	173.53	6.08	-267000	73.46	-423.7	630000	.000275
0.000005	.000002	173.53	36.84	-2670000	73.48	-496.1	6300000	.0000275

$$u/U = 1 - (r/r_0) \cdot \cos(\beta - \beta_0), \text{ and } v/U = (r/r_0) \cdot \sin(\beta - \beta_0) .$$

When these two terms are multiplied by the speed of the geostrophic motion (V_g), the dimensional wind components are obtained.

In addition to T^2 = absolute value of the dimensionless shearing stress we define its azimuth

$$\gamma = \tan^{-1}(t/s) \quad . \tag{8}$$

Values of T^2, T, γ and $\psi = \beta - \gamma$ are also listed in Table 2. The data of T^2 and γ serve to compute the stress spiral, considering that the relative stress components parallel with and perpendicular to the surface stress are

$$(T^2/T_0^2) \cos(\gamma - \gamma_0), \text{ and } (T^2/T_0^2) \sin(\gamma - \gamma_0) .$$

The angle ψ formed by the vectors of geostrophic departure and shearing stress shows a significant height dependency at $x < 0.5$. It will be remembered that in the classical Ekman-spiral this angle is constant and equal to 45°.

In order to compute an actual wind spiral it is necessary to specify the external conditions. As a minimum requirement, this means that a set of three parameters must be given — the geostrophic speed V_g, the Coriolis parameter f, and the aerodynamic surface roughness z_0. The non-dimensional combination of these three quantities is the surface-Rossby number (see Lettau (1959)),

$$\underline{Ro}_0 = V_g/z_0 f \quad . \tag{9}$$

Owing to the boundary condition of zero wind speed at the surface, the quantity r_0 (which is the absolute value of the dimensionless geostrophic departure at $z = 0$) must be equal to the dimensionless geostrophic speed (U). Recalling that $x_0 = z_0/X$, it follows that

$$\underline{Ro}_0 = U/x_0 = r_0/x_0 \quad . \tag{10}$$

Consequently, with the aid of the listings in the lower part of Table 2, we can establish the functional relationship between r/x, and r, T^2, T, or the angular quantities. Obviously, at $z = 0$, ψ_0 equals α_0, since the wind vector in the immediate vicinity of the surface will be parallel with the surface stress, while α_0 is the angle formed by the wind nearest to the surface, and the geostrophic motion. It can be noted that r/x varies by many powers of ten. Therefore, the

Table 2. Universal spiral solution for geostrophic departure and stress as a function of relative height. $\zeta = z/Z = 2x$; r, β = relative magnitude and azimuth of geostrophic departure; T^2, γ = relative magnitude and azimuth of horizontal stress; T = relative magnitude of friction velocity; $\psi = \beta - \gamma$ = angle formed by the vectors of stress and geostrophic departure.

x	ζ	r	β (deg)	T^2	γ (deg)	T	ψ (deg)
4.0	8.0	1.66	377.8	0.27	323.6	0.52	54.2
3.8	7.6	2.74	338.5	0.59	286.8	0.77	51.7
3.6	7.2	4.45	304.4	1.13	255.0	1.06	49.4
3.4	6.8	6.74	276.7	1.96	227.4	1.30	49.3
3.2	6.4	9.68	252.5	3.19	203.3	1.78	49.2
3.0	6.0	13.3	231.1	4.92	181.8	2.22	49.3
2.8	5.6	17.1	211.9	7.25	162.5	2.69	49.4
2.6	5.2	23.0	194.5	12.67	145.1	3.56	49.4
2.4	4.8	29.0	178.6	14.27	129.1	3.78	49.5
2.2	4.4	36.1	164.0	19.21	114.5	4.38	49.5
2.0	4.0	43.0	150.5	25.3	101.0	5.03	49.5
1.8	3.6	53.8	137.9	32.9	88.4	5.73	49.5
1.6	3.2	63.6	126.2	41.4	76.6	6.44	49.6
1.4	2.8	74.8	115.2	52.1	65.6	7.22	49.6
1.2	2.4	86.9	104.9	64.4	55.3	8.02	49.6
1.0	2.0	100.6	95.0	78.7	45.5	8.87	49.5
0.9	1.8	108.3	90.3	86.6	40.8	9.31	49.5
0.8	1.6	116.1	85.7	96.7	36.2	9.83	49.5
0.7	1.4	124.2	81.1	104.3	31.7	10.43	49.4
0.6	1.2	133.0	76.6	114.0	27.3	10.68	49.3
0.5	1.0	142.4	72.0	124.2	22.9	11.14	49.1
0.4	0.8	152.7	67.4	135.6	18.5	11.64	48.9
0.3	0.6	164.5	62.6	147.2	14.3	12.15	48.3
0.2	0.4	179.0	57.2	160.0	10.1	12.65	47.1
0.1	0.2	199.7	50.1	173.9	5.6	13.16	44.5
5.10^{-2}	1.10^{-1}	219.4	45.6	180.6	3.2	13.45	42.4
5.10^{-3}	1.10^{-2}	283.1	34.1	187.9	0.4	13.70	33.7
5.10^{-4}	1.10^{-3}	351.1	27.0	188.5	0.1	13.74	26.9
5.10^{-5}	1.10^{-4}	413.7	22.1	188.6	0.0	13.75	22.1
5.10^{-6}	1.10^{-5}	497.4	18.7	188.6	0.0	13.75	18.7
5.10^{-7}	1.10^{-6}	572.5	16.2	188.6	0.0	13.75	16.2

common logarithm of the surface-Rossby number was utilized for the interpolations which resulted in the data summarized in Table 3. With the aid of Table 3, the boundary values (r_0, T_0^2, T_0, α_0, β_0, and γ_0) can be interpolated for a given set (V_g, z_0, f) or the subsequent surface-Rossby numbers.

At this point, an order-of-magnitude discussion will be illustrative. While both V_g and f will normally vary by no more than a factor of 4 (or 1/4) about their average values (V_g approximately 1,000 cm/sec and f approximately 0.00005 sec^{-1}), the aerodynamic roughness parameter z_0 of natural ground can vary from more than 100 cm (for tall vegetation) to less than 0.01 cm (for snow surfaces, etc.). Consequently, the surface-Rossby number may range from approximately 10^5 to 10^9. This is considered in the computations which are summarized in Table 3 and the following tables, where certain variables are quoted as a function of the surface-Rossby number.

Table 3. Dependence of parameters of theoretical wind and stress spirals on surface-Rossby number $\underline{Ro}_0$. T_0^2 = relative magnitude of the surface stress; α_0 = angle formed by surface stress and geostrophic wind; r_0, β_0 = relative magnitude and azimuth of the surface geostrophic wind; $\gamma_0 = \beta_0 - \alpha_0$; T_0 = relative magnitude of the surface friction velocity.

$\log_{10} \underline{Ro}_0$	T_0^2	α_0 (deg)	r_0	β_0 (deg)	γ_0	T_0
4.5	187.6	35.0	269.2	36.0	1.0	13.67
5.0	188.1	31.9	299.3	32.2	0.3	13.72
5.5	188.3	28.9	330.4	29.0	0.1	13.73
6.0	188.5	26.1	362.4	26.1	0.0	13.73
6.5	188.6	23.7	395.2	23.7	0.0	13.73
7.0	188.6	21.7	428.7	21.7	0.0	13.73
7.5	188.6	20.1	462.8	20.1	0.0	13.73
8.0	188.6	18.7	497.4	18.7	0.0	13.73
8.5	188.6	17.4	532.4	17.4	0.0	13.73
9.0	188.6	16.2	567.8	16.2	0.0	13.73
9.5	188.6	15.1	603.5	15.1	0.0	13.73

For the conversion of dimensionless distance from the surface (x, or $\zeta = 2x$) into absolute or metric heights we consider again that $r = U = V_g/Xf = V_g/2Zf$. Thus, a unit-height coefficient, $C_Z = \frac{1}{2} r_0$, can be defined in the relation

$$Z = C_Z \, V_g/f \; ; \quad \text{or} \quad X = 2 \, C_Z \, V_g/f \; . \tag{11}$$

It follows from the universal wind-spiral solution in Table 2 or Table 3 that the unit-height coefficient C_Z is a unique-valued function of the surface-Rossby number. Numerical values are listed in Table 4. With them we can compute the unit-height Z, or the scale-height of the boundary layer $X = 2Z$, for any given set (V_g, z_0, f).

Table 4. Non-dimensional coefficients of theoretical wind spirals as functions of the surface-Rossby number $\underline{Ro}_0$. C = geostrophic drag coefficient; C_Z = unit height coefficient; C_K = maximum-diffusivity coefficient; C_M = coefficient of mass transport across the isobars.

$\log_{10} \underline{Ro}_0$	C	$10^5 \cdot C_Z$	$10^7 \cdot C_K$	C_M
4.5	0.0508	187.4	116.9	1.13
5.0	.0459	167.1	92.9	1.06
5.5	.0416	151.3	76.2	1.00
6.0	.0379	138.0	63.4	.94
6.5	.0347	126.5	53.2	.88
7.0	.0320	116.7	45.2	.82
7.5	.0297	108.1	38.8	.77
8.0	.0276	100.5	33.6	.72
8.5	.0258	93.9	29.3	.68
9.0	.0242	88.1	25.8	.64
9.5	.0228	82.8	22.8	.60

As an example, let $f = 10^{-4}$ sec^{-1}, $z_0 = 5$ cm, and $V_g = 15.8$ m/sec. Then $\underline{Ro}_0 = 3.16 \; 10^6$ or $\log_{10} \underline{Ro}_0 = 6.50$, and $V_g/f = 1.57 \; 10^5$ m. For this surface-Rossby number, Table 4 gives $C_Z = 126.5 \; 10^{-5}$, whereupon $Z = 126.5 \times 1.57 = 199$ m. The unit-height Z will have the order of magnitude of 10^2 m in nearly all cases; exceptions will only occur for extremely low geostrophic speeds.

In a similar manner the absolute magnitude of the surface drag (τ_0) or the surface-friction velocity ($\sqrt{\tau_0/\rho}$) can be computed from $T_0/U = T_0/r_0 = \sqrt{\tau_0/\rho}/V_g$. This relationship is the basis for the definition of the geostrophic drag coefficient $C = T_0/r_0$ in the equation

$$\sqrt{\tau_0/\rho} = C V_g \; ; \quad \text{or} \quad \tau_0 = \rho C^2 V_g^2 \; . \tag{12}$$

It follows from the universal wind-spiral solution that the geostrophic drag coefficient C is a unique function of the surface-Rossby number. Numerical values are listed in Table 4. They permit us to compute τ_0 (or $\sqrt{\tau_0/\rho}$) for any given set (V_g, z_0, f).

The listings in Table 4 include also the maximum eddy-viscosity (or diffusivity) coefficient C_K which is defined in the relation

$$K_{max} = C_K V_g^2/f \; , \tag{13}$$

where K_{max} = maximum value of K which was assumed to occur at $x = x^* = 0.5$ or $\zeta = 1.0$, i.e., $z = Z$. Another coefficient is that of total mass transport across the isobars, C_M, which is defined in the relation

$$\int_0^\infty V_g (v/U)\, dz = C_M Z V_g \; , \tag{14}$$

where $v/U = (r/r_0) \cdot \sin(\beta - \beta_0)$ = dimensionless cross-isobar flow, and Z = unit-height, as defined above. This mass transport across the isobars, due to friction and the subsequent imbalance between pressure gradient force and Coriolis force, is well known for any solution of atmospheric boundary layer flow — for example, the Ekman-spiral solution.

Inspection of the values listed in Table 4 reveals that all coefficients decrease significantly with increasing surface-Rossby number. It can be concluded that surface drag, boundary-layer scale height, maximum eddy viscosity, and mass transport across the isobars, are significantly dependent on the aerodynamic roughness parameter z_0 of the terrain under consideration.

Several characteristic levels (relative to unit-height, Z) of the atmospheric boundary layer are listed in Table 5, as a function of the surface-Rossby number. The height of the surface layer, h, denotes that level at which the wind speed, computed from the spiral solution, begins to deviate by more than 5% from the conventional logarithmic law. More detail will be discussed in connection with data listed in

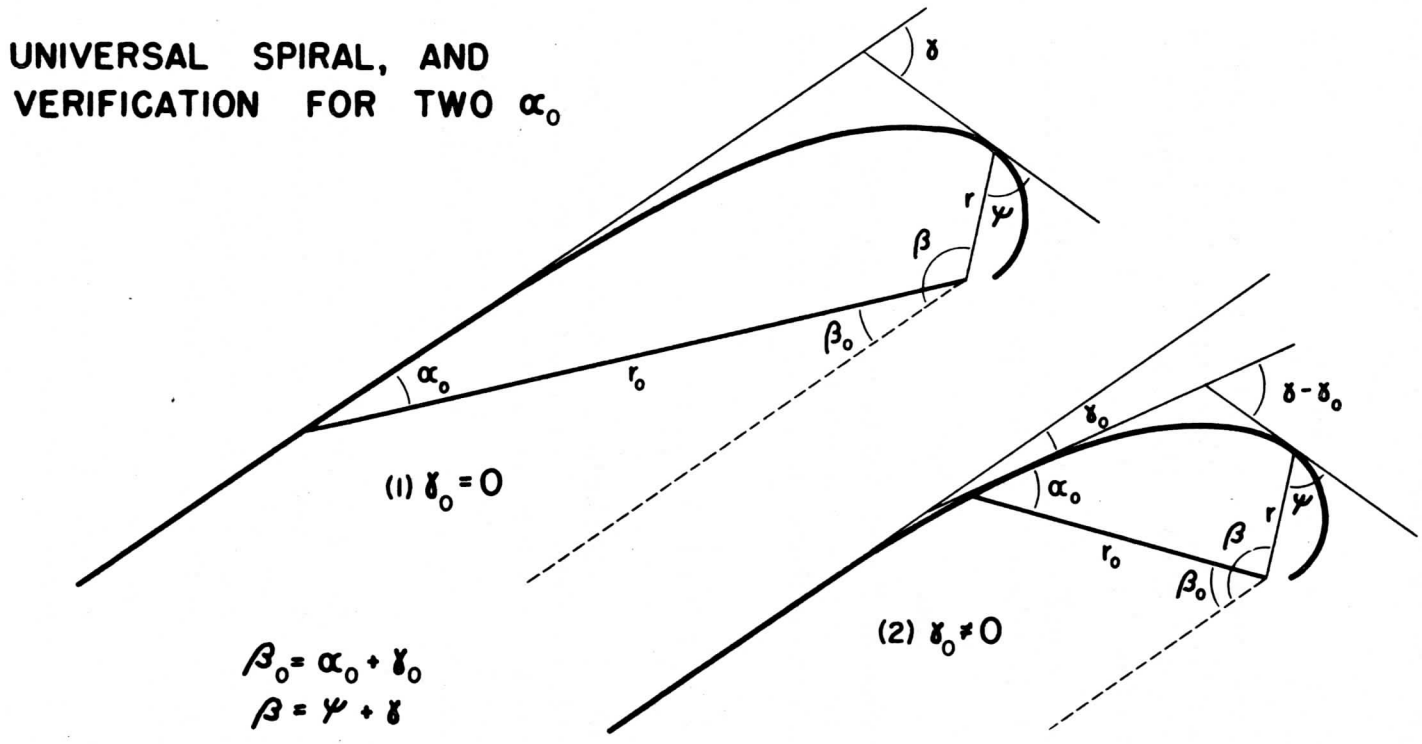

Fig. 1. Universal wind spiral solution (heavy curves) and verification for two different boundary conditions (α_0, β_0, and r_0).

Table 6. The geostrophic displacement thickness δ is defined in analogy to the displacement thickness of flat-plate boundary layer flow. The wind component parallel to the geostrophic wind, i. e., $u/U = 1 - (r/r_0) \cdot \cos(\beta - \beta_0)$ is considered, and δ is defined in the relation

$$\int_0^\infty V_g \, u \, dz = \int_\delta^\infty V_g \, U \, dz ; \quad \text{or} \quad \delta = \int_0^\infty (1 - u/U) \, dz \; . \tag{15}$$

δ can be interpreted as the level above which an exactly geostrophic motion would produce the same total mass transport (in the direction parallel to the isobars) as is produced by the actual wind above the level $z = 0$. In the unidimensional shear flow above a flat plate in the wind tunnel, the air between 0 and δ can be thought of as being brought to rest; however, atmospheric boundary layer flow is two-dimensional (spiral flow), and it is necessary to consider the air between the surface and the level δ as moving parallel to the direction of the pressure gradient from high to low pressure; in fact, this layer can be thought of as absorbing the total cross-isobar flow, which was expressed with the aid of the coefficient C_M in Table 4. Obviously, horizontal variations in this total cross-isobar flow will result in frictionally induced mean vertical motion at the top of the atmospheric boundary layer.

Table 5. Relative height of characteristic levels as functions of the surface-Rossby number $\underline{Ro}_0$ (relative to unit height $Z = C_Z \, V_{g,o}/f$). h = height of the surface layer (for 5% deviation from log-law); δ = geostrophic displacement thickness; z_y = level of maximum cross-isobar flow; H = height of the "geostrophic wind level."

$\log_{10} \underline{Ro}_0$	h/Z	δ/Z	z_y/Z	H/Z
4.5	0.106	0.265	1.59	5.69
5.0	.273	.242	1.42	5.61
5.5	.340	.221	1.28	5.53
6.0	.403	.202	1.16	5.46
6.5	.465	.185	1.05	5.40
7.0	.526	.171	.96	5.35
7.5	.587	.159	.88	5.31
8.0	.648	.148	.81	5.28
8.5	.709	.138	.75	5.25
9.0	.770	.129	.70	5.22
9.5	.830	.122	.65	5.20

NORMALIZED WIND SPIRALS FOR VARIOUS SURFACE-ROSSBY NUMBERS ($\underline{Ro}_0$)

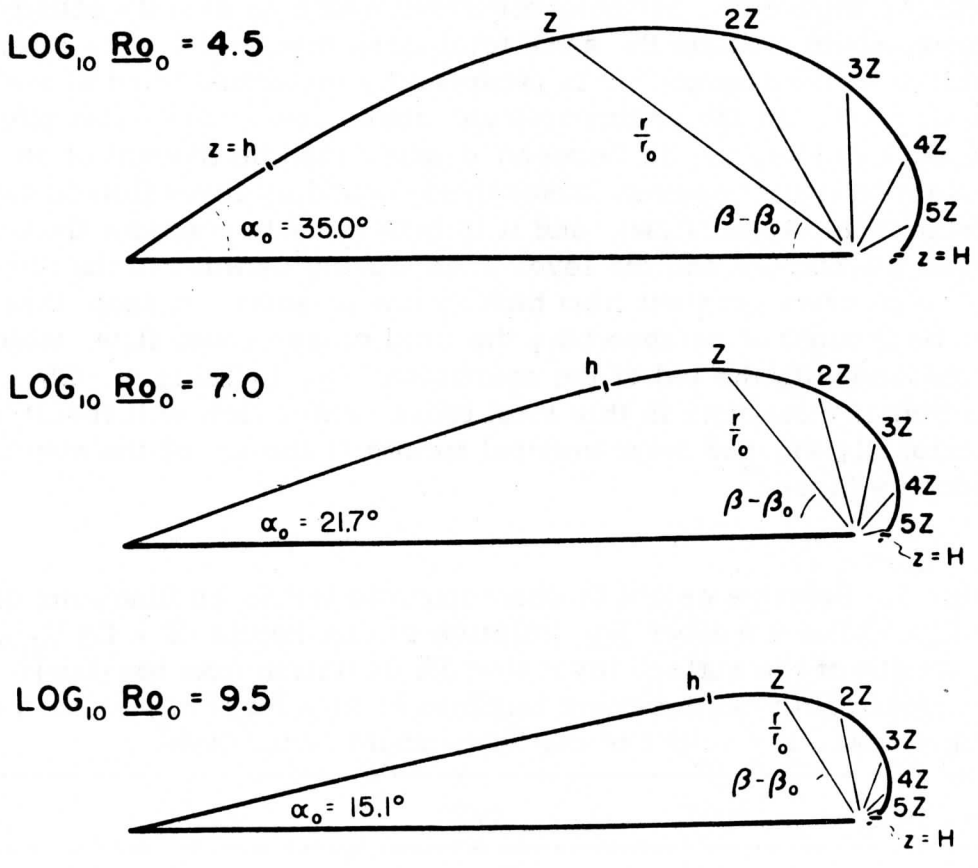

Fig. 2. Normalized theoretical wind spirals for extremely low, moderate, and extremely high surface-Rossby numbers.

The level of maximum cross-isobar flow is also listed in Table 5. It will be remembered that, in the basic spiral solution, this level was made to coincide with $z = Z$. However, introducing actual surface-reference values causes this level to become a function of the surface-Rossby number.

The universal spiral solution listed in Table 2 shows that the angle β increases continuously with height. For every β_0 there must exist special levels where $\beta - \beta_0$ equals 180°, then 360°, 540°, etc. At any of these special levels the actual wind vector is parallel to the geostrophic wind vector. The first of these special levels, i.e., the height at which $\beta - \beta_0 = 180°$, is conventionally referred to as the "geostrophic wind level," H, even though only the direction, but not the speed, is truly geostrophic. Values of H can be obtained from the ratio H/Z listed in Table 5. It is interesting to note that H, like z_y and δ, increases with decreasing surface-Rossby number, while the height of the surface layer, h, behaves in the opposite manner.

A direct consequence of the particular choice for the F-function in the boundary layer solution is that the wind speed profile in the lowest air layer approaches the conventional logarithmic law,

$$(V_g/U)\sqrt{u^2 + v^2} \approx \kappa^{-1}\sqrt{\tau_0/\rho}\,\log_e(z + z_0)/z_0 .$$

The deviation from the logarithmic law is negligible very close to the surface, but increases gradually with height, due to three causes: (1) actual veering of wind direction with height, (2) existing vertical gradient of shearing stress, and (3) non-linear increase of the ℓ term with height. Table 6 shows at which levels the deviation reaches values of 2, 5, and 10%. All these h-levels are strongly dependent on the surface-Rossby number. Previously, estimates of the height of the surface layer were based on the relative momentum divergence, i.e., on a certain value of $(\tau_0 - \tau)/\tau_0$; reference can be made to Lettau (1957a). In this case, a possible non-linearity in the height increase of the length scale of turbulence and also possible changes of wind direction with height were disregarded. It follows from the data in Table 6 that the effect of shear-stress gradients seems to be partially compensated by the effect of the height decrease of the gradient of length scale of turbulence. Evidence of this is the fact that the listed values of the ratio $\Delta\tau/\tau_0$ are nearly always significantly larger than the percentage figures denoted by "i" in Table 6. The only exception occurs at lowest surface-Rossby number, i.e., most likely for extremely rough ground surface. Certain consequences of these findings, with respect to wind profile curvature in the adiabatic surface layer, will be discussed in a forthcoming report.

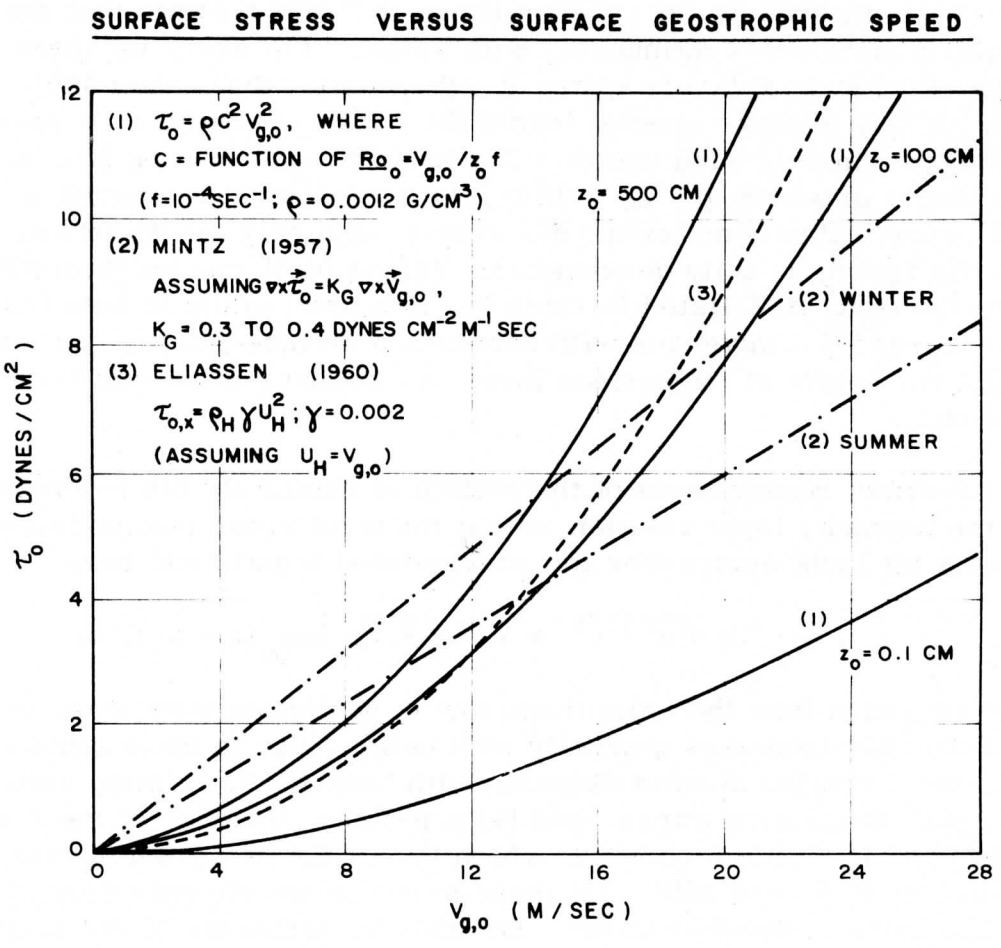

Fig. 3. Surface stress as a function of surface geostrophic speed. (1) From wind spiral theory and geostrophic drag coefficient relationships; (2) after Mintz (1957); and (3) after Eliássen (1960).

Table 6. Surface-layer characteristics as functions of the surface-Rossby number $\underline{Ro}_0$. h_i = level at which the wind speed computed from the spiral solution deviates by i% (for i = 2, 5, and 10) from the logarithmic law (for which $V = 2.5\, T_0\, V_{g,o} \log_e (x/x_0)$); Z = unit height $= C_Z\, V_{g,o}/f$; $\Delta\tau/\tau_0 = \Delta T^2/(T^2)_0 = (\tau_0 - \tau_h)/\tau_0$ = relative stress gradient, or total momentum-flux divergence between the levels 0 and h_i.

	i = 2%		i = 5%		i = 10%	
$\log_{10} \underline{Ro}_0$	h_i/Z	$\Delta\tau/\tau_0$	h_i/Z	$\Delta\tau/\tau_0$	h_i/Z	$\Delta\tau/\tau_0$
4.5	0.01	0.004	0.11	0.044	0.37	0.141
5.0	.09	.036	.27	.087	.59	.214
5.5	.12	.050	.34	.122	.73	.258
6.0	.15	.062	.40	.151	.86	.300
6.5	.18	.073	.46	.175	.99	.341
7.0	.21	.084	.53	.196	1.12	.381
7.5	.24	.094	.59	.216	1.25	.418
8.0	.26	.104	.65	.236	1.38	.452
8.5	.29	.114	.71	.256	1.51	.481
9.0	.32	.124	.77	.276	1.64	.505
9.5	.35	.134	.83	.296	1.77	.524

9.5 Comparison with Observations — Applications

With the aid of the universal spiral solution, i.e., the r and β values listed in Table 2, together with the boundary values r_0, β_0 in in Table 3, a wind spiral for any given set (V_g, z_0, f) can be constructed. Figure 1 illustrates the general procedure, and the relationships among the variables of the spiral solutions, for two different boundary values. Figure 2 shows normalized wind spirals for three different surface-Rossby numbers. The normalization involves the turning of the geostrophic wind vector into a horizontal direction and constructing the spirals of geostrophic departure in the relative terms of r/r_0 and $\beta - \beta_0$. These theoretical spirals are in satisfactory agreement with observed spirals over land (for low $\underline{Ro}_0$) and over the ocean (high $\underline{Ro}_0$); reference is made to the illustration of the "Leipzig wind profile" and the "Scilly wind profile" in Lettau (1957b, Figure 3).

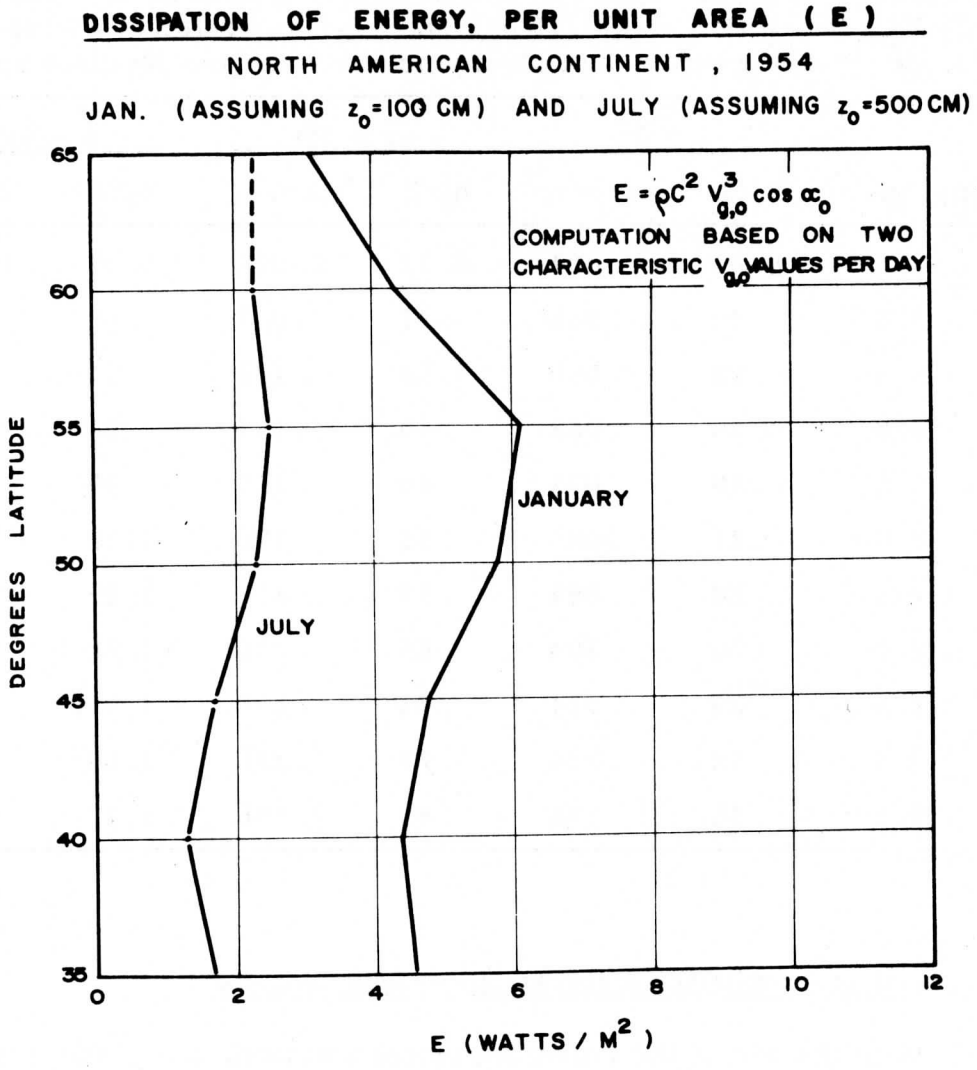

Fig. 4. Seasonal contrast of dissipation of energy in the atmospheric boundary layer. Computed from sea-level geostrophic winds over the North American continent in January and July 1954, with the aid of geostrophic drag coefficients.

Table 7. A quantitative comparison between observed and calculated wind spiral data for both land and ocean boundaries.

Observations: Leipzig (08 to 15 GCT on 20 October 1931): $f = 1.14\ 10^{-4}\ sec^{-1}$, $V_{g,o} = 17.51$ m/sec, estimated $z_0 = 30$ cm; consequently, $Ro_0 = 5.13\ 10^5$ — Ocean near Scilly Islands (12 to 15 GCT on 4 January 1951): $f = 1.11\ 10^{-4}\ sec^{-1}$, $V_{g,o} = 12.19$ m/sec, estimated $z_0 = 0.03$ cm; consequently, $Ro_0 = 3.66\ 10^8$.

Theory: Data calculated from coefficients and ratios interpolated for $\log_{10} Ro_0$ values of 5.71 (for Leipzig) and 8.56 (for Scilly) on Tables 3, 4, and 5; assumed air density $\rho = 0.00115$ g/cm^3.

Quantity	Leipzig (Land)		Scilly (Ocean)	
	Observed	Calculated	Observed	Calculated
α_0 (deg) = angle between surface wind and isobars	26.1	27.7	13.9	17.3
τ_0 (dynes/cm^2) = surface stress	5.31	5.65	0.92	1.13
Z(m) = unit height (level where $K = K_{max}$)	235	223	100	102
K_{max}(cm^2/sec) = maximum eddy diffusivity	144,700	205,000	28,000	41,000
z_y(m) = level of maximum cross-isobar wind component	250	274	70	75
H(m) = geostrophic wind level (first level where cross-isobar wind component equals zero)	1070	1200	480	534
$\ell_{max}(m) = (K^3/\varepsilon)^{\frac{1}{4}}$ at $z = 2Z$	32	36	13	16

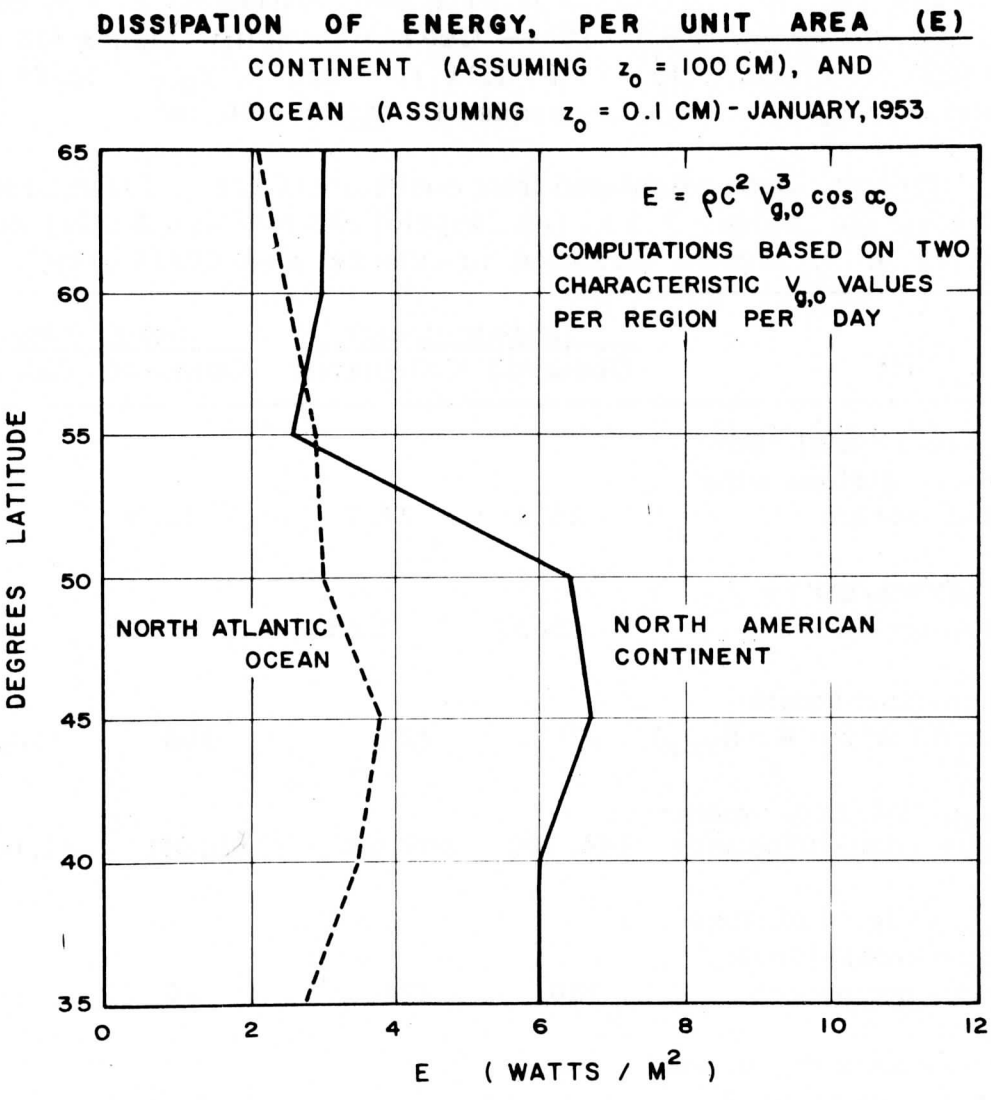

Fig. 5. Ocean-continent contrast of dissipation of energy in the atmospheric boundary layer. Computed from sea-level geostrophic winds over the American continent and the Atlantic Ocean in January, 1953, with the aid of geostrophic drag coefficients.

More detailed comparisons of various quantities, such as the spread between the surface wind and the geostrophic wind (α_0), the height variation of the length scale of turbulence, and eddy viscosities are presented in Table 7, using data discussed by Lettau (1957b).

Besides wind profile characteristics, a comparison with observational data can also be based on surface stress values. The theoretical relationship $\tau_0 = \rho C^2 V_g^2$ with $C = C(\underline{Ro}_0)$ shows satisfactory agreement with empirical data reported by Lettau (1959). Figure 3 illustrates stress versus geostrophic wind, as discussed in two studies of large-scale atmospheric motion. Mintz (1958) assumes a linear relationship which involves a dimensional coefficient of proportionality; Eliassen (1960) assumes a quadratic relationship. Owing to the dependency of C on $\underline{Ro}_0$ (or V_g), the expression $\tau_0 = \rho C^2 V_g^2$ is actually not exactly quadratic; this can be noted on Figure 3. For the range of normal V_g between 10 and 15 m/sec, nearly all the curves on Figure 3 agree with each other, and produce stress values between 3 and 5 dynes/cm^2, when the curve for low z_0 is disregarded. Mintz' distinction between winter and summer curves may be explained by the fact that V_g is lower in summer than in winter; an effect of heating and cooling conditions would most likely act in the opposite direction. This will be discussed in more detail in a later report.

The important advantage of the concept of the geostrophic drag coefficient is that C is uniquely determined by the external conditions. Furthermore, its application leads to an extremely simple and straightforward method for the determination of the total energy dissipation in the lower troposphere. Consider an integration of the scalar product which represents the work necessary to overcome the frictional force,

$$\int_0^H \vec{V} \cdot (\partial\vec{\tau}/\partial z)dz = [\vec{V} \cdot \vec{\tau}]_0^H - \int_0^H \vec{\tau} \cdot (\partial\vec{V}/\partial z)dz = -\int_0^H \rho\varepsilon \, dz = -E \,, \qquad (16)$$

where $\rho\varepsilon$ = local value of energy dissipation (ergs cm^{-3} sec^{-1}), and E = total value of energy dissipation in the boundary layer (ergs cm^{-2} sec^{-1} = 10^{-3} watts/m^2). The scalar product $\vec{V} \cdot \vec{\tau}$ gives no contribution due to the fact that $\vec{V} = 0$ at $z = 0$ and $\vec{\tau} = 0$ at $z \geq H$.

With the assumptions quoted in the introduction — see equation (1) — one obtains that $\vec{V} \cdot (\partial\vec{\tau}/\partial z)$ equals exactly $\vec{V}_g \cdot (\partial\vec{\tau}/\partial z)$. Namely, by repeated application of the rules of scalar multiplication of vectors, considering that $\vec{V} \cdot i\vec{V} = 0$,

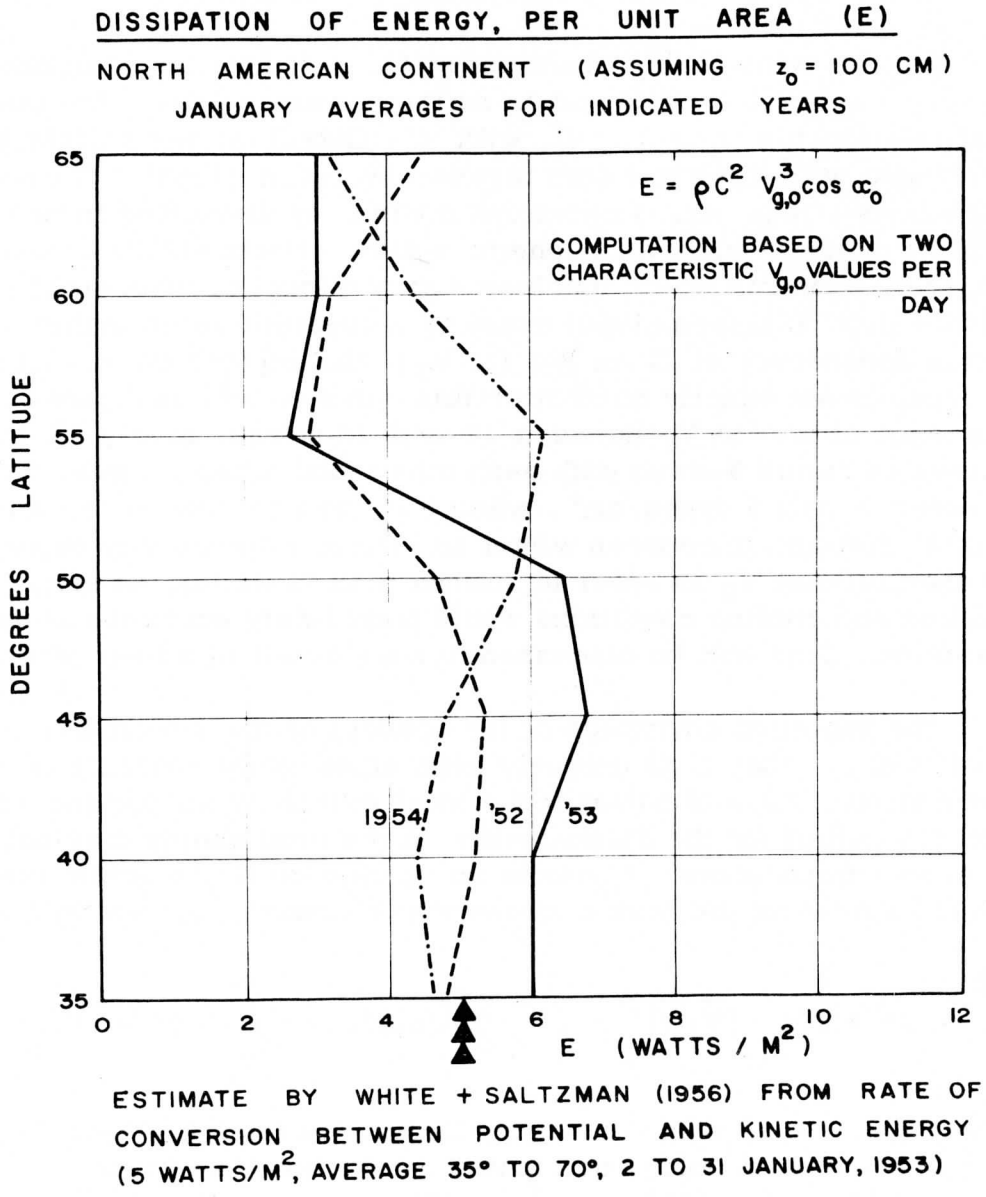

Fig. 6. Year-to-year differences in the dissipation of energy in the atmospheric boundary layer. Computed from sea-level geostrophic winds over the North American continent for the months of January in 1952, 1953, and 1954, with the aid of geostrophic drag coefficients.

$$\vec{V} \cdot (\partial\vec{\tau}/\partial z) = \vec{V} \cdot \rho f i(\vec{V} - \vec{V}_g) = -\rho f \vec{V} \cdot i\vec{V}_g = \rho f \vec{V}_g \cdot i\vec{V} = \rho f \vec{V}_g \cdot i(\vec{V} - \vec{V}_g) =$$

$$\vec{V}_g \cdot (\partial\vec{\tau}/\partial z) \quad . \qquad (17)$$

Consequently,

$$E = -\int_0^H \vec{V}_g \cdot (\partial\vec{\tau}/\partial z)\, dz = -V_g \cdot \int_0^H (\partial\vec{\tau}/\partial z)\, dz = \vec{V}_g \cdot \vec{\tau}_0 \quad , \quad \text{or}$$

$$E = V_g \, \tau_0 \cos \alpha_0 = \rho C^2 V_g^3 \cos \alpha_0 \quad . \qquad (18)$$

Results of sample computations of the total energy dissipation, based on daily V_g-estimates from surface weather charts between 30° and 70° northern latitude, and a tentatively assumed z_0-value of 100 cm for North America, and $z_0 = 0.1$ cm for the North Atlantic Ocean, are illustrated in Figures 4, 5, and 6. They show the seasonal contrast (January-July), the ocean-continent contrast, and differences from year to year, respectively. A basis for comparison is given for North America in January 1953 in that White and Saltzman (1956) derived, from a laborious investigation of the conversion between potential and kinetic energy in the troposphere, a mean dissipation value of 5 watts/m^2 , which compares satisfactorily with an average of the meridional distribution of E depicted on Figure 6.

References

Eliassen, A.: "On the Formation of Fronts in the Atmosphere," p. 276 in The Atmosphere and the Sea in Motion (Rossby Memorial Volume), Oxford University Press, New York, 1959.

Lettau, H.: "A Generalized Mathematical Model of the Mean Velocity Distribution in Fully Turbulent Duct Flow," Departments of Meteorology and Civil Engineering, University of Wisconsin, 1961 (see Section 8, This Report).

Lettau, H.: "Wind Profile, Surface Stress, and Geostrophic Drag Coefficients in the Atmospheric Surface Layer," Advances in Geophysics, Vol. 6, Academic Press, New York and London, 1959.

Lettau, H.: "Summary of Non-Dimensional Characteristics of Boundary Layer Theory," Sec. 7.5 in Exploring the Atmosphere's First Mile, Vol. I, Pergamon Press, New York and London, 1957a.

Lettau, H.: "Windprofil, Innere Reibung, und Energie Umsatz in den unteren 500 m ueber dem Meer," Beitr. Phys. d. Atmosph., Vol. 30, 78, 1957b.

Mintz, Y.: "An Empirically Determined Surface Stress Coefficient for Numerical Forecasting Experiments," Proceedings XI General Assembly in Toronto, Canada; Intern. Assoc. of Meteorology and Atmospheric Physics, London, 1958.

Rossby, C. G.: "A Generalization of the Theory of the Mixing Length with Applications to Atmospheric and Oceanic Turbulence," Mass. Inst. Tech. Meteorol. Papers, 1, No. 4, 1932.

INDEX OF DISTRIBUTION

Department of Defense Activities

Chief Signal Officer
Department of the Army
ATTN: SIGRD-4c
Washington 25, D. C. 1

Commanding Officer
U. S. Army Signal
Engineering Agency
Washington 25, D. C. 1

Commanding General
U. S. Army Signal Air Defense
Engineering Agency
ATTN: SIGAD-7a
Fort George Meade, Md. 1

Commanding General
U. S. Army Combat
Surveillance Agency
1124 North Highland St.
Arlington 1, Virginia 1

Chief, U. S. Army SigC
Operations Research Office
The Johns Hopkins University
Washington 25, D. C. 1

Commanding Officer
U. S. Army Signal R and D
Laboratory
ATTN: Chief, Met Div;
Surveillance Dept.
Fort Monmouth, New Jersey 2

President
U. S. Army Signal Board
Fort Monmouth, New Jersey 1

Commandant
U. S. Army Signal School
ATTN: Weather Br, DST
Fort Monmouth, New Jersey 1

Commanding Officer, U. S. Army
Signal Missile Support Agency
ATTN: Chief, Missile Meteor-
ology Division
White Sands, New Mexico 2

Commanding General
U. S. Continental Army Command
ATTN: ATSIG
Fort Monroe, Virginia 1

Deputy for Defense Research
and Engineering
Office of the Secretary of Defense
ATTN: Geophysical Sciences,
Office of Science
Washington 25, D. C. 1

Chief, Research and Development
Department of the Army
ATTN: CRD/M, Army Research
Office
Washington 25, D. C. 2

Commanding General
U. S. Continental Army Command
ATTN: ATINT, D and D Div.,
Weather Branch
Fort Monroe, Virginia 2

Commanding General
U. S. Continental Army Command
ATTN: 16th Weather Squadron
USAF Air Weather Service
Fort Monroe, Virginia 1

Commanding General
U. S. Continental Army Command
ATTN: Materiel Development
Fort Monroe, Virginia 1

Commandant
U. S. Army Command and
General Staff College
ATTN: Archives
Fort Leavenworth, Kansas 1

President
U. S. Army Artillery Board
Fort Sill, Oklahoma 1

Commandant
U. S. Army Artillery and
Missile School
ATTN: Development and
Doctrine Division
Fort Sill, Oklahoma 1

Commandant
U. S. Army Artillery and
Missile School
ATTN: Target Acquisition Div.
Fort Sill, Oklahoma 1

Commandant
U. S. Army Artillery and
Missile School
ATTN: Metro Div., Target
Acquisition Dept.
Fort Sill, Oklahoma 1

Chief of Ordnance
Department of the Army
ATTN: ORDTU
Washington 25, D. C. 1

Chief of Ordnance
Department of the Army
ATTN: ORDTB
Washington 25, D. C. 1

Commanding General
U. S. Army Ordnance
Missile Command
ATTN: Staff Assistance Div.,
Signal Office (ORDXM-DR)
Redstone Arsenal, Alabama 1

Commander
U. S. Army Rocket and Guided
Missile Agency
ATTN: T and E Laboratory
Redstone Arsenal, Alabama 1

Commander
U. S. Army Rocket and Guided
Missile Agency
ATTN: ORDXR-ODT
Redstone Arsenal, Alabama 1

Commander
U. S. Army Ballistics
Missile Agency
ATTN: Director, Research Lab,
ORDAB-RR
Redstone Arsenal, Alabama 1

Commanding General
White Sands Missile Range
ATTN: Office of Ordnance Mission
(ORDBS-OM-SS)
White Sands, New Mexico 1

Commanding General
Aberdeen Proving Ground
ATTN: U. S. Army Ballistic
Research Laboratories
Fort George Meade, Md. 1

Commanding Officer
Army Research Office (Durham)
Duke Station
Durham, North Carolina 1

Commanding Officer
Picatinny Arsenal
ATTN: Pyrotechnics Chemical
Research Section
Dover, New Jersey 1

Chief Chemical Officer
Department of the Army
ATTN: R and D Command
Washington 25, D. C. 1

Director
U. S. Army Chemical Corps
Opns Research Gp
U. S. Army Chemical Center
Edgewood, Maryland 1

Commanding Officer
U. S. Army Chemical Corps
Proving Ground
ATTN: Chief, Meteorology Div
Dugway, Utah 2

Chairman
U. S. Army Chemical Corps
Meteorological Committee
Fort Detrick
Frederick, Maryland 2

The Quartermaster General
Department of the Army
ATTN: Research Br,
R and E Div.
Washington 25, D. C. 1

Commanding Officer
U. S. Army Quartermaster
R and E Command
ATTN: EPR Div
Natick, Massachusetts 1

Chief of Engineers
Department of the Army
ATTN: Chief, Engineer
R and D Div
Washington 25, D. C. 1

Commanding Officer
U. S. Army Engineer
R and D Laboratory
ATTN: Tech Documents Center
Fort Belvoir, Virginia 1

Commanding Officer
U. S. Army Corps of Engineers
ATTN: SIPRE
1215 Washington Avenue
Wilmette, Illinois 1

Commanding Officer
U. S. Army Corps of Engineers
ATTN: Army Mobility Research
Center
Vicksburg, Mississippi 1

Chief of Transportation
Department of the Army
ATTN: CAD-E
Washington 25, D. C. 1

Chief of Transportation
Department of the Army
ATTN: TCCAD-E
Washington 25, D. C. 1

Commanding Officer
U. S. Army Transportation
R and E Command
ATTN: Chief, Tech Svcs Div
Fort Eustis, Virginia 1

Armed Services Technical
Information Agency
Arlington Hall Station
Arlington 12, Virginia 10

Director, Geophysical Research
Directorate
USAF Cambridge Research Center
Hanscom Field
New Bedford, Massachusetts 1

Director, Geophysical Research
Directorate
USAF Cambridge Research Center
ATTN: CRZD
Hanscom Field
New Bedford, Massachusetts 2

Commander
USAF Air Weather Service
Scott Air Force Base, Illinois 1

Commander
2d Weather Group
USAF Air Weather Service
Langley Field, Virginia 1

Chief of Naval Operations (OP 07)
U. S. Navy Department
Washington 25, D. C. 1

Chief, Bureau of Naval Weapons (FAME)
U. S. Navy Department
Washington 25, D. C. 1

Office of Naval Research
U. S. Navy Department
Washington, D. C. 1

Chief, Naval Weather Svce.
U. S. Naval Station
Washington 25, D. C. 1

Commander
U. S. Naval Research Lab. (Code 7100)
Washington 25, D. C. 1

Officer-in-Charge
U. S. Naval Weather Research Facility
U. S. Naval Air Station
Norfolk, Virginia 1

Commander
U. S. Navy Electronics Lab.
ATTN: Dr. M. Halstead
San Diego 52, California 1

Officer-in-Charge
Meteorological Curriculum
U. S. Naval Post Graduate School
Monterey, California 1

Commandant
U. S. Marine Corps School
U. S. Marine Corps Development Center
Quantico, Virginia 2

Internal USAEPG 62

Other Government Agencies

Director, Atmospheric Sciences Program
National Science Foundation
Washington 25, D. C. 1

Chief
U. S. Weather Bureau
Washington 25, D. C. 7

Chief
National Aeronautics and Space Administration
Washington 25, D. C. 1

Director, Federal Aviation Agency
Bureau of Research and Development
ATTN: Records Officer
Washington 25, D. C. 1

Director, National Research Council, National Academy of Sciences
2101 Constitution Avenue
Washington 25, D. C. 1

Chief, Radio Propagation Lab.
U. S. National Bureau of Standards
Boulder, Colorado 1

Chief, Fallout Studies Branch
Div. of Biology and Medicine
Atomic Energy Commission
Washington 25, D. C. 1

Chief, Agricultural Research Svce.
Soil and Water Conservation Div.
U. S. Dept. of Agriculture
Beltsville, Maryland 1

Director, Pacific Southwest Forest and Range Expt. Station
U. S. Dept. of Agriculture
Forest Service
P. O. Box 245
Berkeley 1, California 1

Nongovernment Agencies

Executive Secretary
American Meteorological Society
45 Beacon Street
Boston 8, Massachusetts 1

University Corporation for Atmospheric Research (UCAR)

Director, National Center for Atmospheric Research
University of Colorado
Boulder, Colorado 1

Director, Meteorology Dept.
University of Arizona
Tucson, Arizona 1

Director, Meteorology Dept.
University of California
Los Angeles 24, California 1

Director, Meteorology Dept.
The University of Chicago
Chicago 37, Illinois 1

Director, Meteorology Dept.
Cornell University
Ithaca, New York 1

Director, Meteorology Dept.
Florida State University
Tallahassee, Florida 1

Director, Meteorology Dept.
Johns Hopkins University
Baltimore, Maryland 1

Director, Meteorology Dept.
Massachusetts Institute of Technology
Cambridge 37, Mass. 1

Director, Meteorology Dept.
University of Michigan
Ann Arbor, Michigan 1

Director, Meteorology Dept.
New York University
University Heights
New York 53, New York 1

Director, Meteorology Dept.
Pennsylvania State University
University Station, Pa. 1

Director, Meteorology Dept.
St. Louis University
St. Louis, Missouri 1

Dept. of Oceanography and Meteorology
Agricultural and Mechanical College of Texas
College Station, Texas 1

Director, Meteorology Dept.
University of Washington
Seattle, Washington 1

USAEPG Micrometeorology Research Contractors

Chief, Agricultural Research Svce.
Soil and Water Conservation Research Division
U. S. Department of Agriculture
U. S. Salinity Laboratory
P. O. Box 672
Riverside, California 1

Chief, Agricultural Research Svce.
Southern Piedmont Soil Conservation Field Station
U. S. Dept. of Agriculture
P. O. Box 33
Watkinsville, Georgia 1

Chief, Agricultural Research Svce.
U. S. Water Conservation Lab.
U. S. Dept. of Agriculture
Route 2, P. O. Box 816-A
Tempe, Arizona 1

Chief, Agricultural Research Svce.
Soil and Water Conservation
Research Division
U. S. Dept. of Agriculture
Cornell University, Bailey Hall
Ithaca, New York 1

Department of Meteorology
University of Wisconsin
Madison, Wisconsin 1

Department of Meteorology
Massachusetts Institute
of Technology
Round Hill Field Station
South Dartmouth, Mass. 1

Smyth Research Associates
3555 Aero Court
San Diego 11, California 1

Dept. of Civil Engineering
Colorado State University
Fort Collins, Colorado 1

Dept. of Agricultural Chemistry
and Soils
University of Arizona
College of Agriculture
Tucson, Arizona
ATTN: Mr. Anderson 1

Department of Agronomy
Utah State University
Logan, Utah 1

Department of Irrigation
University of California
College of Agriculture
Agricultural Experiment Station
Davis, California 1

Armour Research Foundation
of Illinois
Institute of Technology
Technology Center
10 West 35th Street
Chicago 16, Illinois

Other Universities Conducting Meteorology Research

University of Minnesota
ATTN: Dean Spilhouse
Minneapolis, Minnesota 1

Department of Geophysics
Washington University
St. Louis, Missouri 1

Meteorology Department
University of Hawaii
Honolulu, Hawaii 1

Atmospheric Science Branch
Scientific Research Institute
Oregon State College
Corvallis, Oregon 1

Department of Meteorology
University of Utah
Salt Lake City, Utah 1

Department of Physics
Iowa State College
Ames, Iowa 1

Electrical Engineering Research
Laboratory
The University of Texas
Austin, Texas 1

Department of Soils
University of Missouri
Columbia, Missouri 1

Laboratory of Climatology Associates
Route 1, Centerton
Elmer, New Jersey 1

Dept. of Agricultural Engineering
ATTN: Dr. F. A. Brooks
University of California
Davis, California 1

AD________________ Accession Nr________________

UNCLASSIFIED

Department of Meteorology, University of Wisconsin, Madison, Wisconsin
ANNUAL REPORT, 1961. STUDIES OF THE THREE-DIMENSIONAL STRUCTURE OF THE PLANETARY BOUNDARY LAYER by Dr. H. H. Lettau and others.
First Annual Report (1 July 1959 through 30 June 1961)
Pub August 1961, USAEPG Technical Program DS Project 3A99-27-005
170 pp 37 illustrations. Unclassified Report.

This report is concerned with investigations of the three-dimensional structure of the planetary boundary layer. Investigations of four types are reported: (1) A comparison of experimental determinations with a theoretical model for the effects of solar heating at the earth's surface, (2) experimental determinations of the effect of surface roughness on the dynamics of the air near the earth's surface, (3) a new theoretical model for the length-scale of turbulence for duct flow and atmospheric boundary layer flow, and (4) a theoretical analysis of the steady-state, neutral wind profile for the entire planetary boundary layer.

Micrometeorology — Energy Balance

Micrometeorology — Surface Roughness

Turbulent Boundary Layer — Mathematical

CONTRACT DA-36-039-SC-80282

UNCLASSIFIED

AD________________ Accession Nr________________

UNCLASSIFIED

Department of Meteorology, University of Wisconsin, Madison, Wisconsin
ANNUAL REPORT, 1961. STUDIES OF THE THREE-DIMENSIONAL STRUCTURE OF THE PLANETARY BOUNDARY LAYER by Dr. H. H. Lettau and others.
First Annual Report (1 July 1959 through 30 June 1961)
Pub August 1961, USAEPG Technical Program DS Project 3A99-27-005
170 pp 37 illustrations. Unclassified Report.

This report is concerned with investigations of the three-dimensional structure of the planetary boundary layer. Investigations of four types are reported: (1) A comparison of experimental determinations with a theoretical model for the effects of solar heating at the earth's surface, (2) experimental determinations of the effect of surface roughness on the dynamics of the air near the earth's surface, (3) a new theoretical model for the length-scale of turbulence for duct flow and atmospheric boundary layer flow, and (4) a theoretical analysis of the steady-state, neutral wind profile for the entire planetary boundary layer.

Micrometeorology — Energy Balance

Micrometeorology — Surface Roughness

Turbulent Boundary Layer — Mathematical

CONTRACT DA-36-039-SC-80282

UNCLASSIFIED

AD________________ Accession Nr________________

UNCLASSIFIED

Department of Meteorology, University of Wisconsin, Madison, Wisconsin
ANNUAL REPORT, 1961. STUDIES OF THE THREE-DIMENSIONAL STRUCTURE OF THE PLANETARY BOUNDARY LAYER by Dr. H. H. Lettau and others.
First Annual Report (1 July 1959 through 30 June 1961)
Pub August 1961, USAEPG Technical Program DS Project 3A99-27-005
170 pp 37 illustrations. Unclassified Report.

This report is concerned with investigations of the three-dimensional structure of the planetary boundary layer. Investigations of four types are reported: (1) A comparison of experimental determinations with a theoretical model for the effects of solar heating at the earth's surface, (2) experimental determinations of the effect of surface roughness on the dynamics of the air near the earth's surface, (3) a new theoretical model for the length-scale of turbulence for duct flow and atmospheric boundary layer flow, and (4) a theoretical analysis of the steady-state, neutral wind profile for the entire planetary boundary layer.

Micrometeorology — Energy Balance

Micrometeorology — Surface Roughness

Turbulent Boundary Layer — Mathematical

CONTRACT DA-36-039-SC-80282

UNCLASSIFIED

AD________________ Accession Nr________________

UNCLASSIFIED

Department of Meteorology, University of Wisconsin, Madison, Wisconsin
ANNUAL REPORT, 1961. STUDIES OF THE THREE-DIMENSIONAL STRUCTURE OF THE PLANETARY BOUNDARY LAYER by Dr. H. H. Lettau and others.
First Annual Report (1 July 1959 through 30 June 1961)
Pub August 1961, USAEPG Technical Program DS Project 3A99-27-005
170 pp 37 illustrations. Unclassified Report.

This report is concerned with investigations of the three-dimensional structure of the planetary boundary layer. Investigations of four types are reported: (1) A comparison of experimental determinations with a theoretical model for the effects of solar heating at the earth's surface, (2) experimental determinations of the effect of surface roughness on the dynamics of the air near the earth's surface, (3) a new theoretical model for the length-scale of turbulence for duct flow and atmospheric boundary layer flow, and (4) a theoretical analysis of the steady-state, neutral wind profile for the entire planetary boundary layer.

Micrometeorology — Energy Balance

Micrometeorology — Surface Roughness

Turbulent Boundary Layer — Mathematical

CONTRACT DA-36-039-SC-80282

UNCLASSIFIED